This pdf file consists of all figures, and their captions, scanned from:

# MICROSTRUCTURAL EVOLUTION

# IN CRYSTAL-MELT SYSTEMS

by

Youngdo Park

Photographic figures in the printed copy have a coarse dot screen; these images in this file have been smoothed using the scanner image software

A Dissertation

Submitted to the University at Albany, State University of New York

in Partial Fulfillment of

the Requirements for the Degree of

Doctor of Philosophy

College of Arts and Sciences
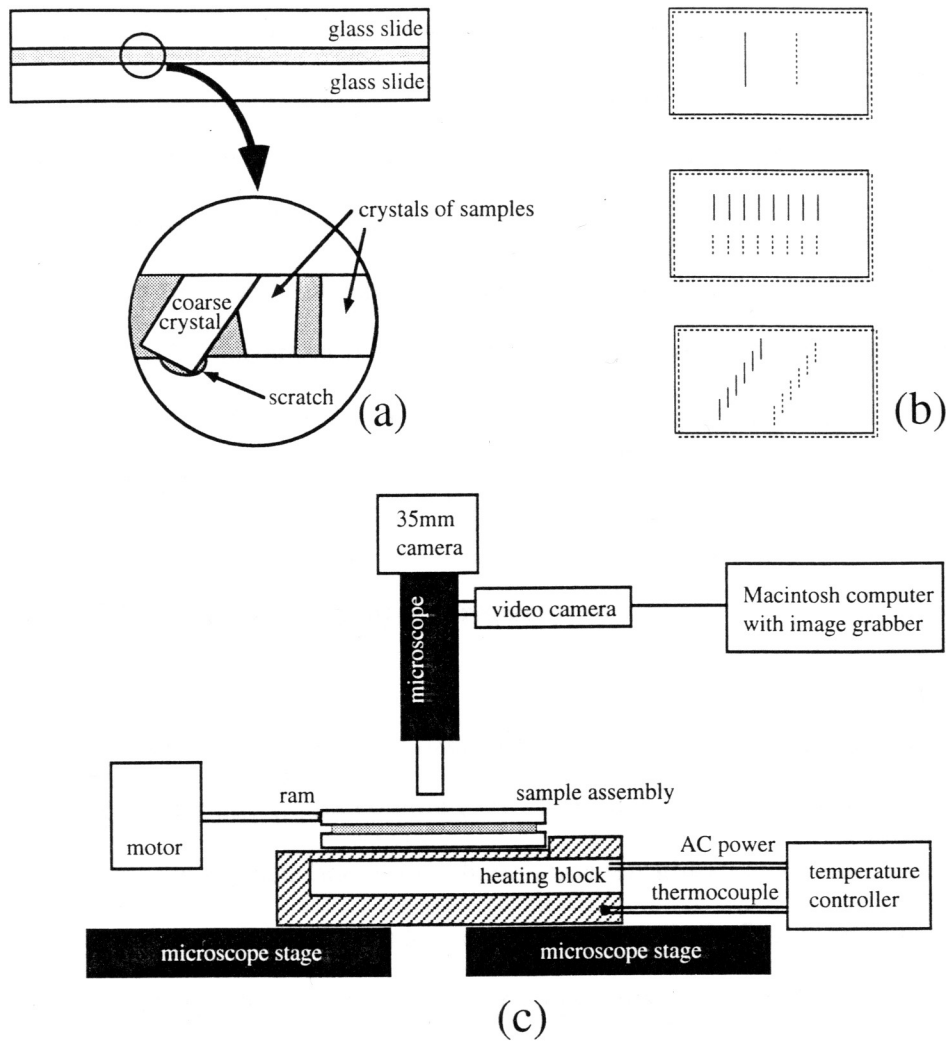
Department of Geological Sciences

1994

Figure 2.1   Sample assembly and experimental apparatus used for deformation experiments.  (a) Sample assembly made of two slide glasses and thin film of crystal-melt mixture (shaded, thickness exaggerated).  Scratches on glass accommodate large crystals which serve as grips.  (b) Geometry of grips for pure shearing, simple shearing and general shearing (top to bottom).  Solid and dashed lines represent top and bottom slides respectively.  (c) Experimental apparatus, including stage-mounted press, heating block with thermocontroller, 35mm camera and video camera connected to a Macintosh computer with image grabber.
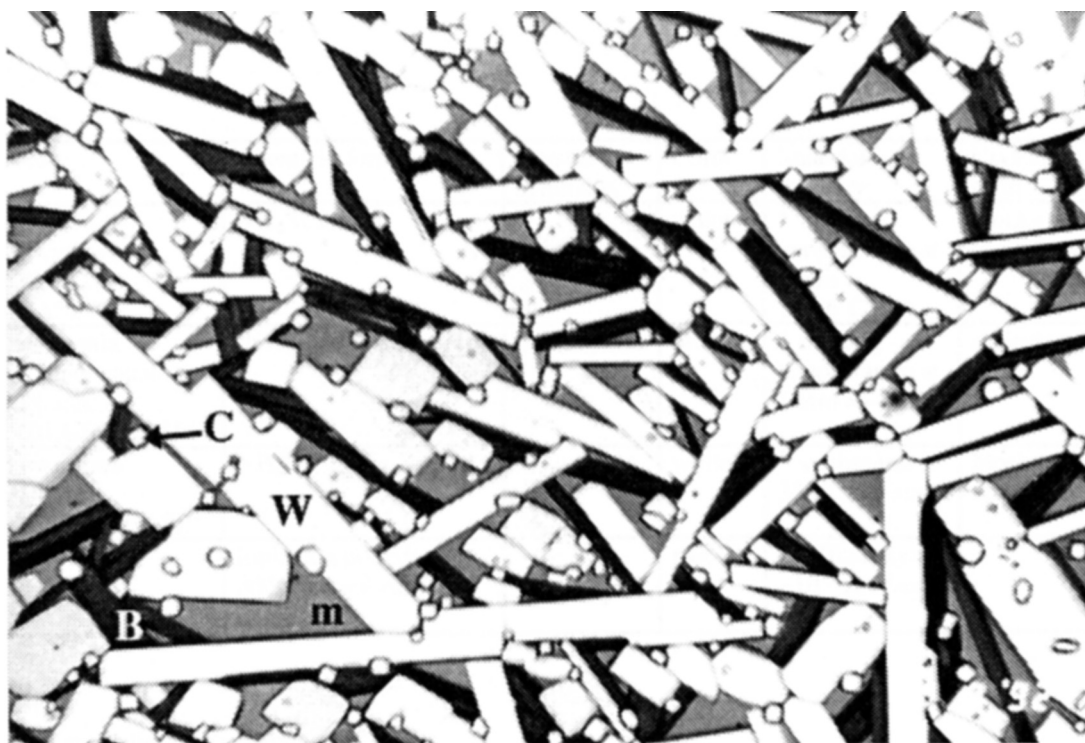
Figure 2.2    Plane polarized light photomicrograph of the sample material.  The sample is made of three crystalline phases and liquid.  Three crystalline phases are W (white phase, ammonium thiocyanate), B (blue phase, diammonia tetrathiocyanato cobaltate), and C (cube phase, ammonium chloride).  The liquid phase or melt (m) is gray background between crystals.  Field width: 1.5 mm.
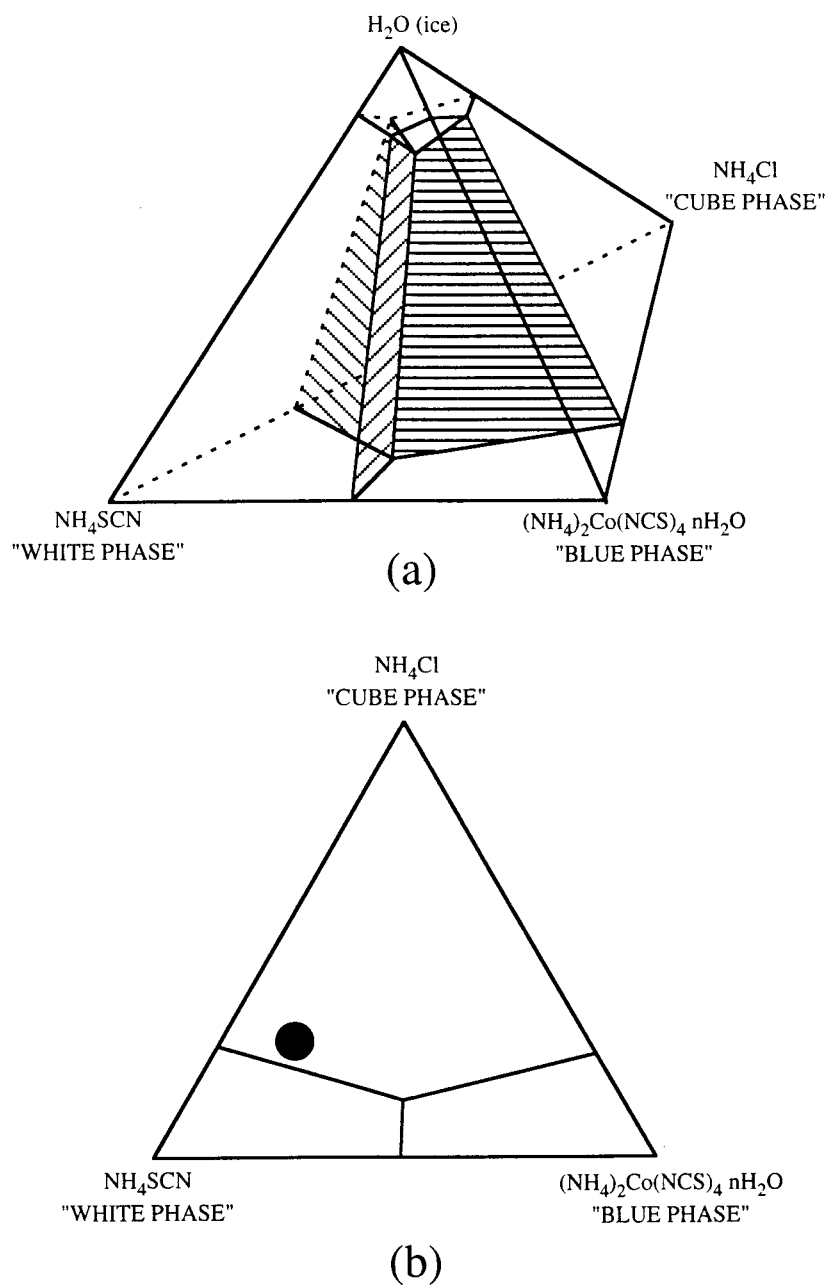
Figure 2.3  Schematic and provisional phase diagram of the experimental system. (a) Quaternary eutectic phase diagram, consistent with crystallization and melting experimental observations. The positions of the cotectic lines and the solid solution relation are not precisely known. (b) Projected quaternary phase diagram onto the base of the tetrahedron in (a). Bulk composition (filled circle) of the material used for experiments is in the liquidus field of the cube phase.

Figure 2.4   Crystal plastic deformation and growth of a recrystallized crystal in plane polarized light (left) and crossed polarized light (right).   W: white phase crystal, m: melt.   (a) & (e) t=0 minutes.   (b) & (f) t=5 minutes.   (c) & (g) t=10 minutes.   (d) & (h) t=15 minutes.   Arrows mark cusps in crystal/melt interface which are characteristic of white phase crystal deforming crystal plastically in melt.   Slip traces in the white phase crystal can be seen in the contrast-modified box in (a).   Field width: 0.5 mm.
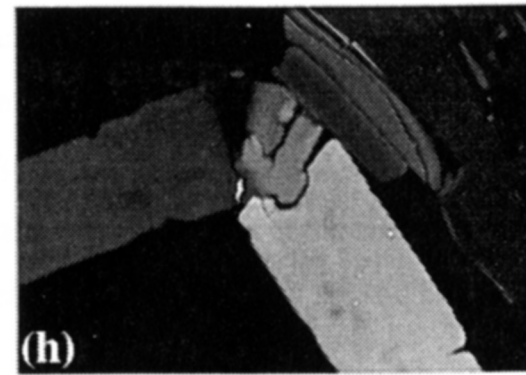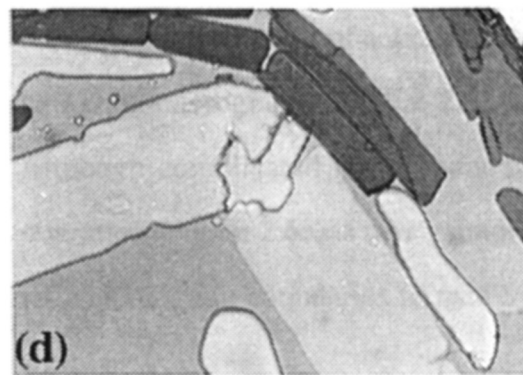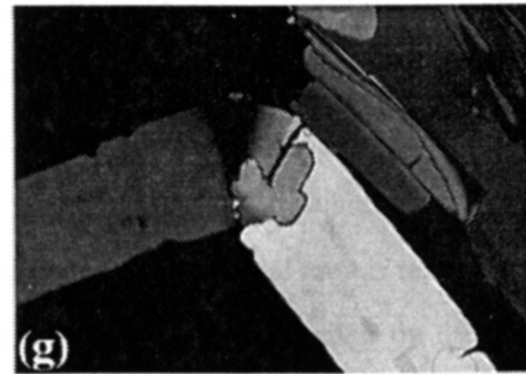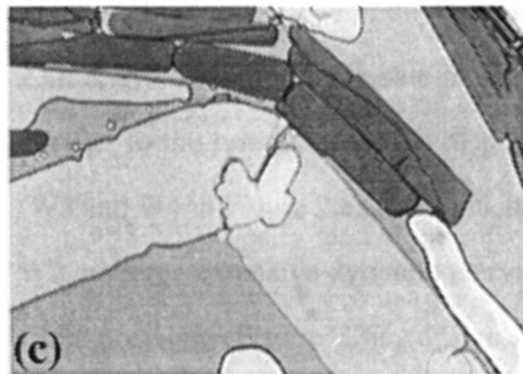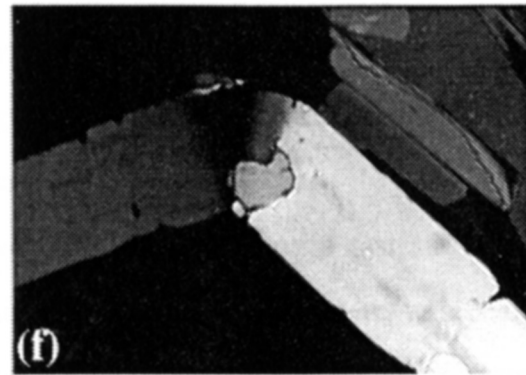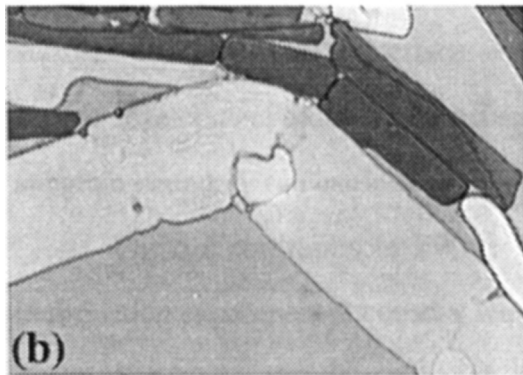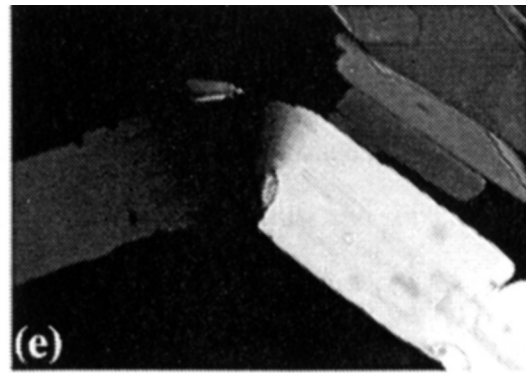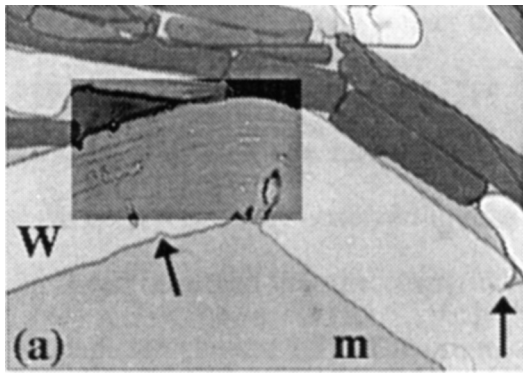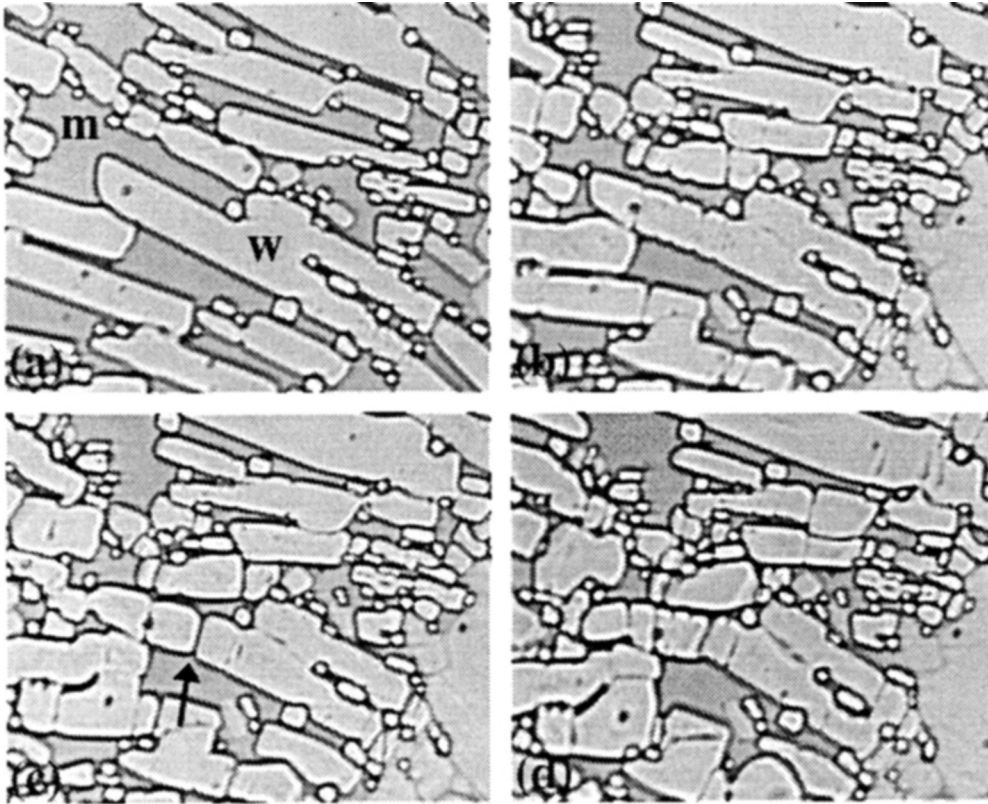
Figure 2.5   Segmentation of a white phase crystal (W) by propagation of the cuspy crystal-melt interfaces. m: melt.  The positions of subgrain boundaries in the white phase crystal (b), correspond to the positions of the cuspy crystal-melt interfaces.  After complete propagation of cuspy crystal-melt interface across the white phase crystal W (c), the originally single white phase crystal W becomes segmented or divided into separate crystals (d).  (a) t=0 minutes.  (b) t=43 minutes.  (c) t=53 minutes.  (d) t=73 minutes.  Field width: 0.23 mm.

Figure 2.6 Dynamic recrystallization during melt-present deformation. W1,W2,W3,W4: white phase crystals, m: melt. The lines in (a) & (e) indicate dextral shearing in this field of view although pure shearing grips were used. (a) & (g) t=0 minutes. (b) & (h) t=3 minutes. (c) & (i) t=8 minutes. (d) & (j) t=14 minutes. (e) & (k) t= 14 minutes. (f) & (l) t=5 days (static recovery at constant temperature). (a)-(f): plane polarized light, (g)-(l): crossed polarized light. Field width: 0.47 mm.
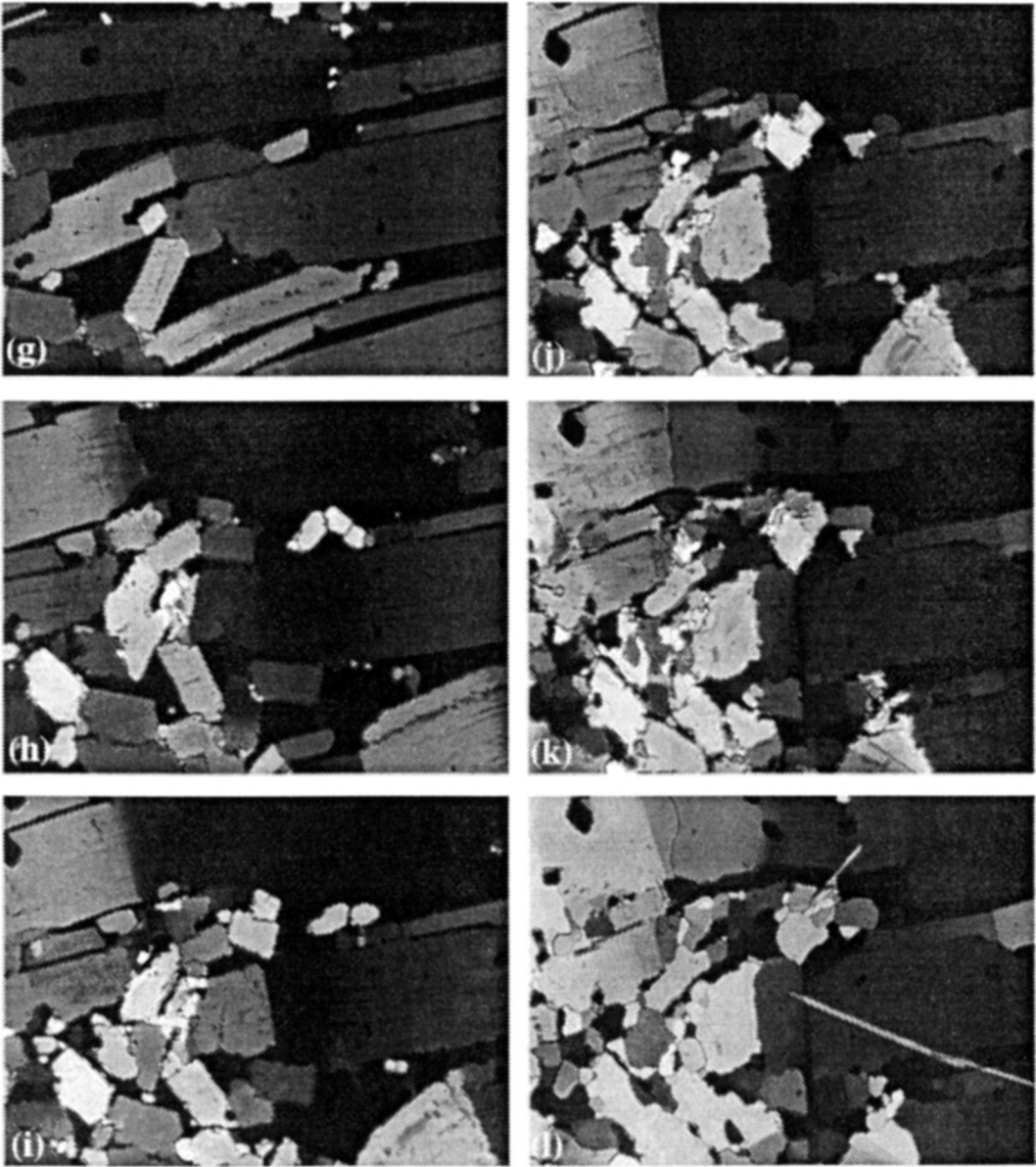
2-21
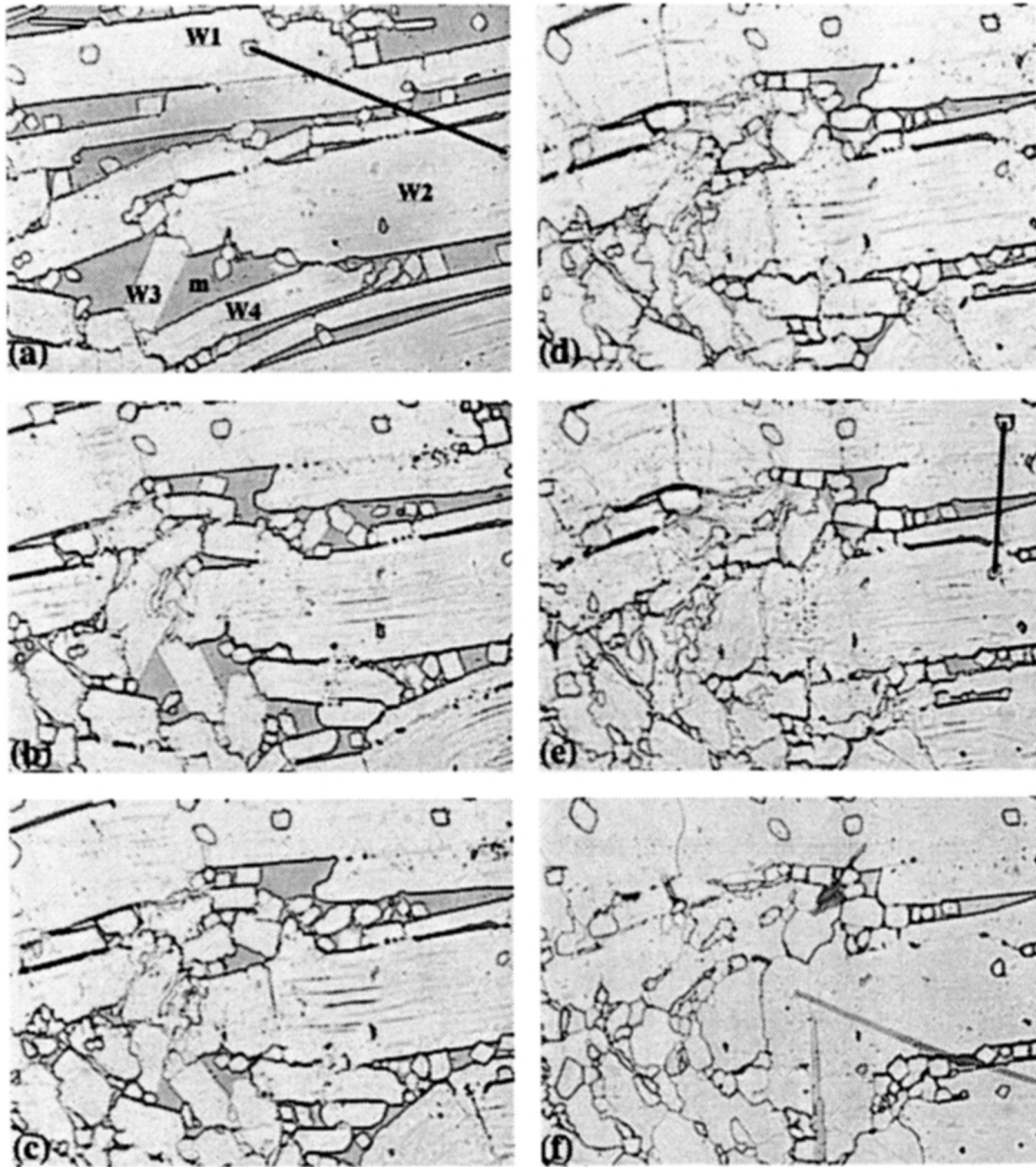
Figure 2.7   Contact melting/redeposition during slow strain rate experiment. W1,W2,W3,W4,W5,W6,W7: white phase crystals, m: melt.  The white phase crystal W1 changes its length by melting at the contacts with crystals W2 and/or W3. Development of indented grain boundary by preferential contact melting can be seen in crystal W6.  Notice no length change in indenting crystal W7 between a & e.  Crystal W4 dissects crystal W1 by grain boundary migration (d & e).  (a) t= 0 minutes.  (b) t= 60 minutes.  (c) t= 171 minutes.  (d) t= 179 minutes.  (e) & (f) t= 180 minutes.  (a)-(e): plane polarized light, (f) crossed polarized light.  Constructed horizontal line in (a) and (e) indicates local shortening.  Field width: 0.48 mm.
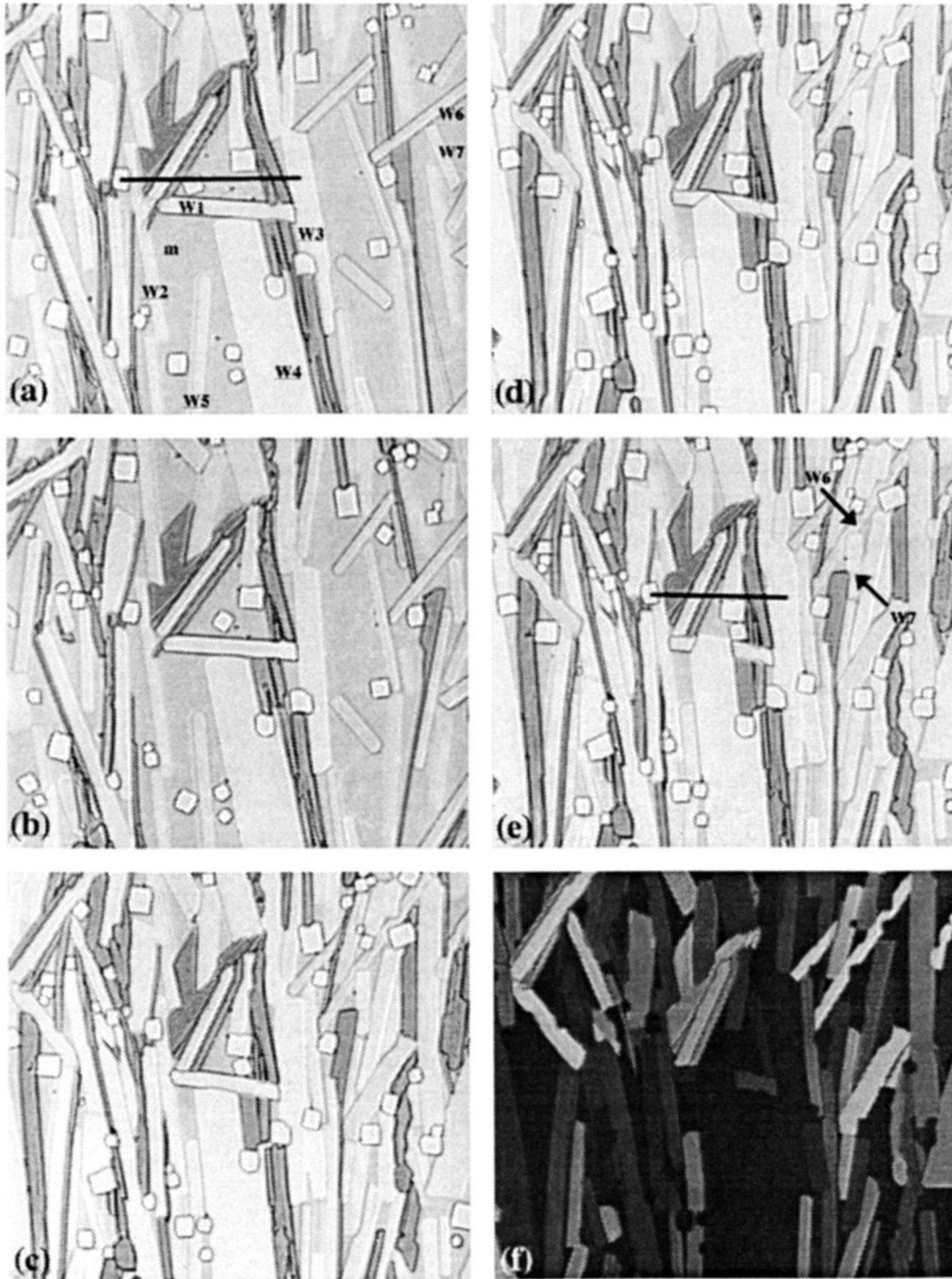
Figure 2.8    Contact melting/redeposition during slow strain rate experiment. W1,W2,W3: white phase crystals, B1: blue phase crystal, m:melt. Contact melting of the white phase crystal W1 is observed at the contact between W1 and B1 boundaries. Redeposition of the white phase crystal component after contact melting can be observed on crystal W3. (a) t=0 minutes. (b) t= 40 minutes. (c) t= 50 minutes. (d) t=60 minutes. (e) t=70 minutes. (f) t=100 minutes. (g) & (h) t=320 minutes. (a)-(g): plane polarized light, (h): crossed polarized light. Field width: 0.29 mm.
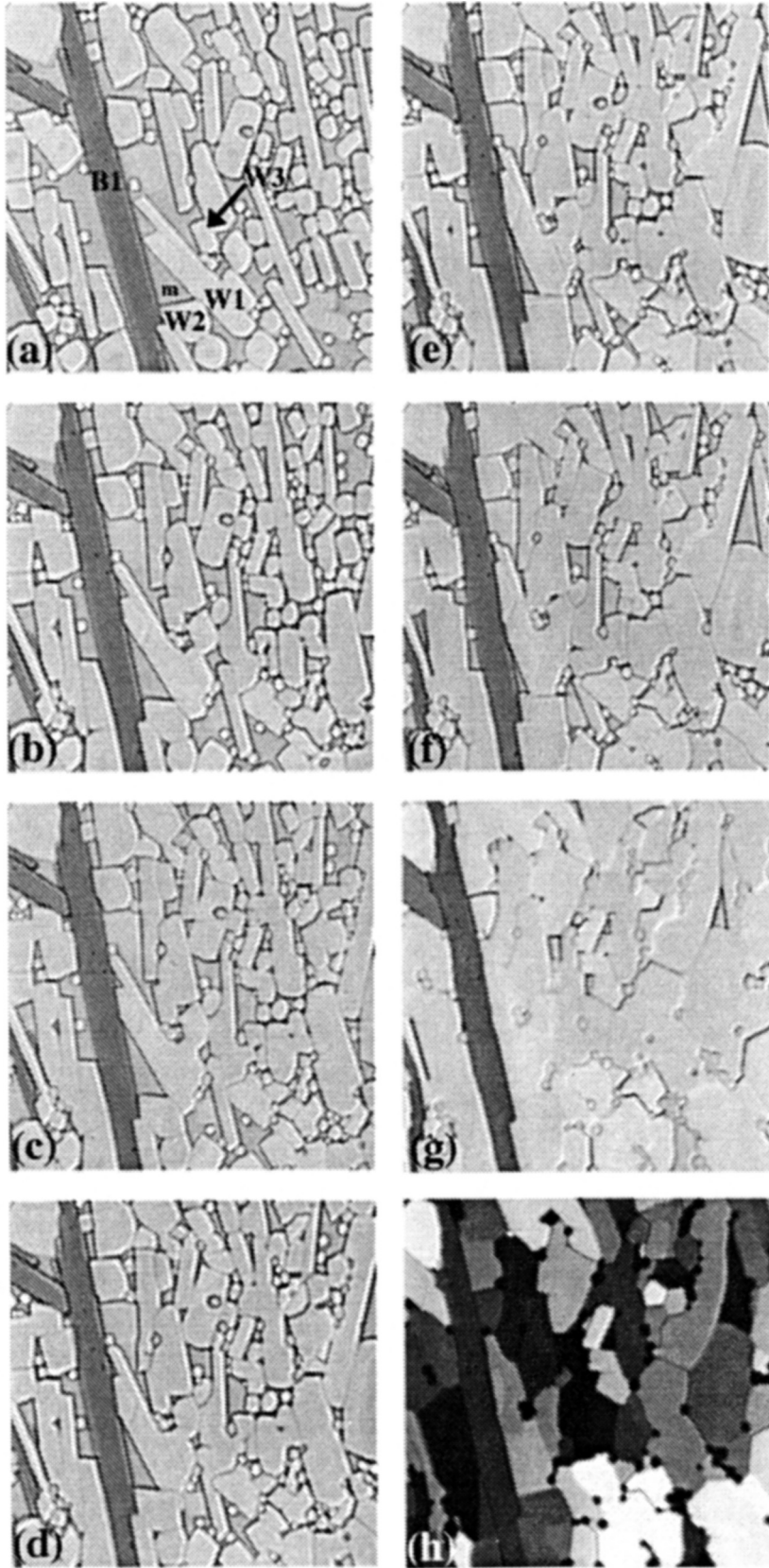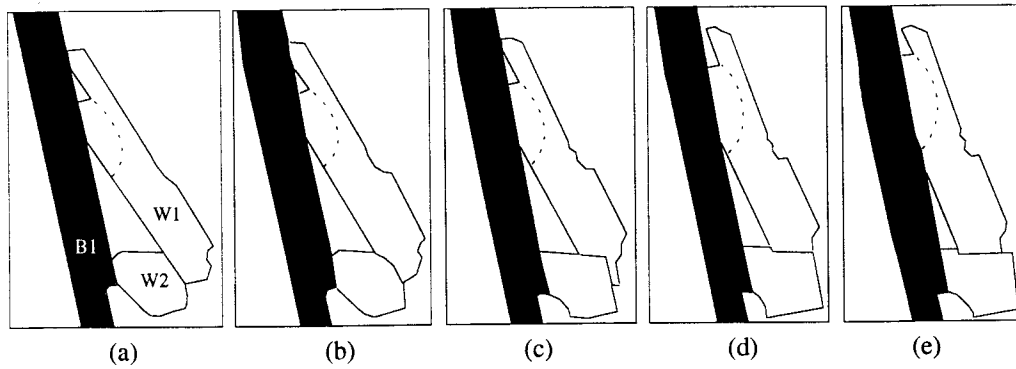
Figure 2.9  Grain boundary migration assisted grain boundary sliding during slow strain rate experiment. Sketches of the grain or phase boundaries in (a), (b), (c), (d), & (e) correspond to the photomicrographs of Figure 8(b), 8(c), 8(d), 8(e), & 8(f), respectively.

Figure 2.10 Grain flow by sliding along crystal boundaries and rotation of crystals. W1,W2: white phase crystals. Notice large strain in the field of view (compare positions of crystals with dots in a, b, & c). (d) Grain boundary sliding along the boundary between W1 and W2 crystals occurs while crystals rotate. (a) t=0 minutes. (b) t=210 minutes. (c) t=345 minutes. (d1) t=0. (d2) t=120 minutes. (d3) t=150 minutes. (d4) t=180 minutes. (a)-(d): plane polarized light. Field width for (a), (b), & (c): 0.4 mm.

2-30
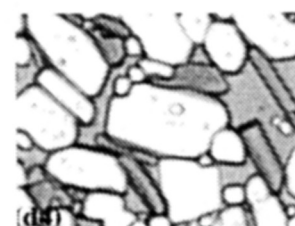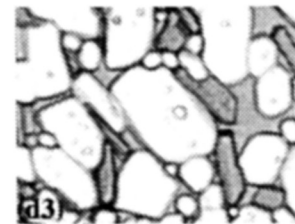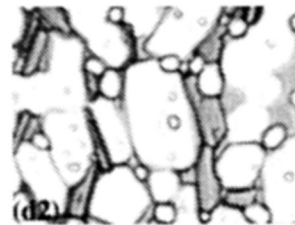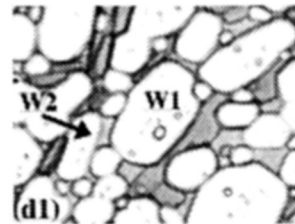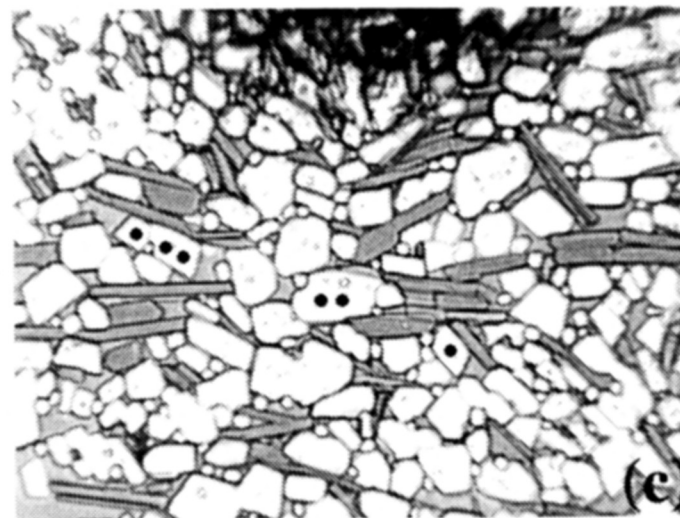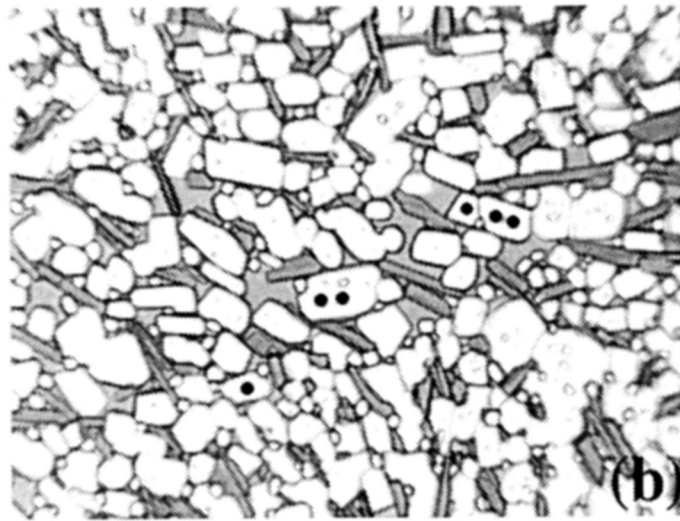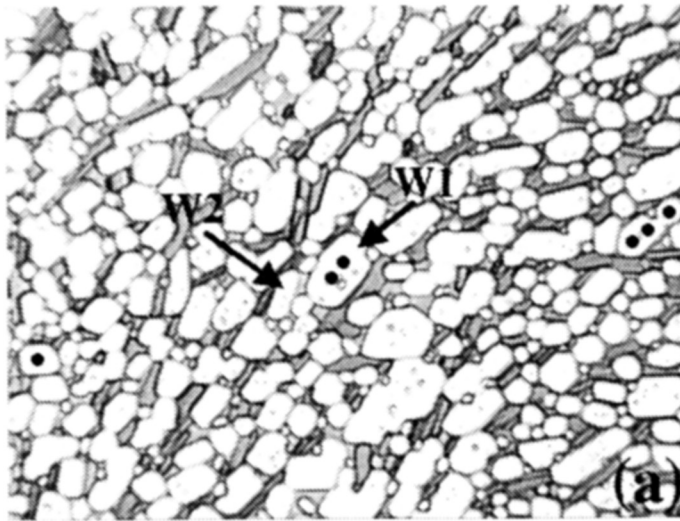
Figure 2.11 Development of a micro shear zone in the sample of low melt fraction. x symbols in (a) represent material points used to construct a displacement map (c). Square symbol in (a) represents the origin for a displacement map (c). Reference frame chosen for displacement maps in (c) is one axis parallel to the horizontal edges of photomicrographs and the other axis perpendicular to the already chosen axis. Displacement maps, 1 to 9 in (c), are the incremental displacement maps from (a) to (b). Displacement map, 10 in (c), is the total displacement map from (a) to (b). The area of different shade in (b) is the micro shear zone, corresponding to the high strain rate zone indicated by displacement maps in (c). (a) t=0. (b) t=120 minutes. (a) & (b): plane polarized light. Field width for (a): 0.18 mm.
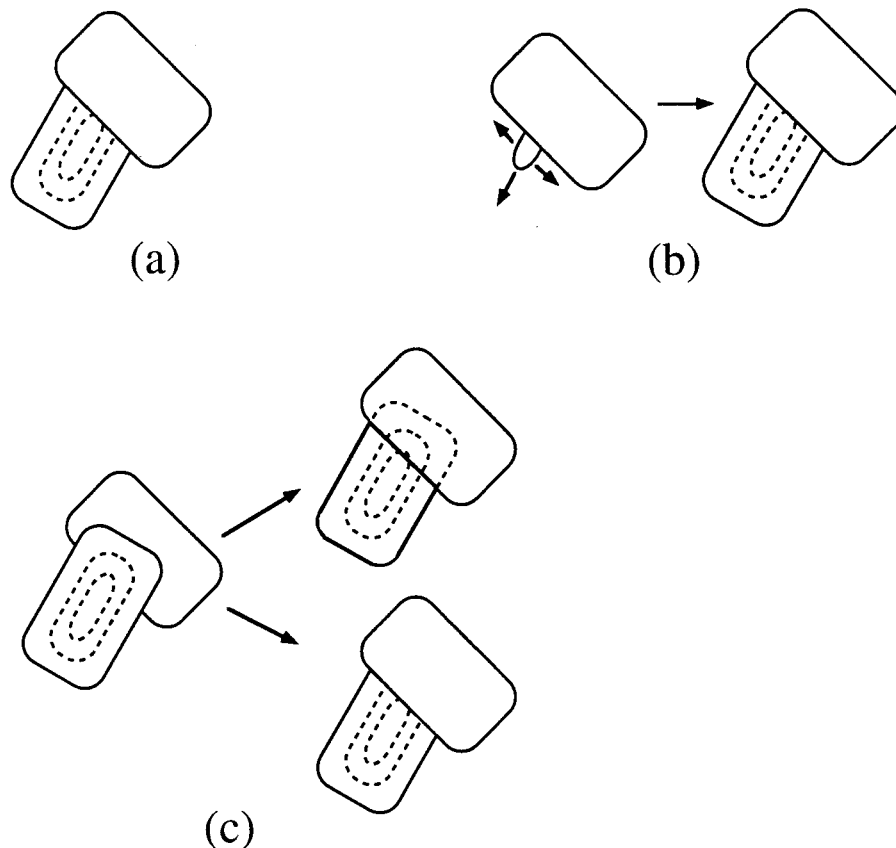
(a)


(b)

(1)    (2)    (3)    (4)

(5)    (6)    (7)    (8)

(9)    (1)~(9)
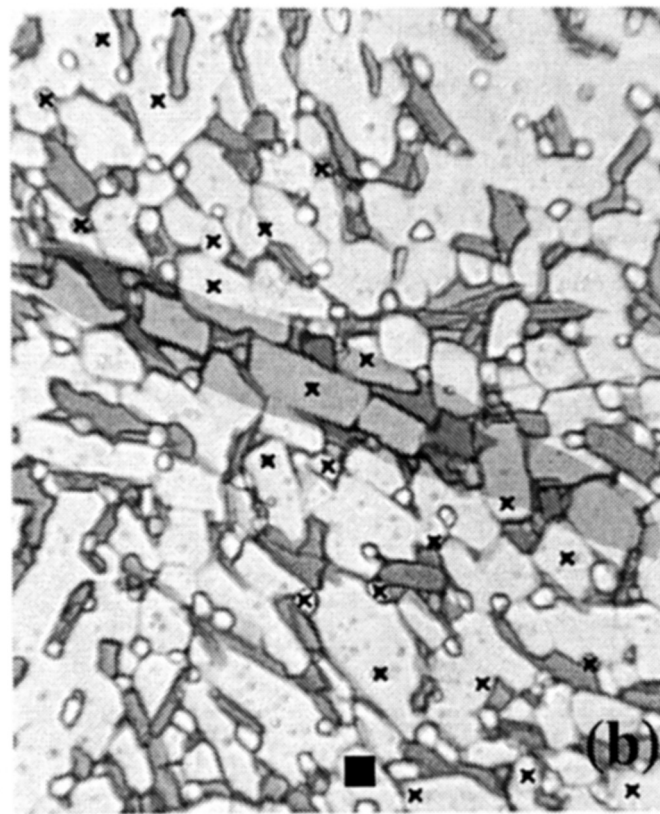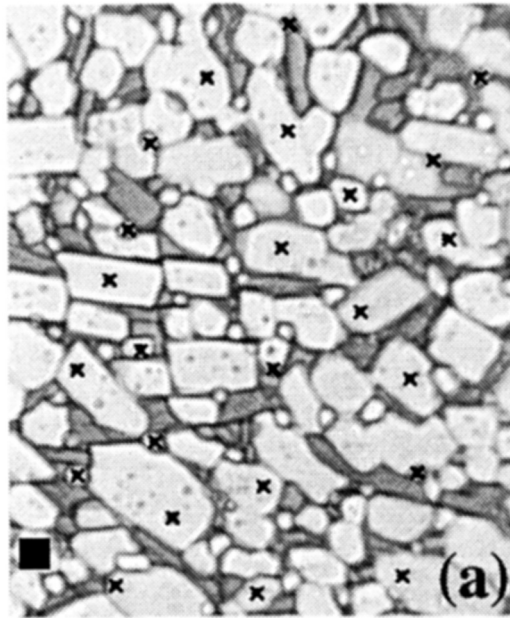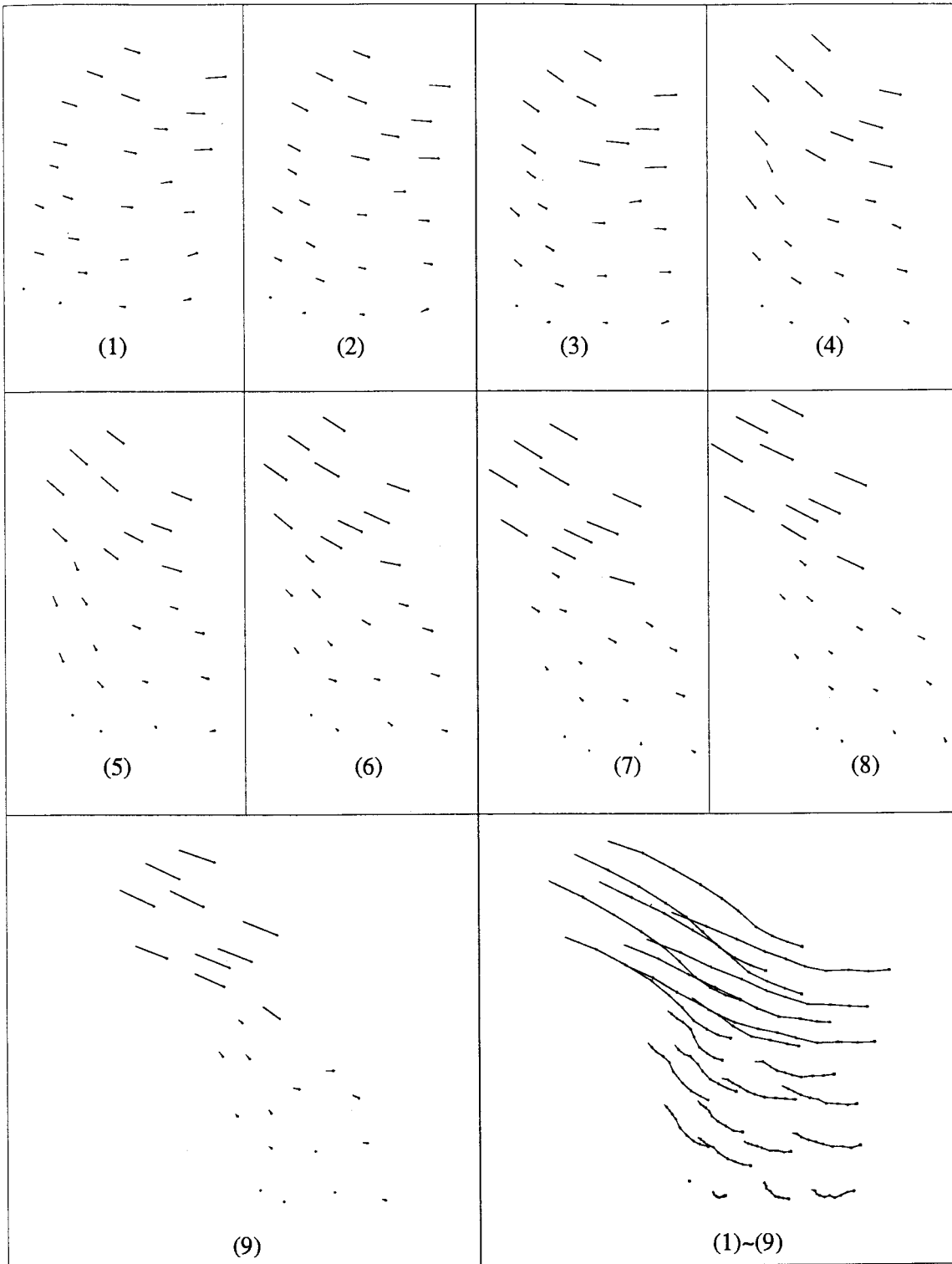
(c)

Figure 2.12 Recognition of microstructures formed by contact melting. Truncated mineral zonation by grain or phase boundary (a) may indicate contact melting. However, since such microstructure can be also formed by other processes - growth impingement (b) and grain or phase boundary migration (c), caution is necessary. (b) Formation of truncated zoning by a boundary during growth impingement. When one crystal is growing while the other stopped growing, such a boundary can be formed although a perfectly planar boundary formed in this way seems unlikely when both crystals are of the same phase. (c) Formation of truncated zoning by grain or phase boundary migration. top: when mineral zonation of the 'consumed' crystal is preserved in the 'consuming crystal', recognition of the process - boundary migration - is obvious. However, when mineral zonation of the consumed crystal was homogenized during boundary migration, recognition of the process becomes difficult, and the resulting microstructure is similar to (a).

Figure 3.1    Photomicrographs taken during the deformation experiment.    Dark region in photomicrographs #21, #24, and #26 is one end of the grip.    Plane polarized light.    Field width: 0.4 mm.
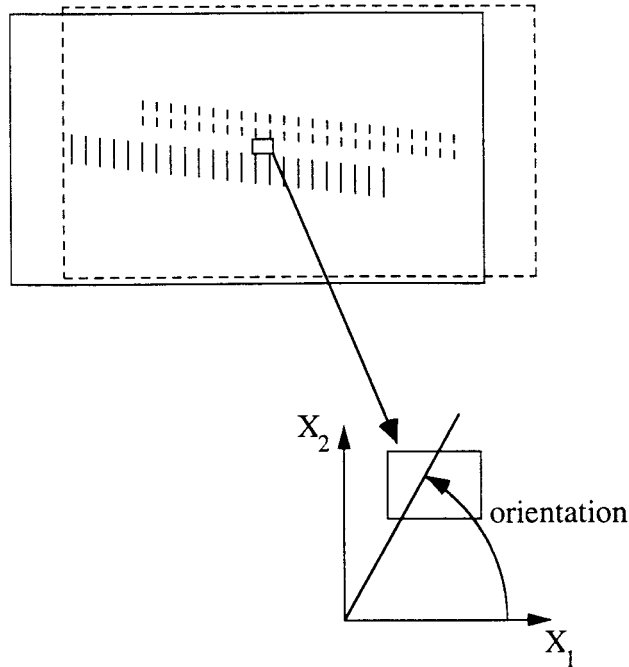
#21 #20 #17 #24
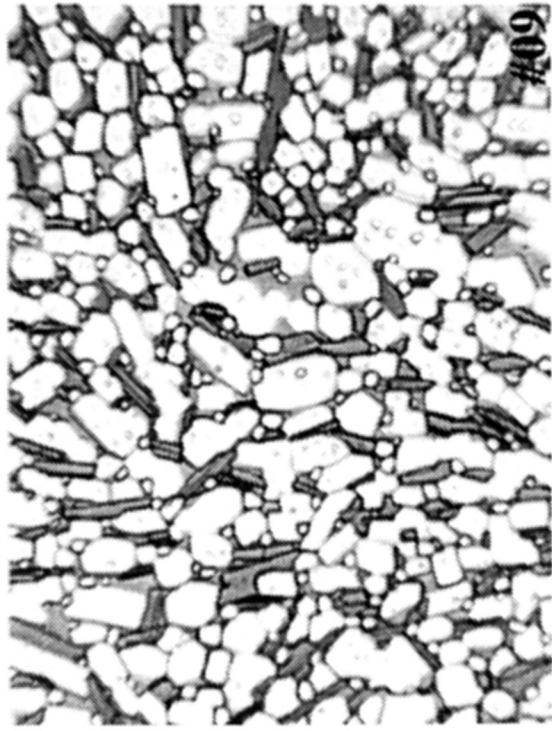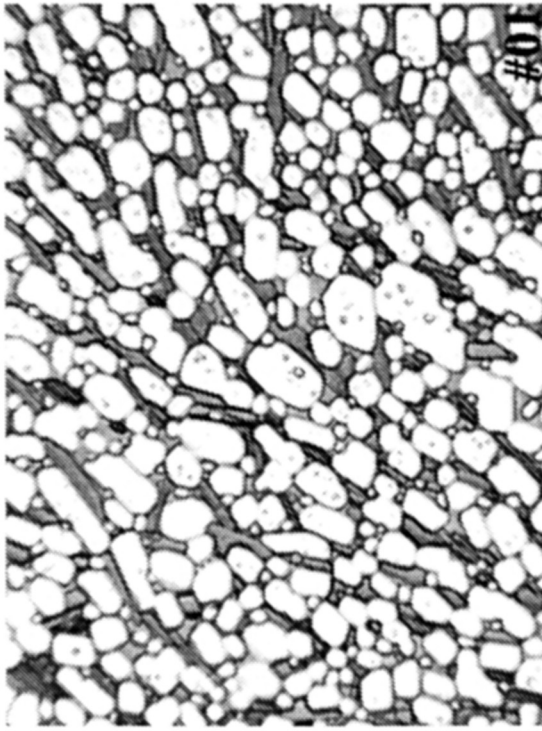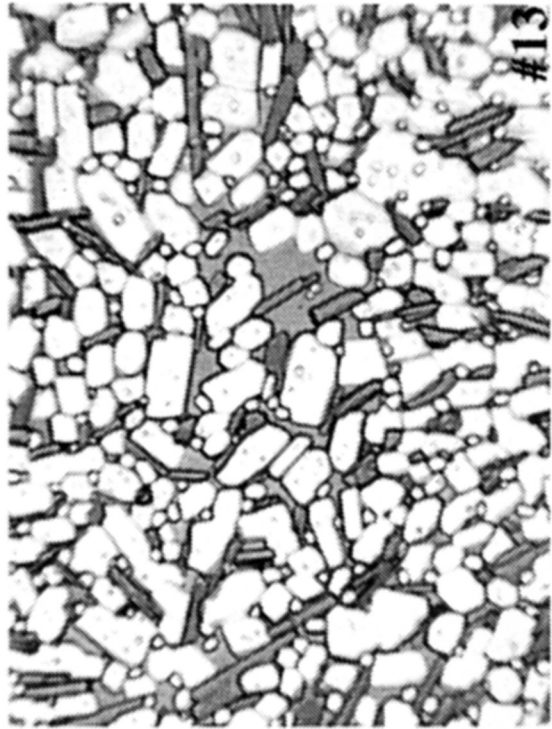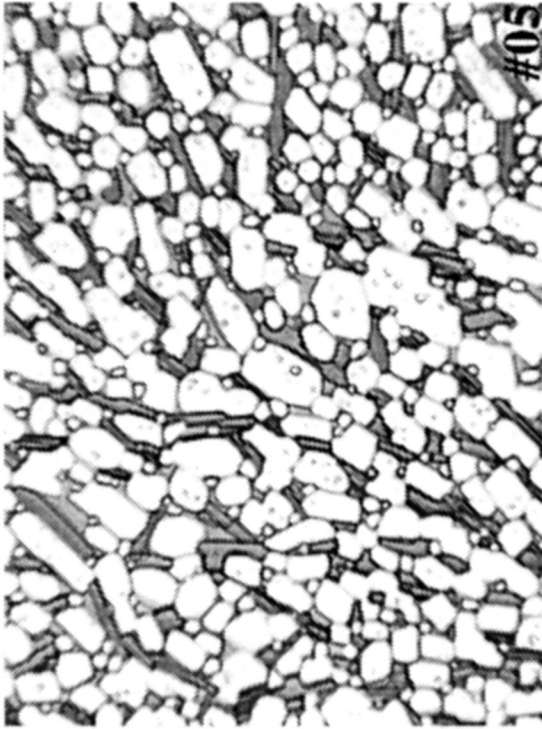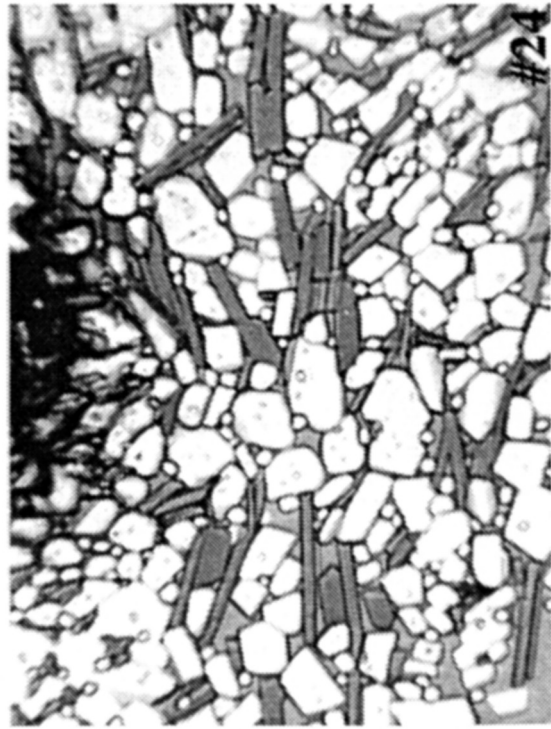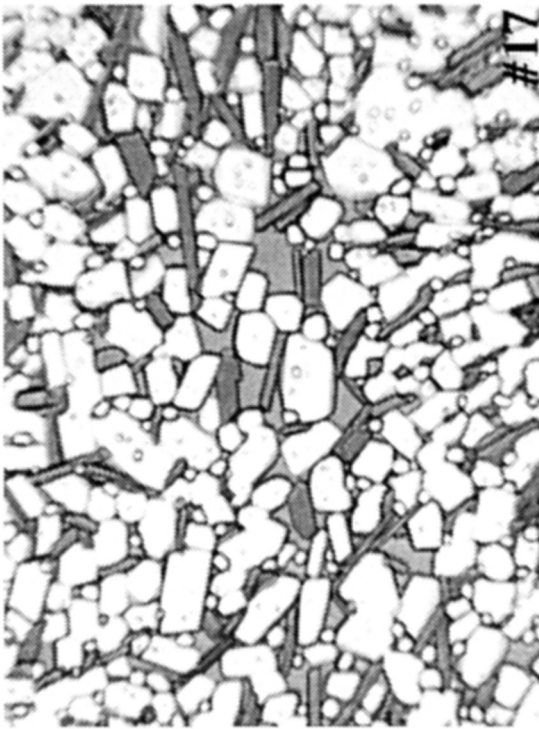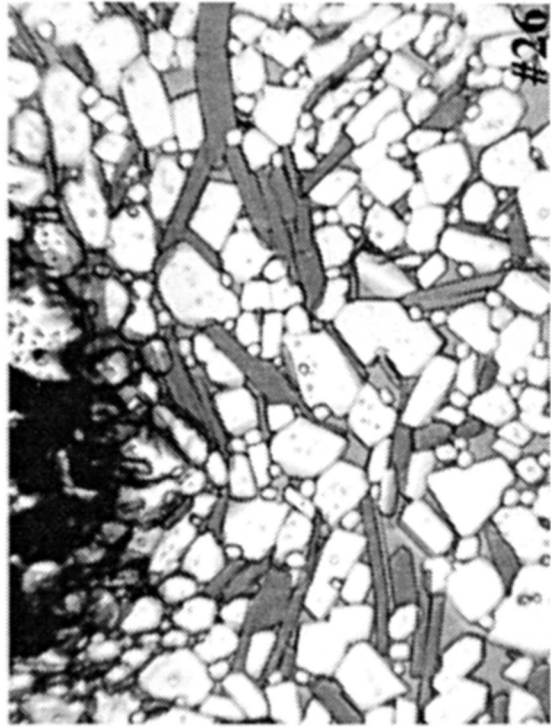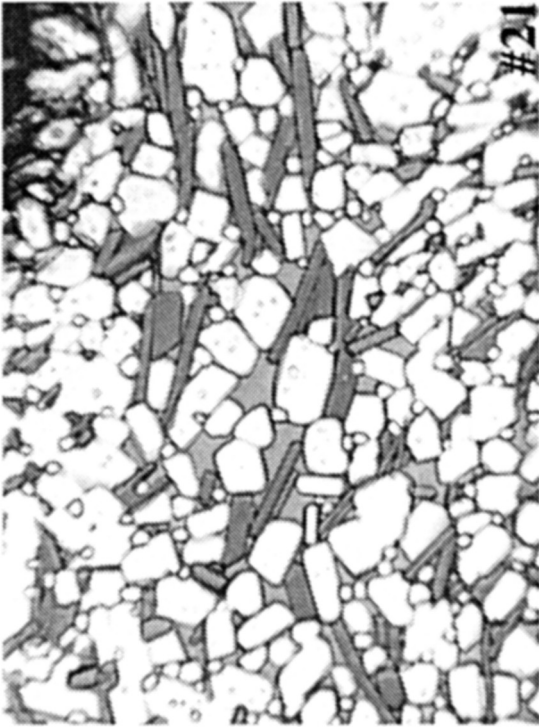
Figure 3.2  Sketch of the sample assembly before experiment TAC-112 and the orthogonal reference frame used in this study. Dashed line represents the lower fixed glass slide and solid line represents the upper moving glass slide. The small box between two grips is the region from which photomicrographs were taken. The upper glass slide moved ~3.5mm during 10 hours. Initial width of shear zone: ~1 mm. Width of shear zone after the experiment: ~0.5 mm. A direction parallel to the horizontal edge of the photomicrographs and to the right is chosen as positive $X_1$ direction. Orientation of crystals was measured counter clockwise from positive $X_1$ direction.
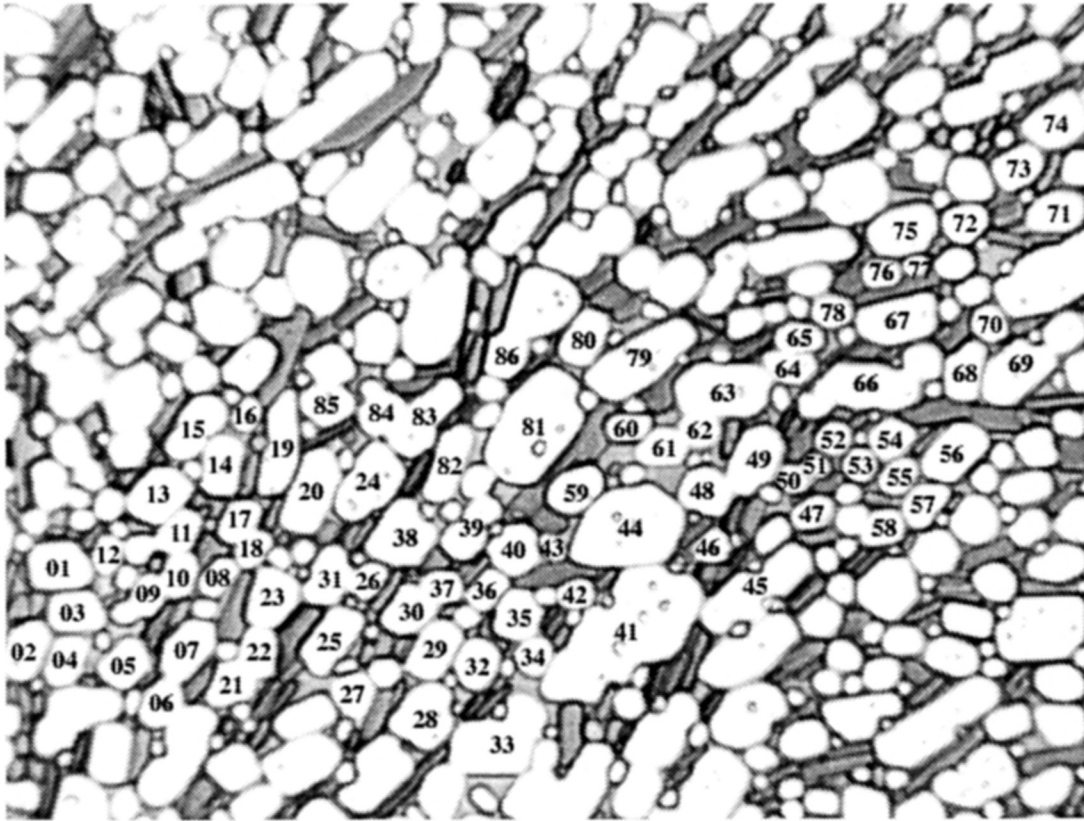
Figure 3.3   Photomicrograph #01 with crystal labels.  The labeled crystals were used to construct displacement maps and to study rotational behavior of the crystals.  Long axes of the labeled crystals were digitized for the first 17 photomicrographs.
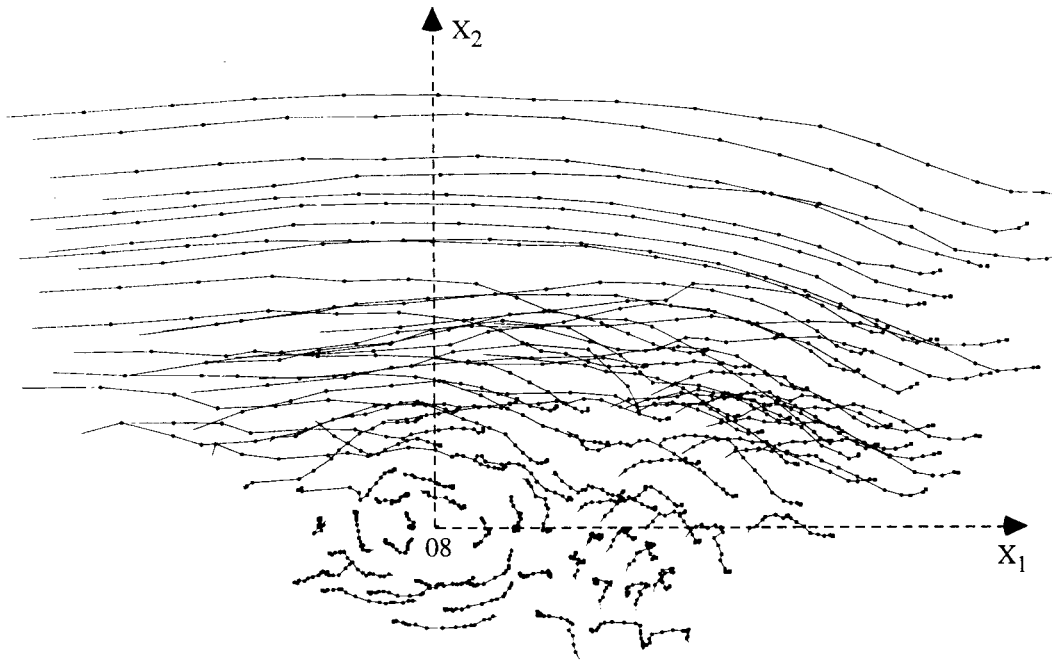
Figure 3.4 Particle trajectories for the first 17 st during the first 17 stages of deformation. Position change of crystals is relative to the white phase crystal 08 in Figure 3.3 and the $X_1$ & $X_2$ axes. Squares indicate the initial positions of each material point.

Figure 3.5   Sketches of the white phase crystals in Figure 3.3 using ellipses.   The black ellipses (back) represent the white phase crystals at one stage (e.g. #01), and the front white ellipses represent the white phase crystals at the next stage (e.g. #02).   The white phase crystals at two different stages during deformation are superimposed with respect to the center of the white phase crystal 08 (Figure 3.3) which is indicated by a cross.   The long axis orientations of the white phase crystals are represented by the rose diagrams.   The radial dimension in the rose diagrams represents the percentage of the total population (radius of the circle: 5% of the total population).

#01-#02

#05-#06

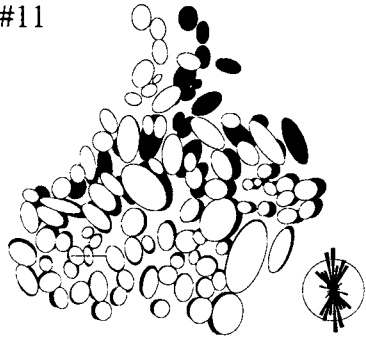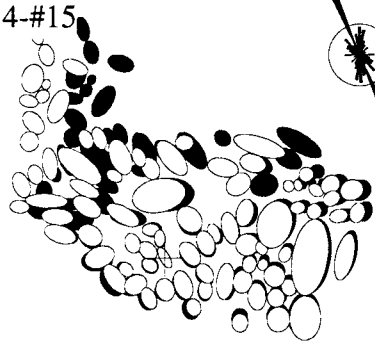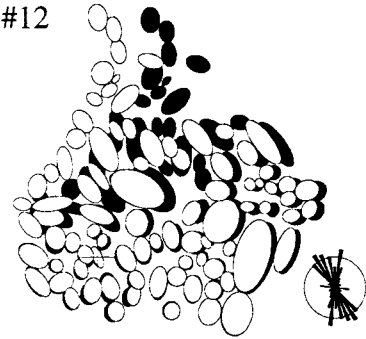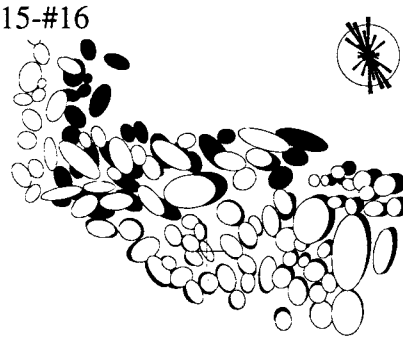#02-#03

#06-#07

#03-#04

#07-#08

#04-#05

#08-#09
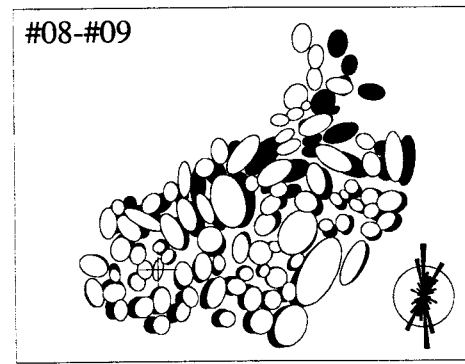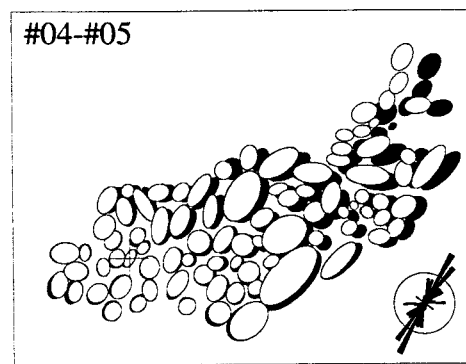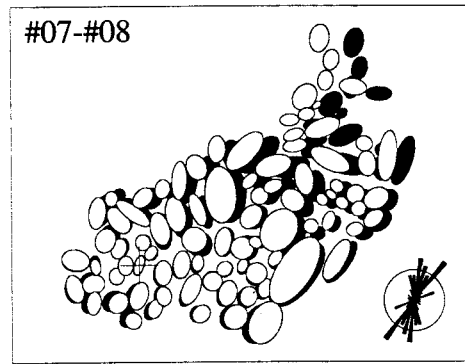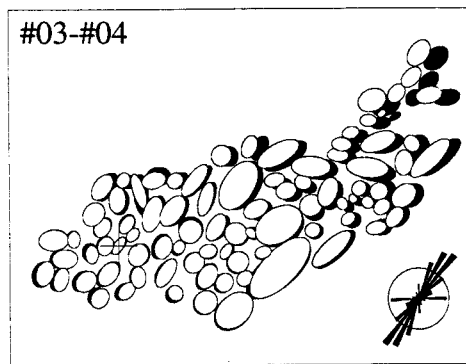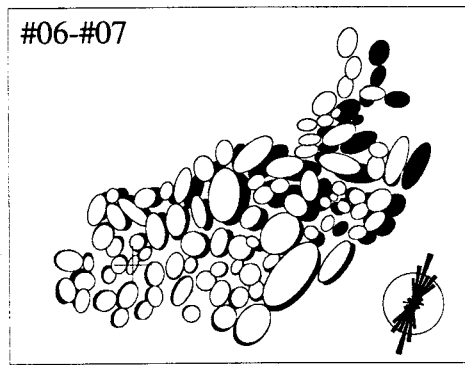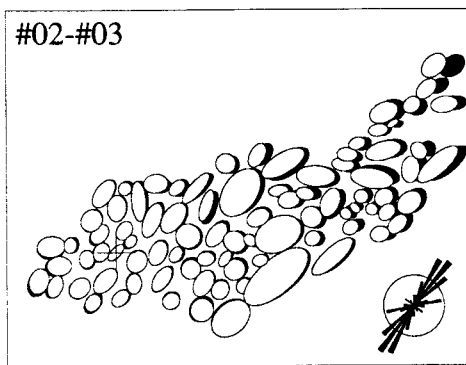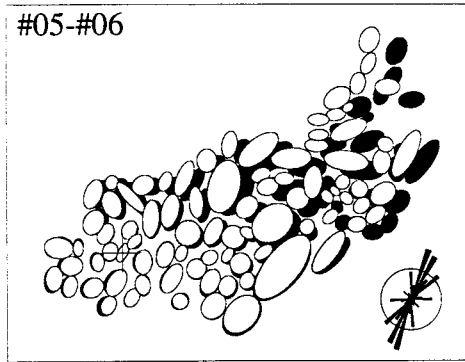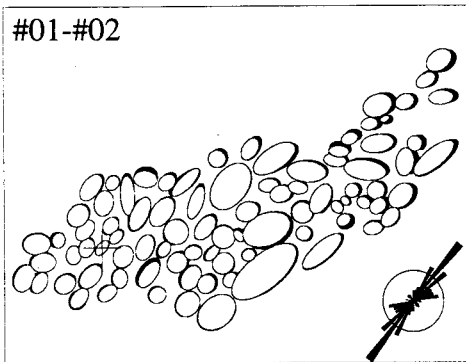
#09-#10
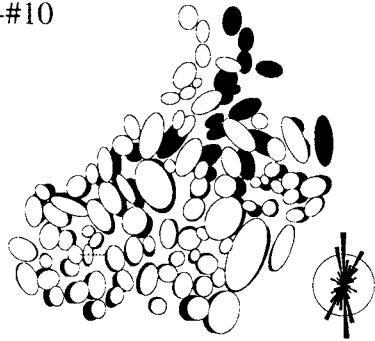
#13-#14

#10-#11

#14-#15

#11-#12

#15-#16

#12-#13

#16-#17

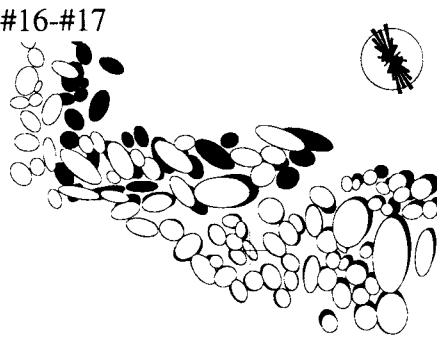Figure 3.6   Incremental displacement maps between pairs of stages.  Displacement of crystals is relative to the crystal 08 in Figure 3.3 (indicated by cross) and $X_1$ direction as defined in Figure 3.2.  The starting position of each displacement vector is indicated by a circle.

#01-#02

#05-#06

#02-#03

#06-#07

#03-#04

#07-#08

#04-#05
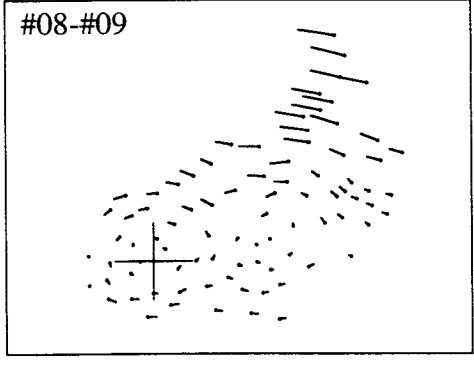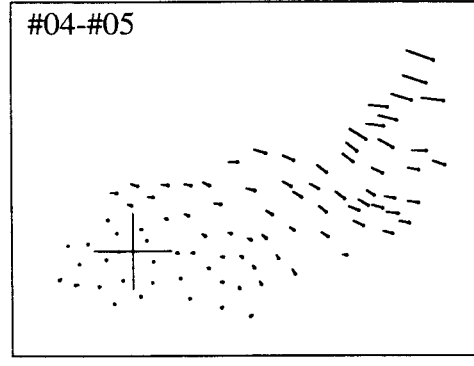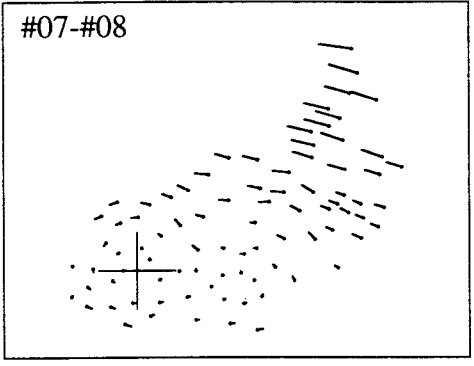
#08-#09

#09-#10

#13-#14

#10-#11

#14-#15

#11-#12

#15-#16

#12-#13

#16-#17
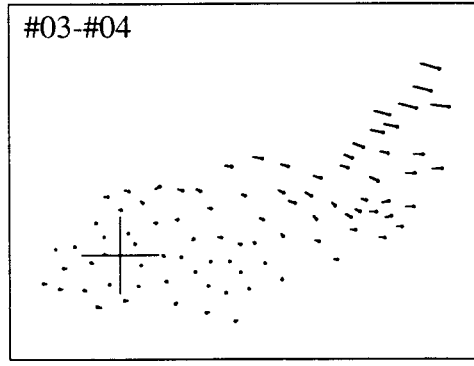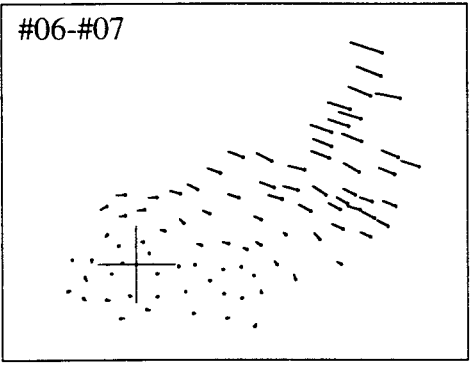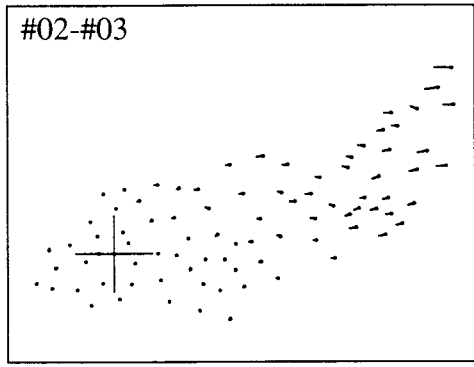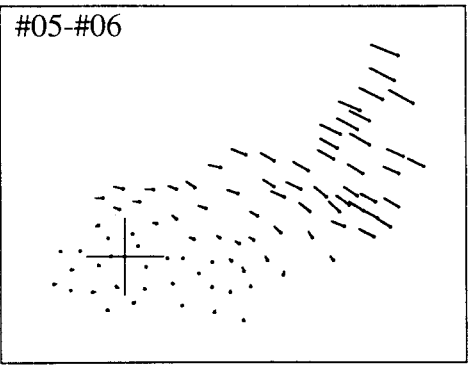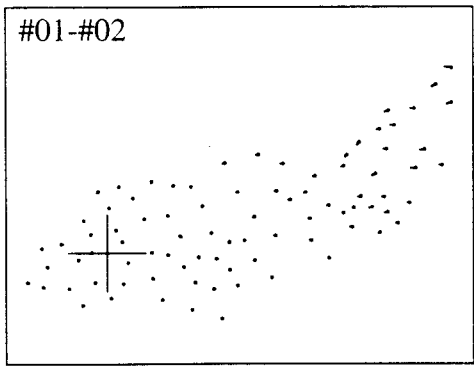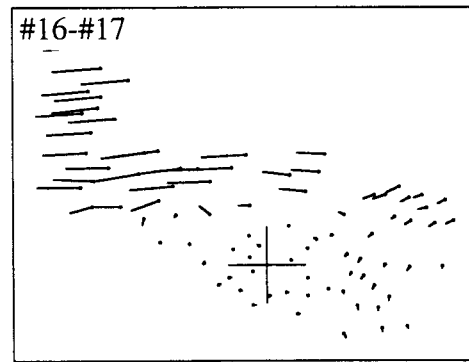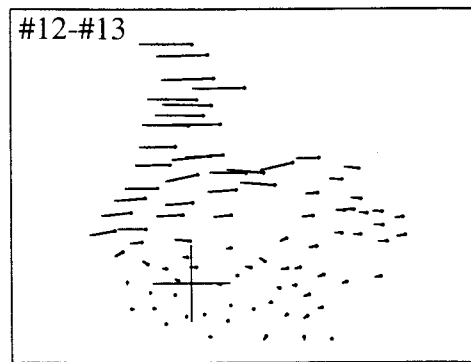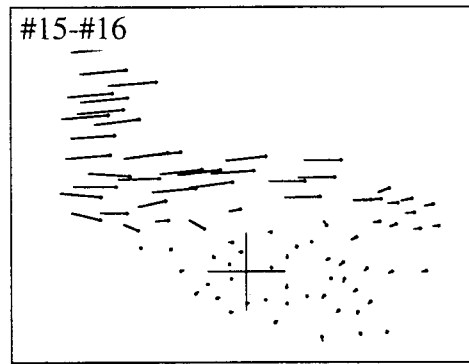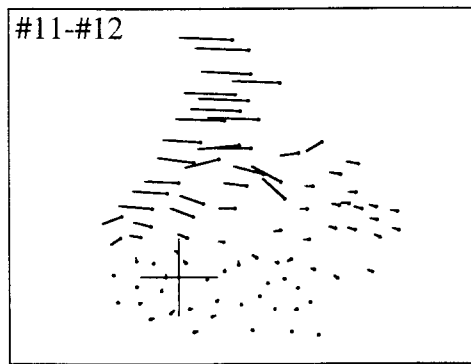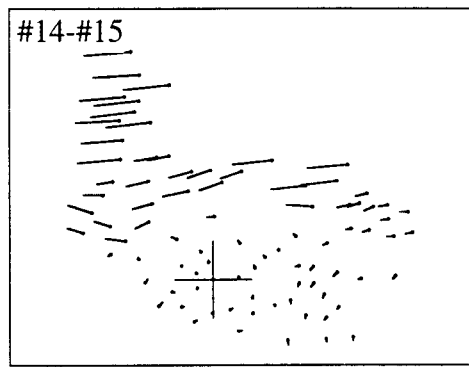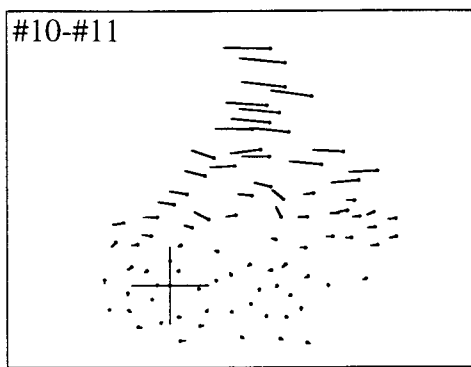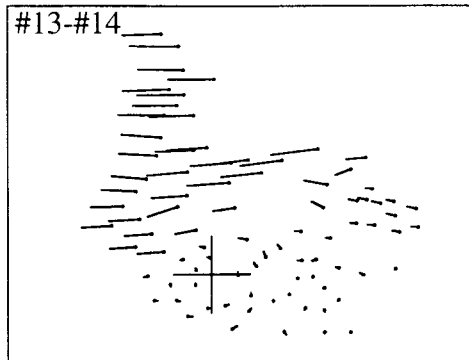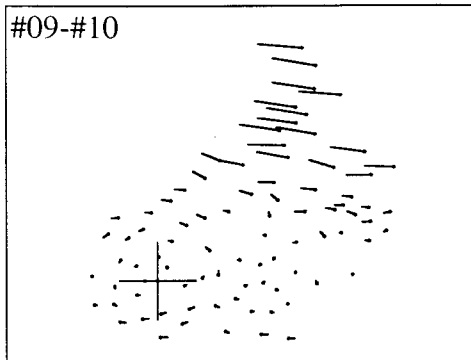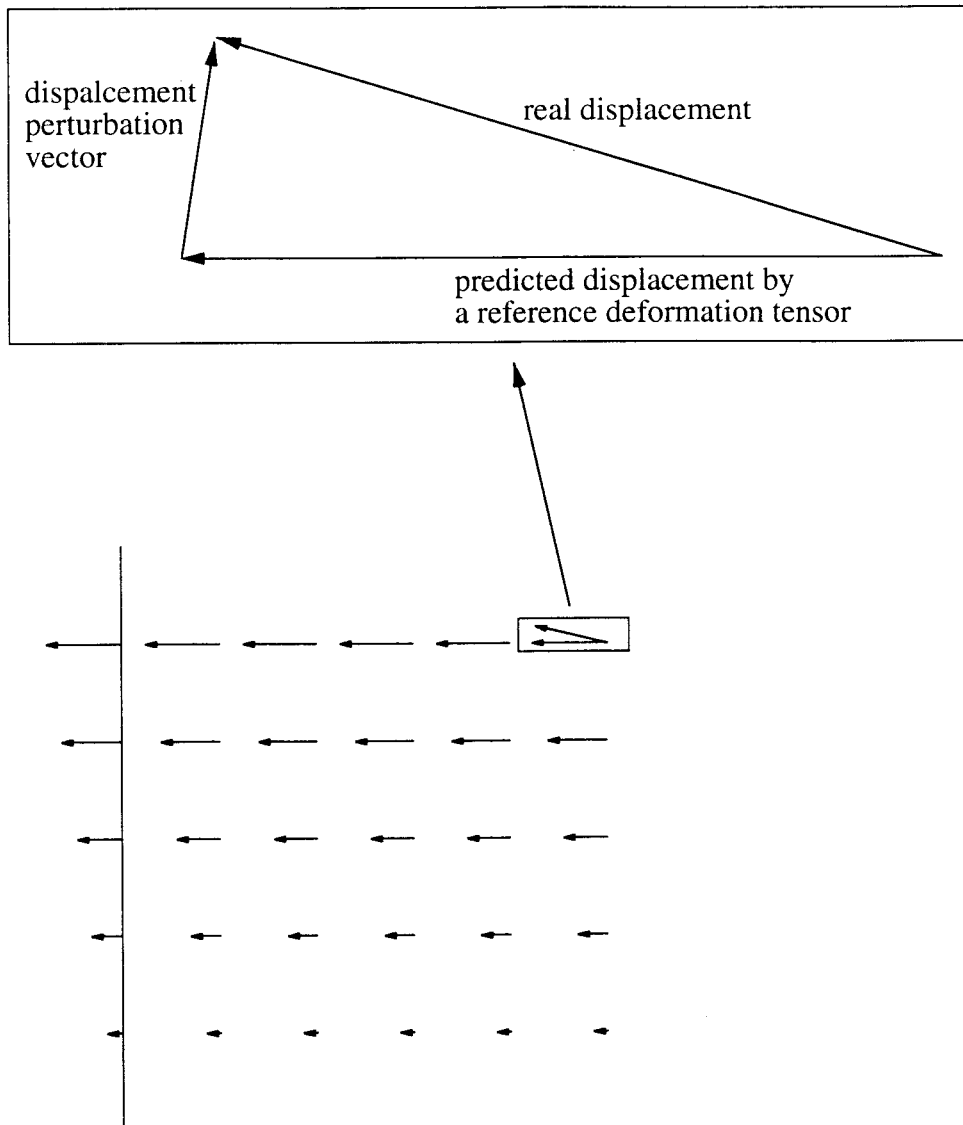
Figure 3.7    Definition of a displacement perturbation vector. The lower part shows a displacement field where all particles are changing their position according to a homogeneous deformation tensor. The position change of the particles in a real material can be described as the vector sum of the predicted displacement vector by the homogeneous deformation tensor and a displacement perturbation vector. Therefore, a displacement perturbation vector can be defined as a vector which connects from a final position predicted by the deformation tensor to a the final position actually reached by the particle.

Figure 3.8  Incremental displacement perturbation maps between stages.  Crystal 08 (Figure 3.3) was chosen as the origin, therefore showing no perturbation (indicated by cross).  The starting position of each vector is indicated by a circle.

#09-#10

#13-#14

#10-#11

#14-#15

#11-#12

#15-#16

#12-#13

#16-#17
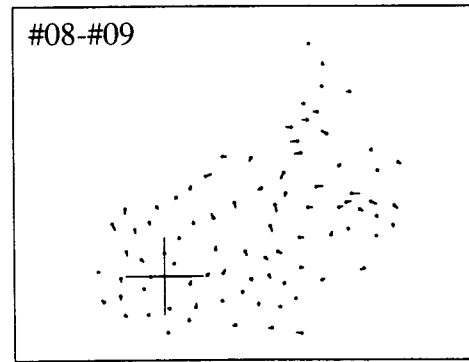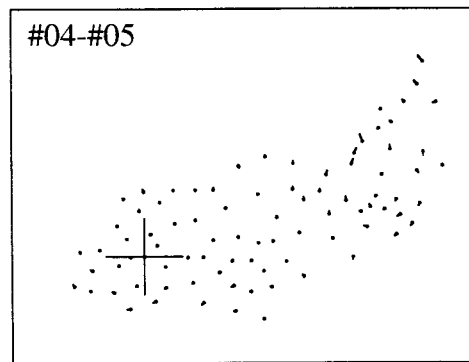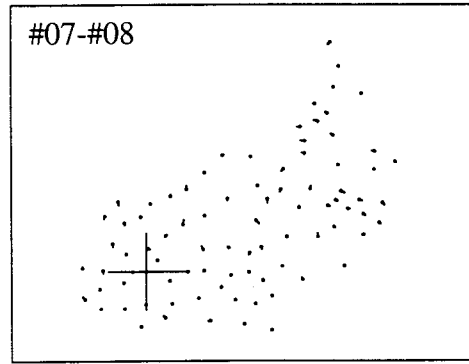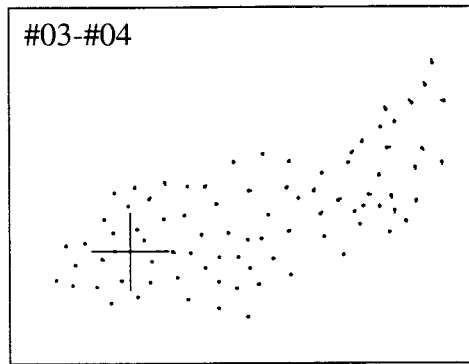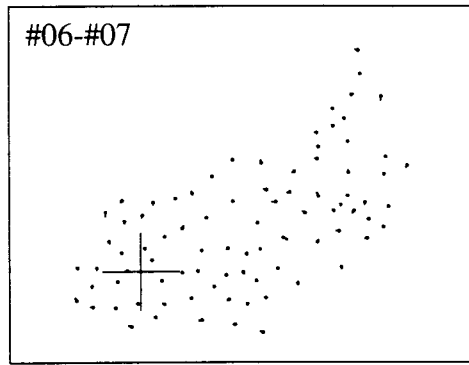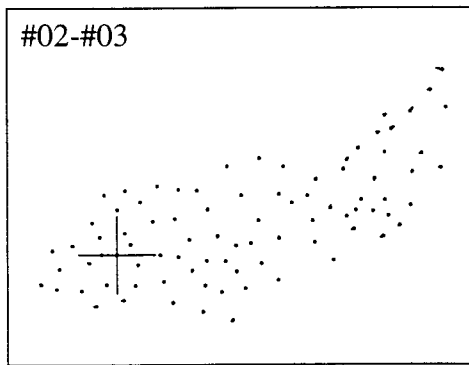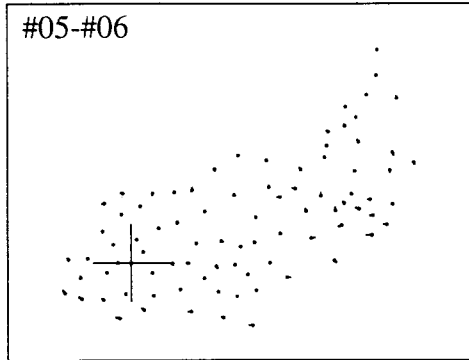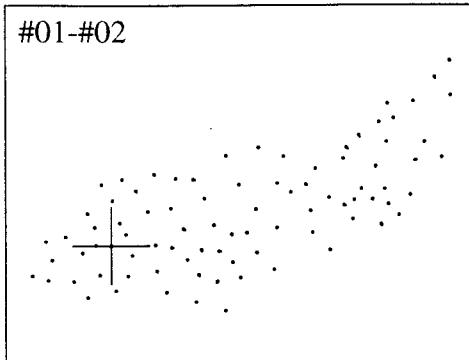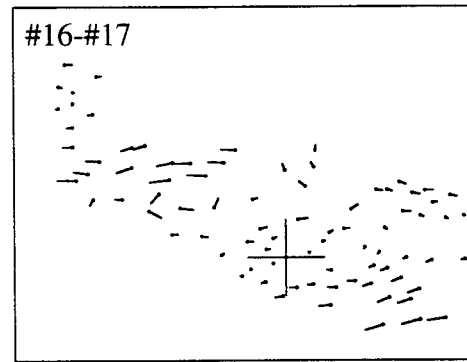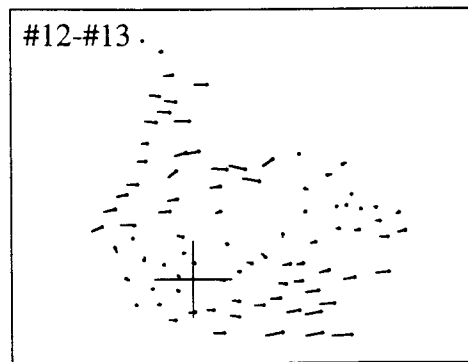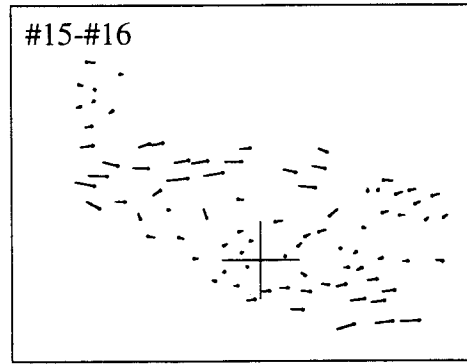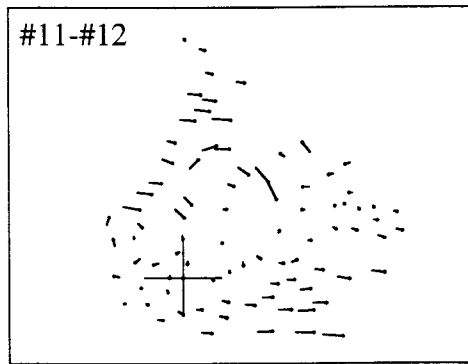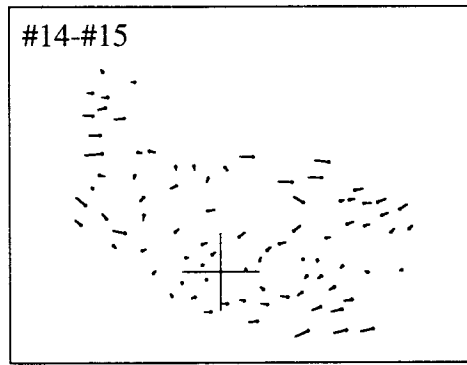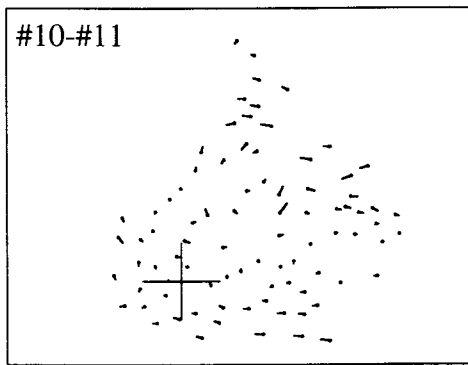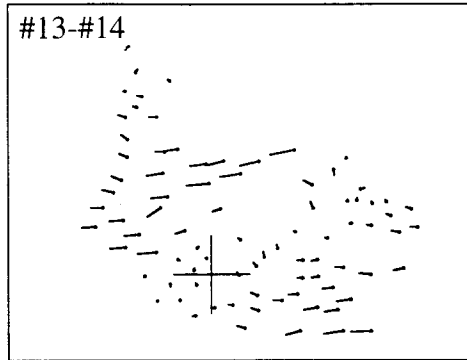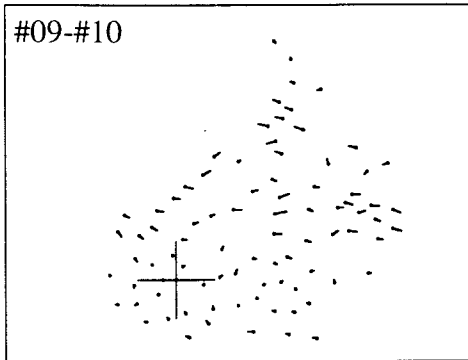
Figure 3.9   Mixing of the white phase crystals.   From top, photomicrograph #01, photomicrograph #19, displacement map relative to the crystal 81 (observed), displacement map relative to the crystal 81 (constructed after assuming shear strain of -4), and displacement perturbation map.
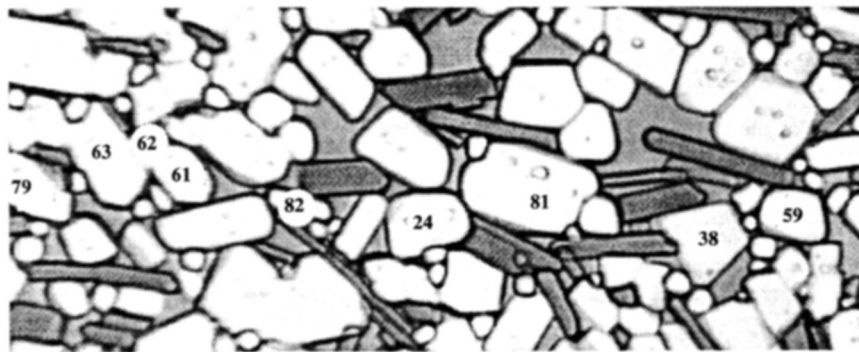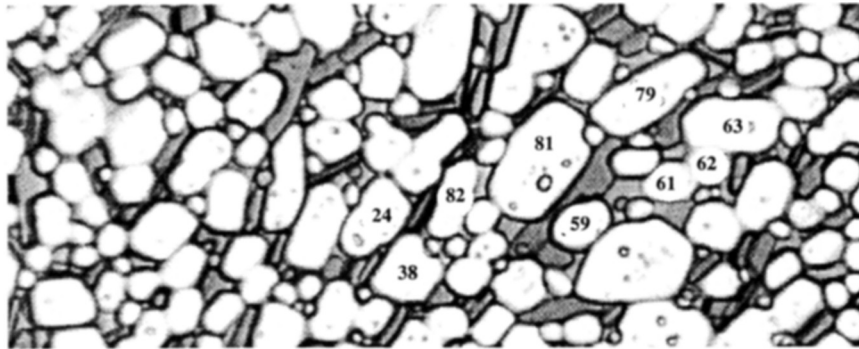
real displacement
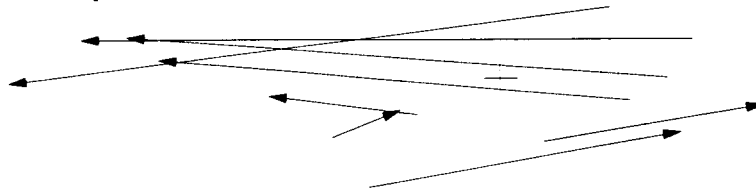


predicted displacement by a reference deformation tensor
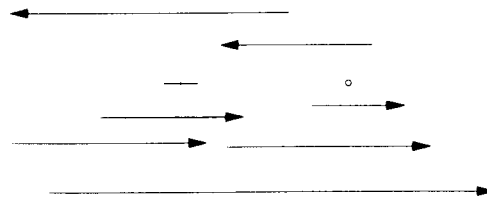


displacement perturbation vector
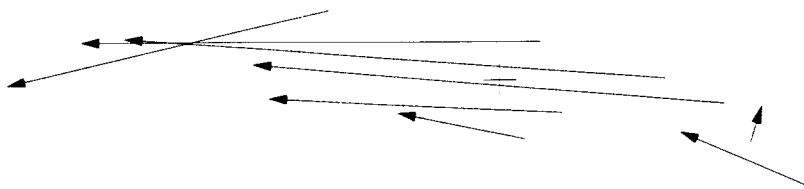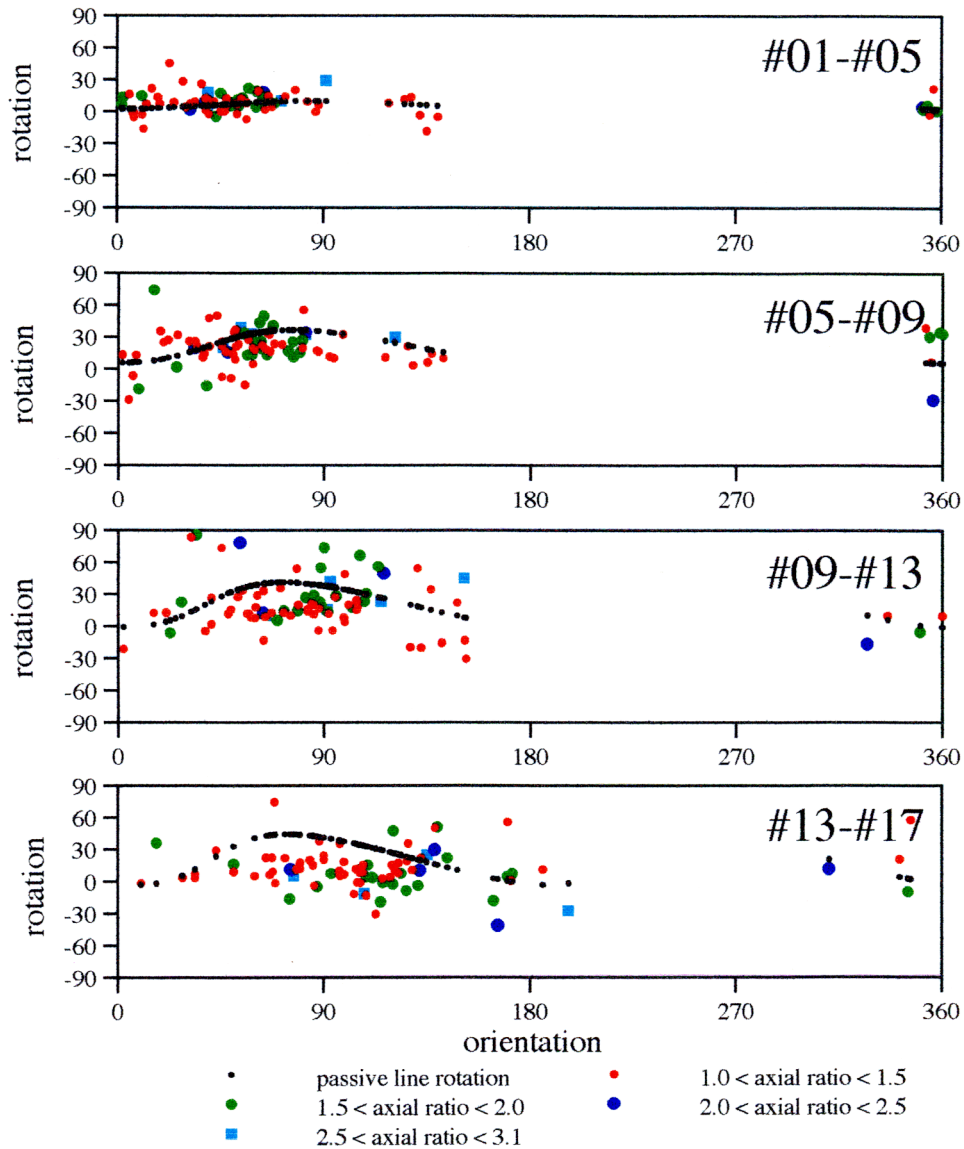
Figure 3.10 Plots of predicted passive line rotation (black symbol) vs. measured rotation of crystals. For example, one crystal of ~90° orientation in #01-#05, rotates about 30° counter clockwise (cyan box symbol, indicating the axial ratio of 2.5~3.1), while the predicted rotation of a passive line at the same orientation is about 10° counter clockwise (black symbol). Calculation of the predicted rotation was made by applying a deformation tensor calculated using the displacement of the white phase crystals (08, 81, & 44 in Figure 3.3) to the long axes of all the crystals.
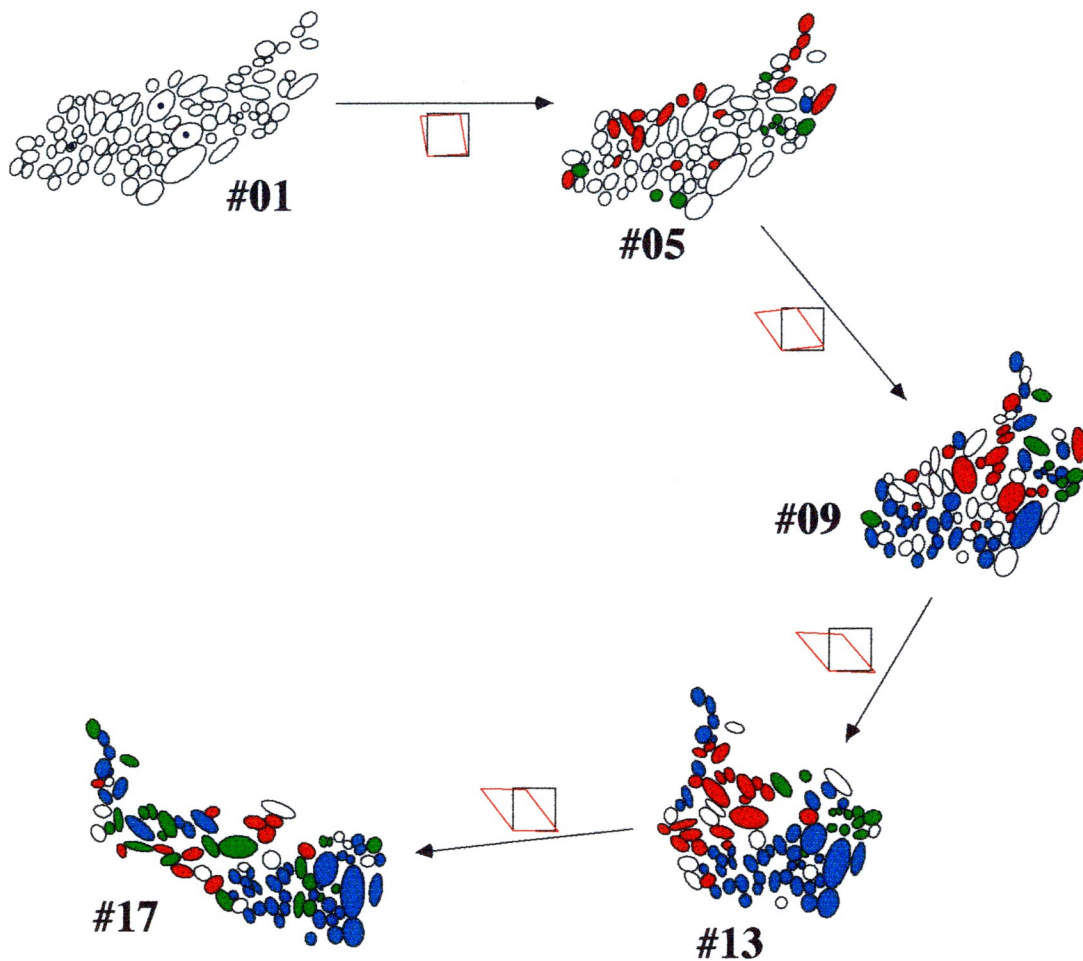
Figure 3.11 Spatial distribution of rotational behavior of white phase crystals. The white phase crystals (08, 81 & 44) were used to calculate a deformation tensor. Squares and deformed squares represent the incremental deformation. White: measured rotation within ± 7.5° of calculated rotation of a passive line. Red: measured rotation is larger than the calculated rotation of a passive line, at least by 7.5°. Blue: measured rotation is smaller than the calculated rotation of a passive line at least by 7.5°, but rotation sense is same as the passive line. Green: crystals rotating in opposite sense, at least by 7.5°.
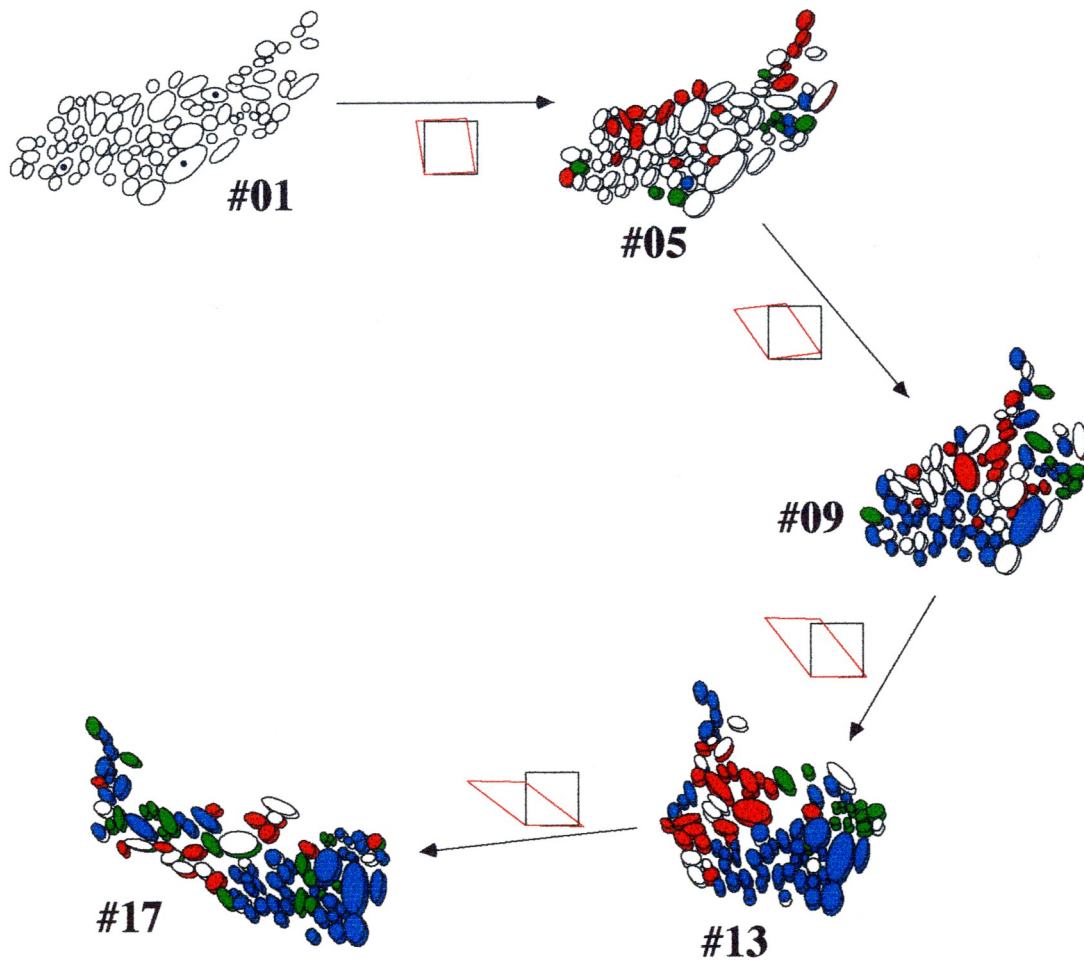
Figure 3.12 Similar diagram to Figure 3.11, using different white phase crystals (07, 41, & 63) to calculate a deformation tensor. Underlying crystals are from Figure 3.11.

#01

#05

#09

#13

#17
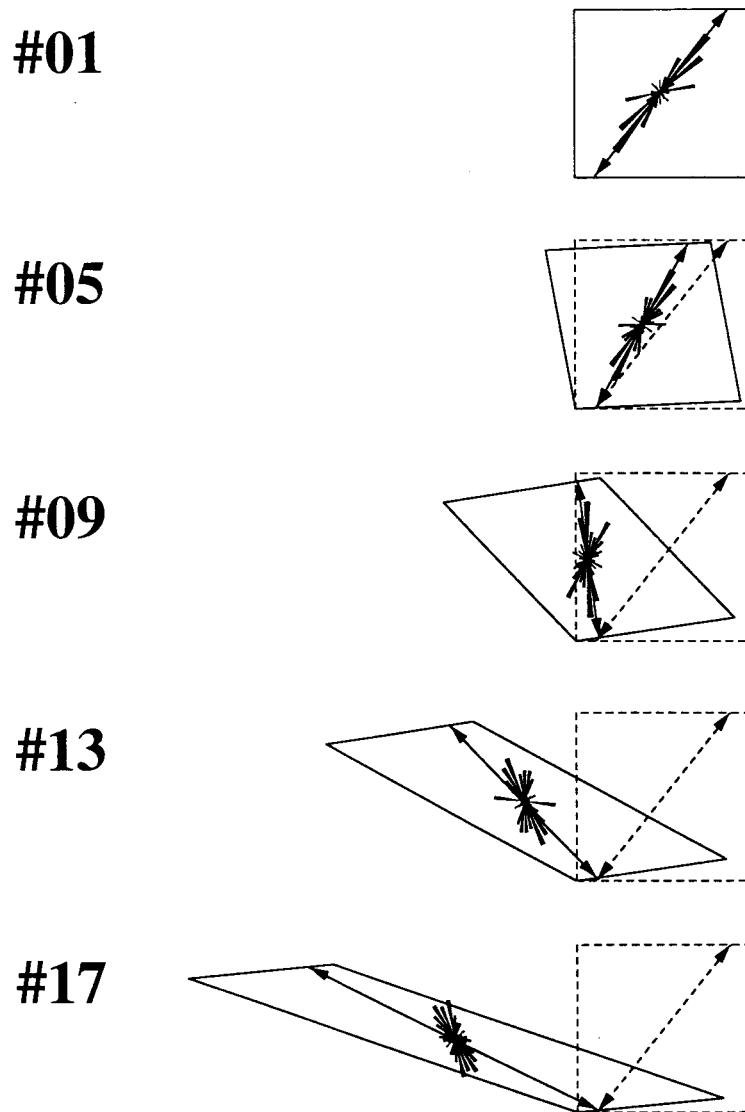
Figure 3.13 Comparison of the shape fabric orientation modification with the passive line orientation. Squares represent undeformed state at stage #01 and parallelograms represent deformed squares calculated by the white phase crystals 08, 81, & 44 in Figure 3.3. The maximum density of shape fabric starts to lag behind the passive line from the stage #13.

3-34
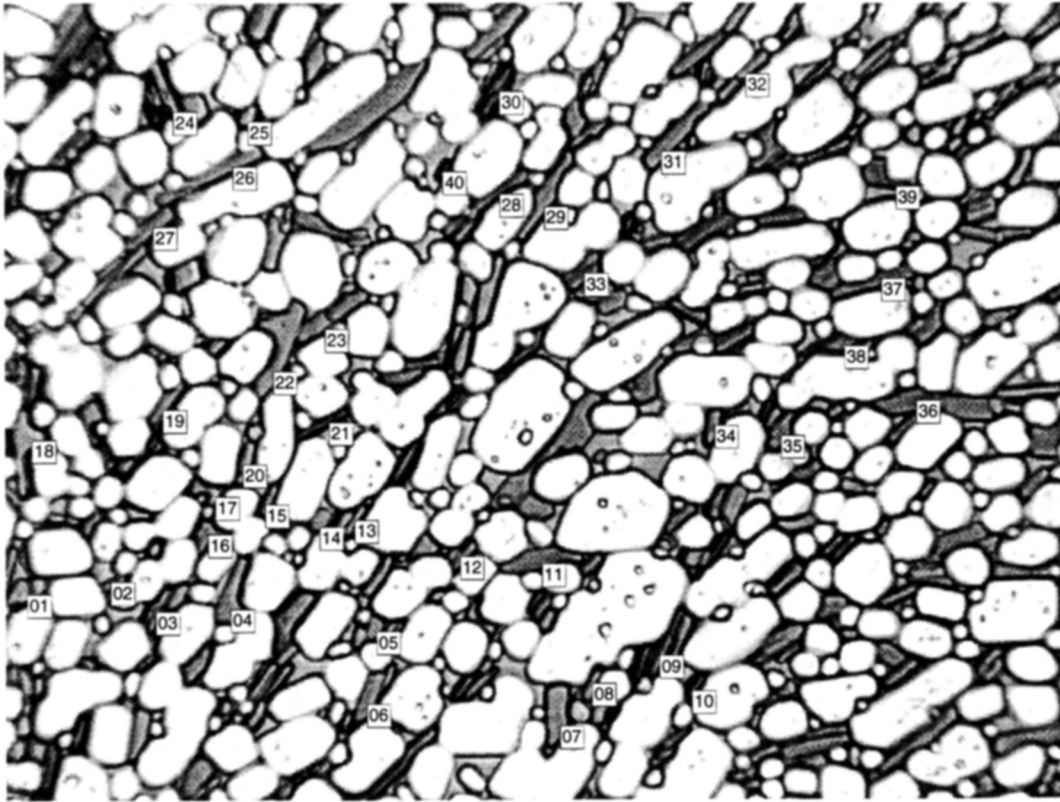
Figure 3.14  Photomicrograph #01 with labels of blue crystals used for orientation and length measurement.  The labeled crystals are the crystals which touch the upper left corner of the box containing the label.
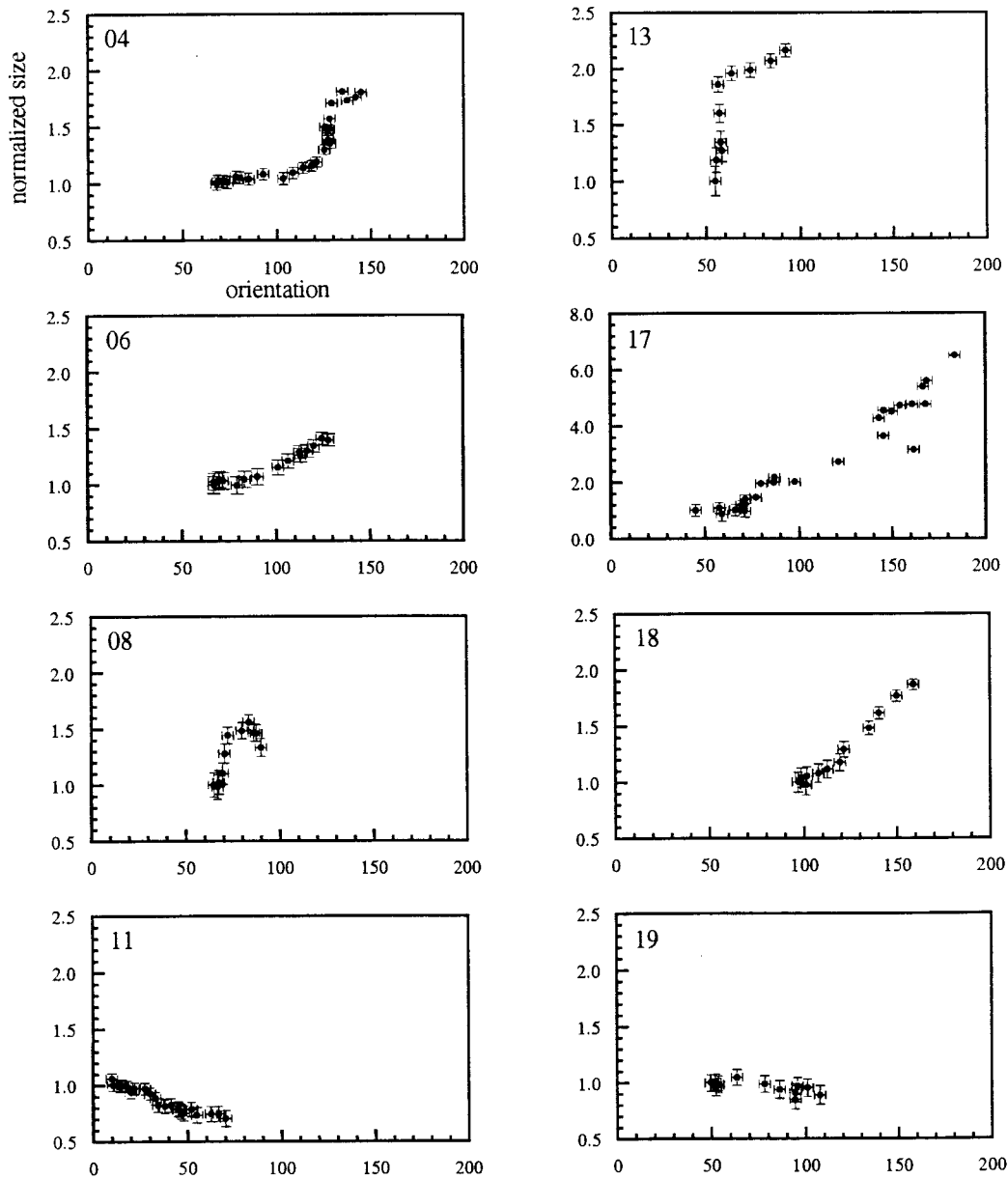
Figure 3.15 Orientation vs. normalized length plot for the blue phase crystals of Figure 3.14. Crystal labels are shown in upper left of each graph. The crystal length is normalized to the crystal length in photo #01. Orientation is measured counter clockwise from positive $X_1$ direction (defined in Figure 3.2).
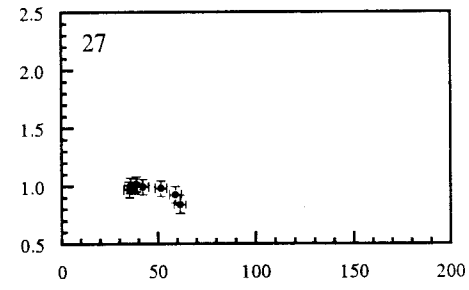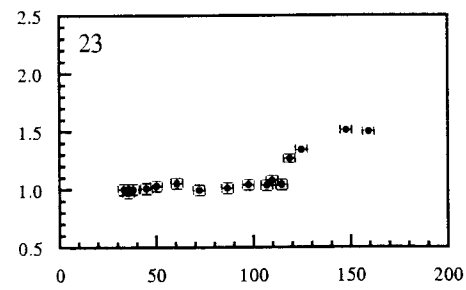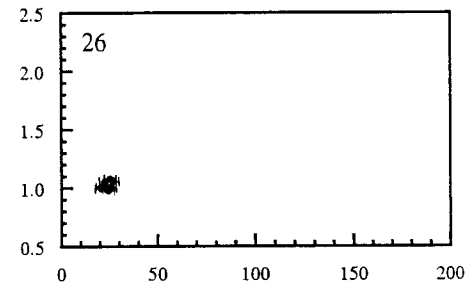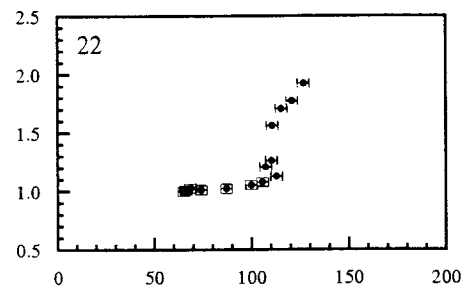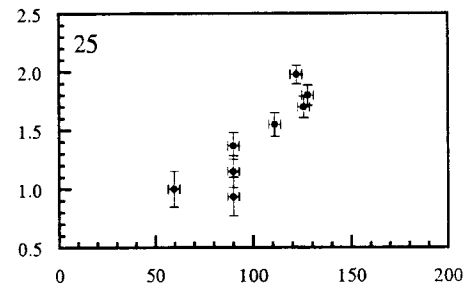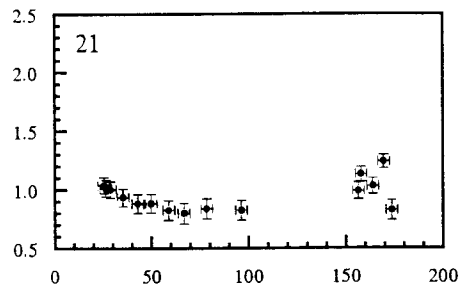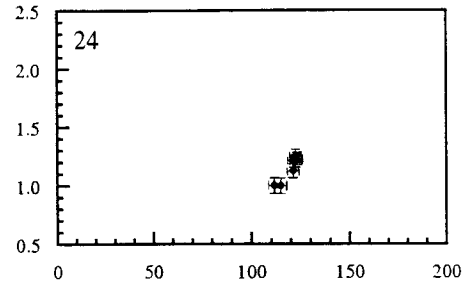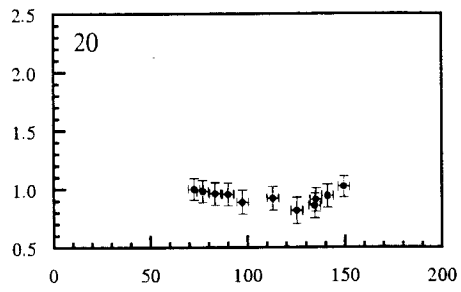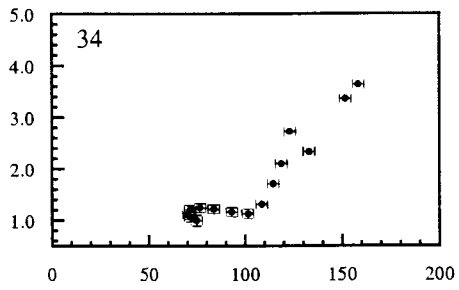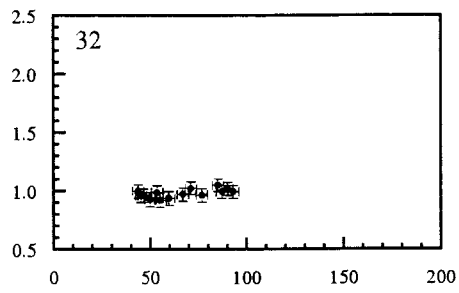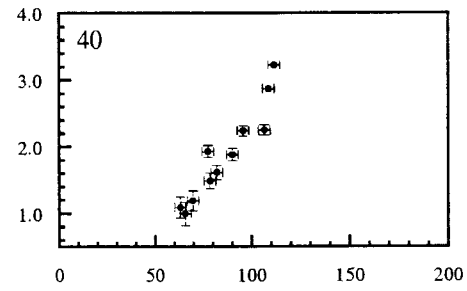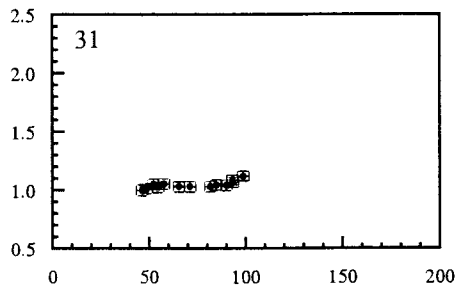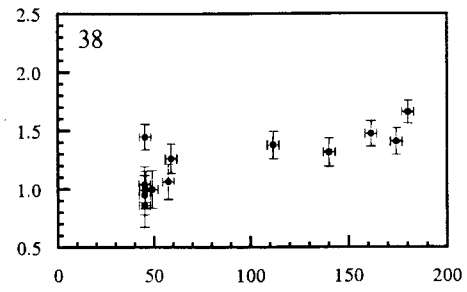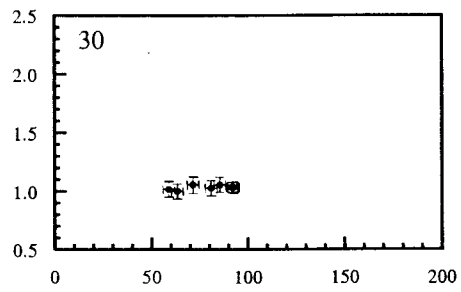
Figure 3.16 Growth and dissolution of blue phase crystals during isothermal deformation. Top row: blue phase crystal 22 showing rapid growth when the fast growth direction (along c-axis) rotates past an orientation of about 110° (see also Figure 3.15). Second row: blue phase crystal 34, showing similar behavior as the blue phase crystal 22. Third row: blue phase crystal 21, showing slight dissolution at end(s) when its long axis is in the shortening field. Fourth row: blue phase crystal, showing dissolution at side(s) (#16-#19) when the long axis is nearly parallel to the instantaneous stretching axis. Fifth row: blue phase crystal, showing dissolution at an unexpected orientation with respect to the bulk stretching and shortening axis. Sixth row: blue phase crystal, showing segmentation and different rotation of the two segments when the long axis is nearly parallel to the instantaneous shortening axis. Scale bar: 50 μm.
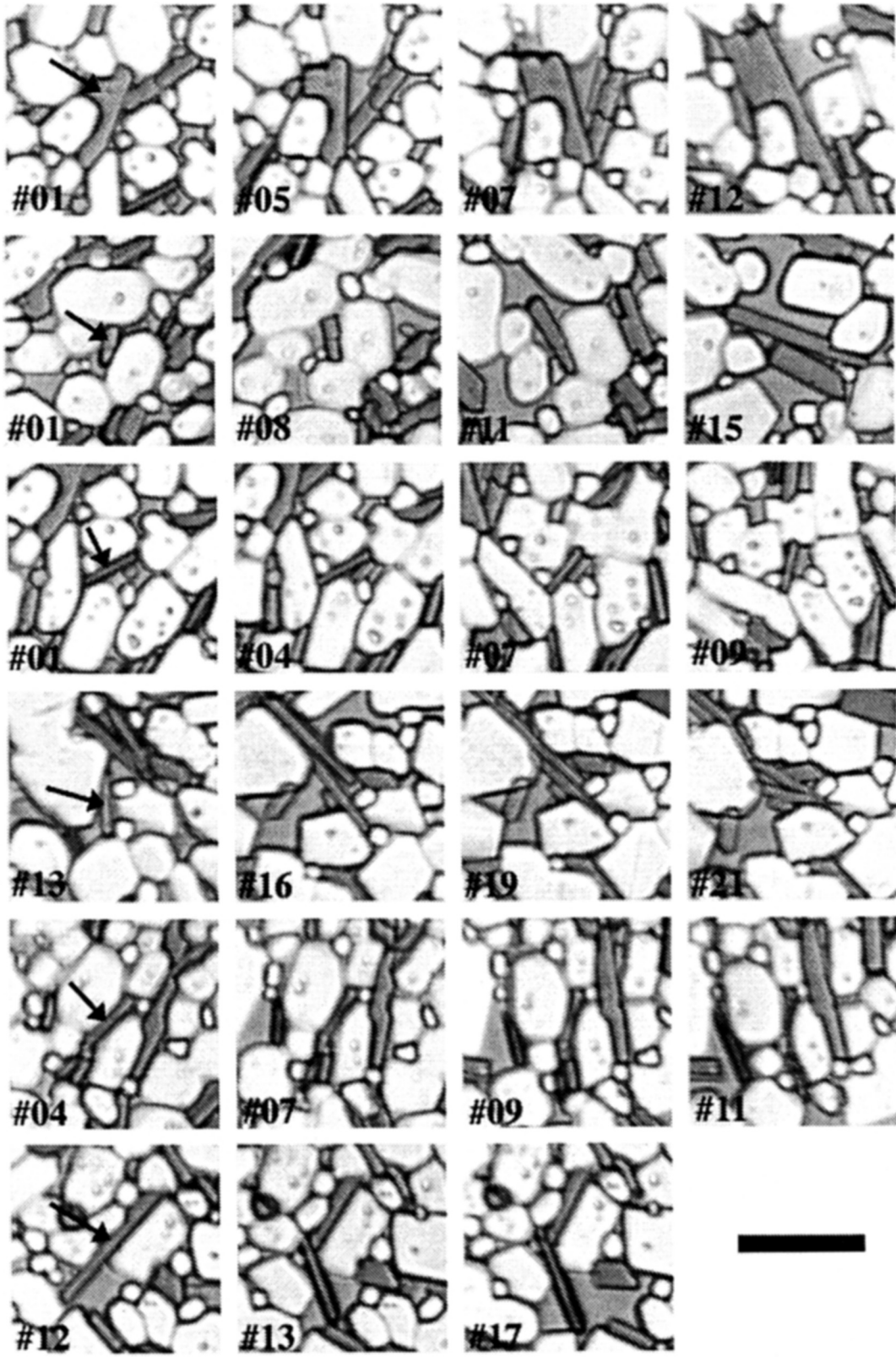
Figure 3.17 Results from a computer model that calculates orientation dependent crystal growth, assuming anisotropic crystal growth and preferential growth toward the stretching directions and no dissolution at the shortening regime. Mohr circle representation of the counter clockwise simple shearing (P: pole point in Mohr space). A crystal oriented about 30 degrees counter clockwise from the positive $X_1$ direction shortens until the orientation becomes perpendicular to the $X_1$ direction and then starts to lengthen. Upper two graphs: rotation rate and elongation rate history of a material line which was initially oriented at $5°$ counter clockwise from $X_1$ direction. Notice that the time period for the relatively faster elongation rate is short because of the fast rotation rate. Lower graph: plot of orientation vs. length (no length change for negative elongation rate is assumed in the model). Three arrows in the graphs indicate the same orientation of the material line. Although the general pattern is similar to the some of the observation from the blue phase crystals, the result from calculation shows no rapid growth at the orientation of instantaneously stretching axis, because of the relatively faster rotation rate at around the stretching axis.
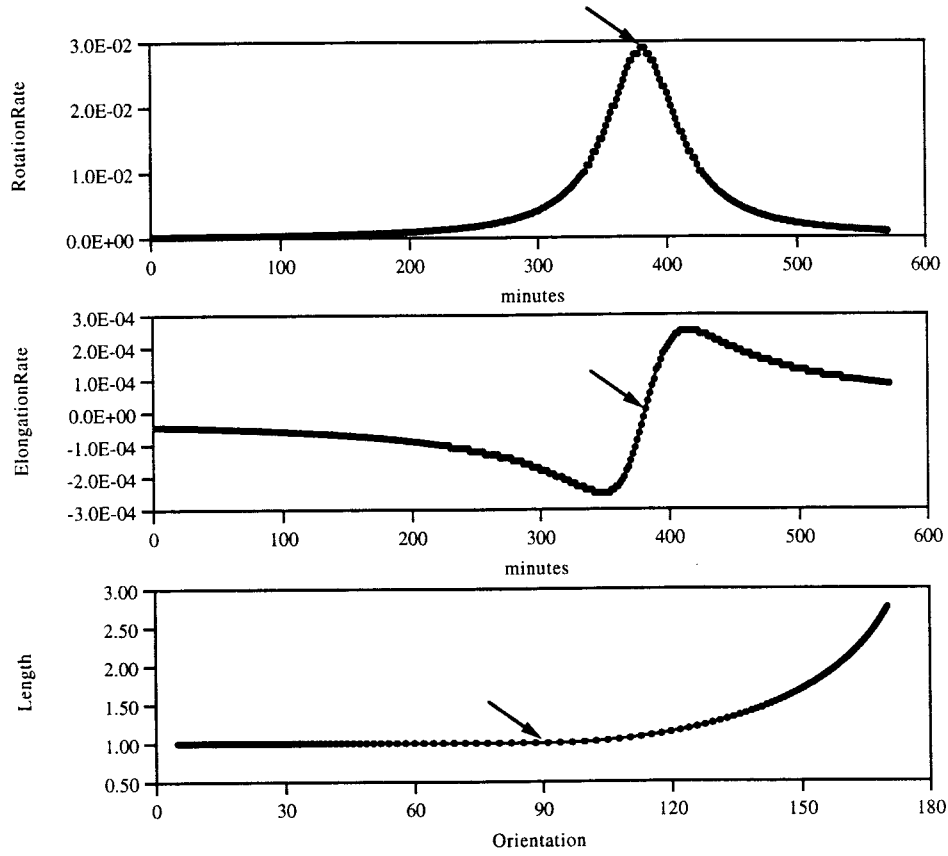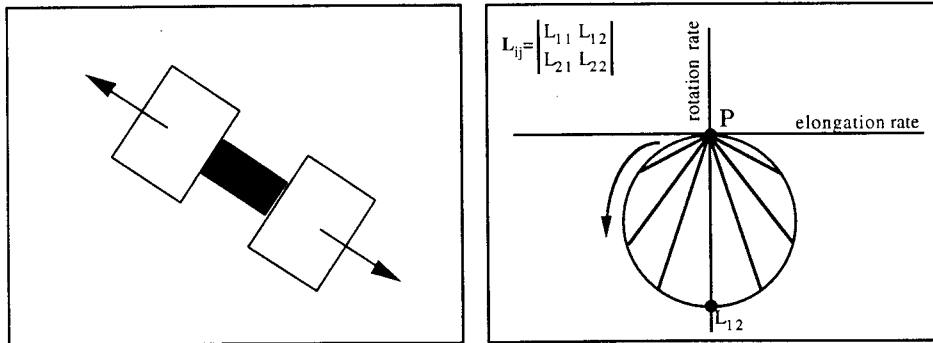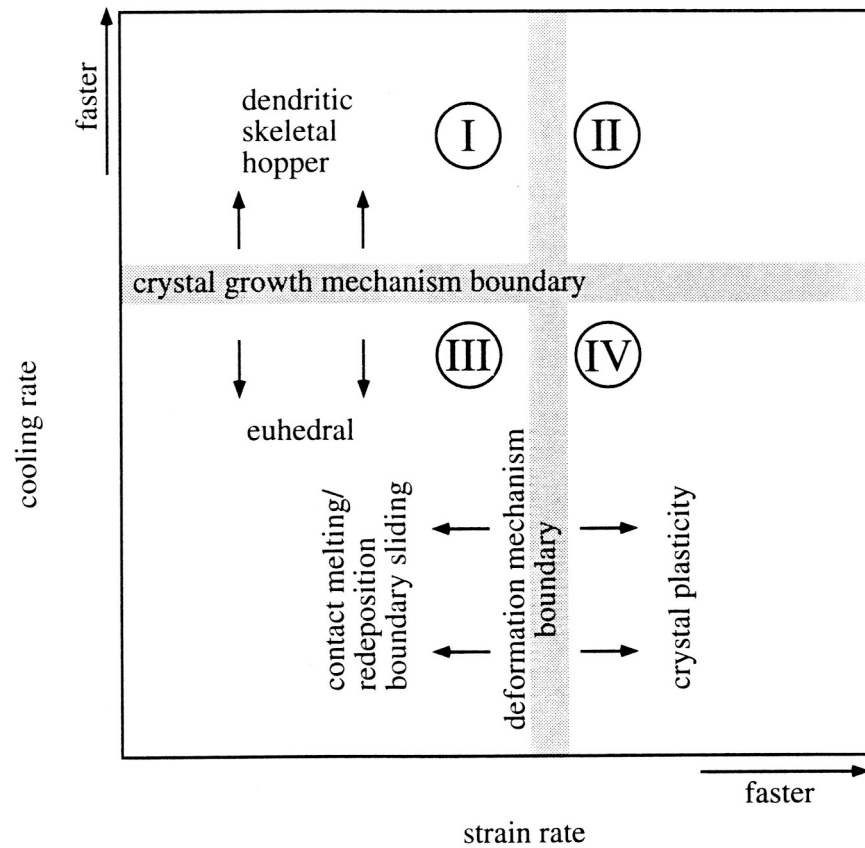
Figure 4.1 Crystal growth mechanisms and deformation mechanisms in framework crystal-melt mixtures, depending on cooling rate and strain rate. The correspondence of the mechanisms to the rates are only true for a given condition. For example, when melt fraction decreases during cooling, the field of crystal plasticity may expand. Therefore, the diagram only describes *instantaneous* microstructural changes by operating mechanisms at a given condition.

Figure 4.2   Crystal growth (the blue phase crystal near the center) during dextral shearing. (a) t=0 minutes & 38 °C. (b) t=1 hour 24 minutes & 32 °C. (c) t=3 hours 28 minutes & 28 °C. (d) t=5 hours 14 minutes & 28 °C. (e) t=7 hours 7 minutes & 28 °C. (f) t=8 hours 17 minutes & 28 °C. Plane polarized light. Field width: 0.13 mm.
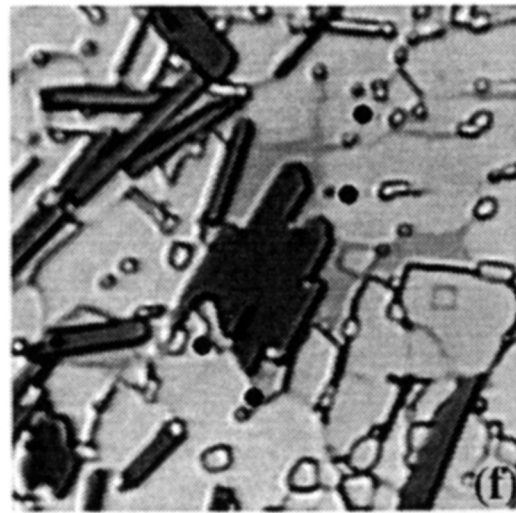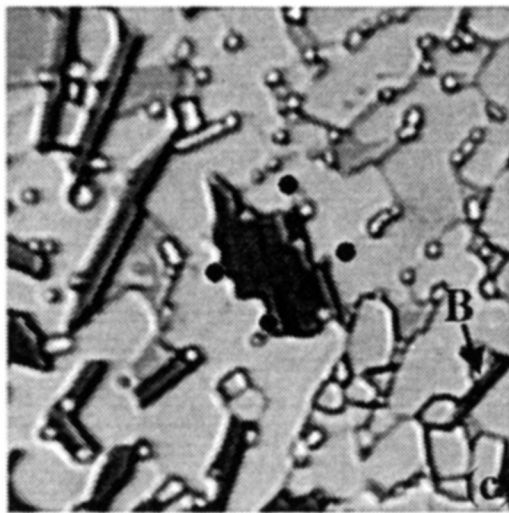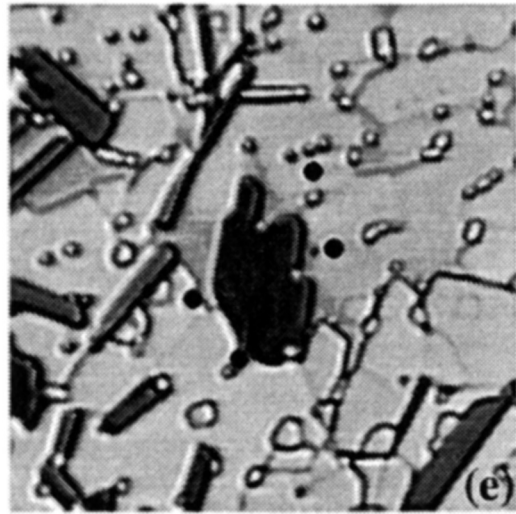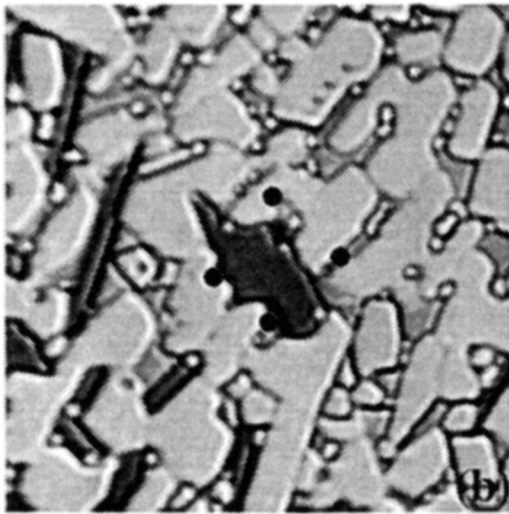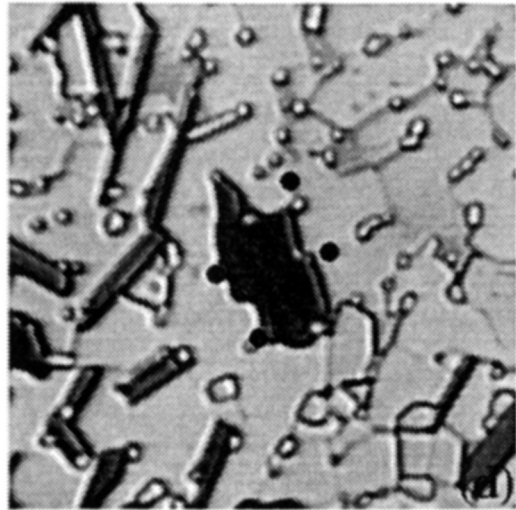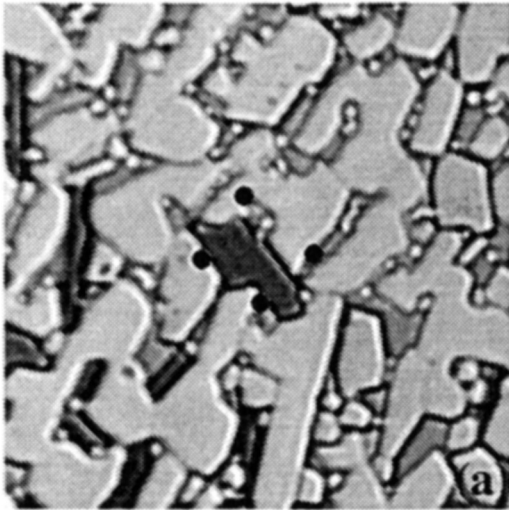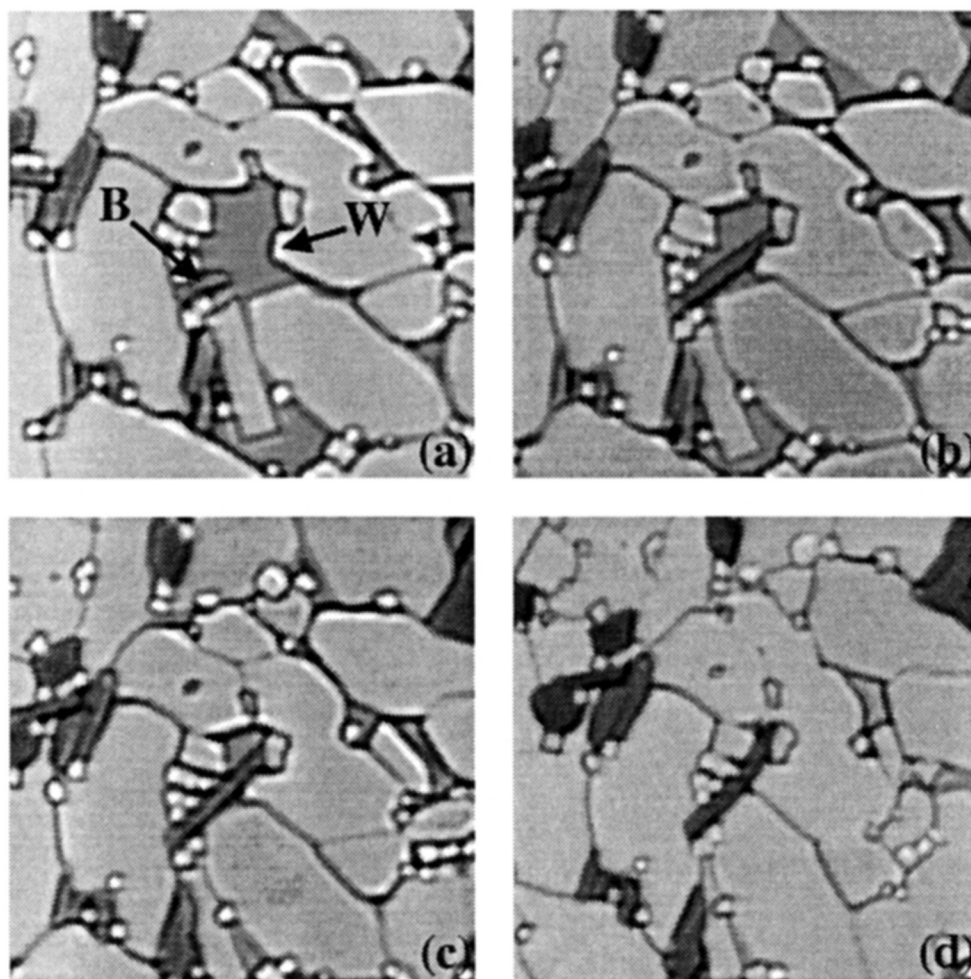
Figure 4.3 Crystal growth of blue phase and white phase crystals around a melt pocket and bending of the blue phase crystal (B) during collapse of the melt pocket by pure shearing. (a) t=0 minutes & 40 °C. (b) t=1 hour 32 minutes & 37 °C. (c) t=4 hours 9 minutes & 32 °C. (d) t=8 hours 15 minutes & 28 °C. Shortening direction: horizontal. Plane polarized light. Field width: 0.1 mm.

Figure 4.4   Contact melting of the white phase crystal (W) during cooling and sinistral shearing (indicated by lines in a & f).  Contact melting of W occurs at the boundary between the blue phase crystal (B2) and W.  Phase boundary migration (blue phase crystal B1) is also observed in this field of view.  (a) t=0 hours & 79 °C.  (b) t=13 hours & 71 °C.  (c) t=25 hours & 64 °C.  (d) t=38 hours & 56 °C.  (e) t=55 hours & 46 °C.  (f) t=67 hours & 39 °C.  Plane polarized light.  Field width: 0.15 mm.
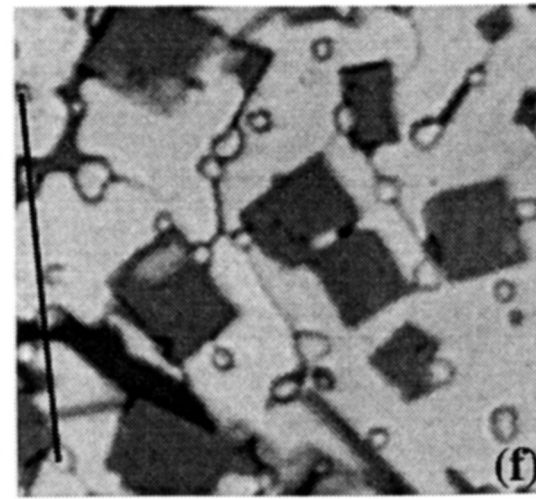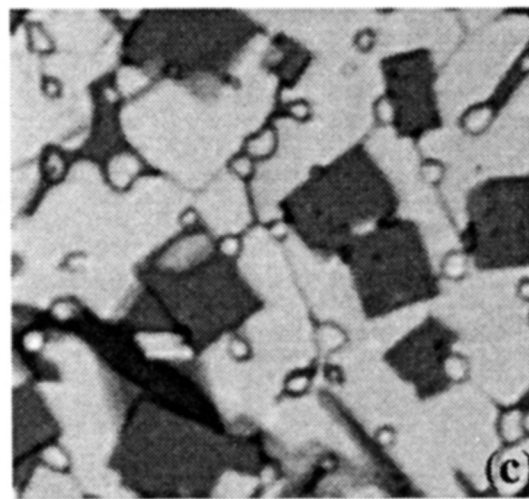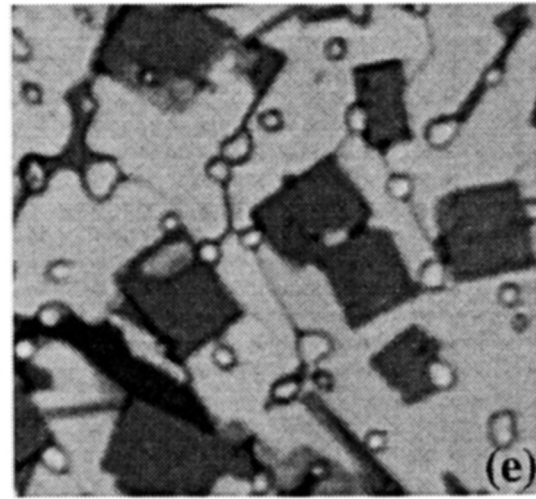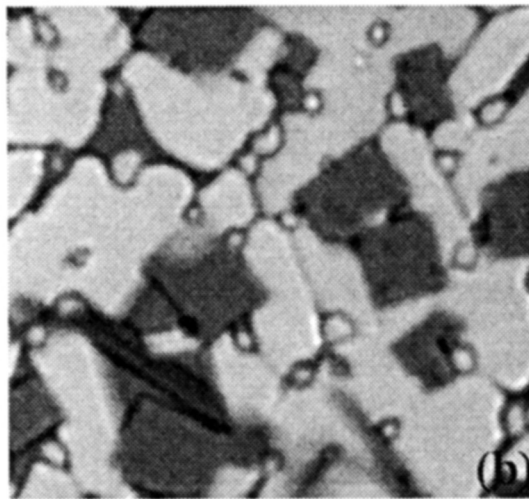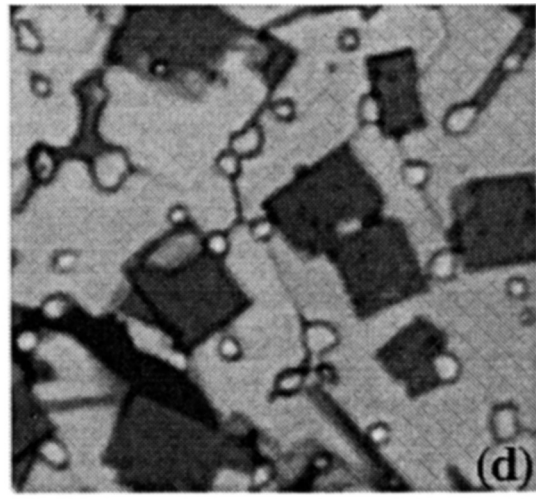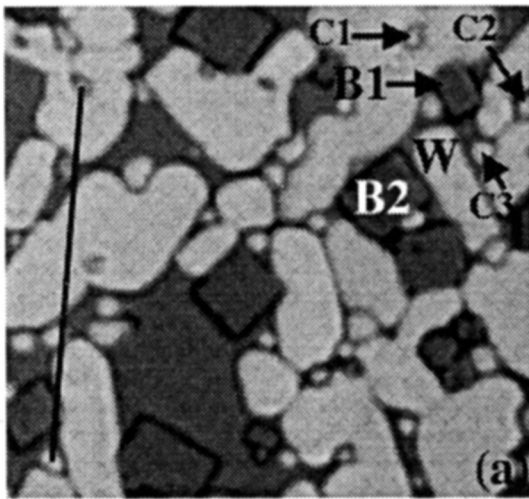
Figure 4.5    Development of a high strain rate zone during partial melting and sinistral shearing.  (a) t=0 minutes & 35 °C.  (b) t=16 minutes & 37 °C.  (c) t=31 minutes & °38C.  (d) t=46 minutes & 39 °C.  (e) t=1 hour 1 minute & 40 °C.  (f) t=1 hour 16 minutes & 41 °C.  (g) t=1 hour 31 minutes & 42 °C.  (h) t=1 hour 46 minutes & 43 °C.  (i) t=2 hours 1 minute & 44 °C.  (j) t=2 hours 16 minutes & 45 °C.  (k) t=2 hours 31 minutes & 46 °C.  (l) t=2 hours 48 minutes & 47 °C.  (m) t=3 hours 3 minutes & 48 °C.  (n) t=3 hours 19 minutes & 49 °C.  (o) t=3 hours 34 minutes & 50 °C.  (p) t=3 hours 49 minutes & 51 °C.  Cube phase crystals (a, f, & k), indicated by arrow, are the origins for displacement maps in Figure 4.6.  Plane polarized light.  Field width: 0.4 mm.

4-15
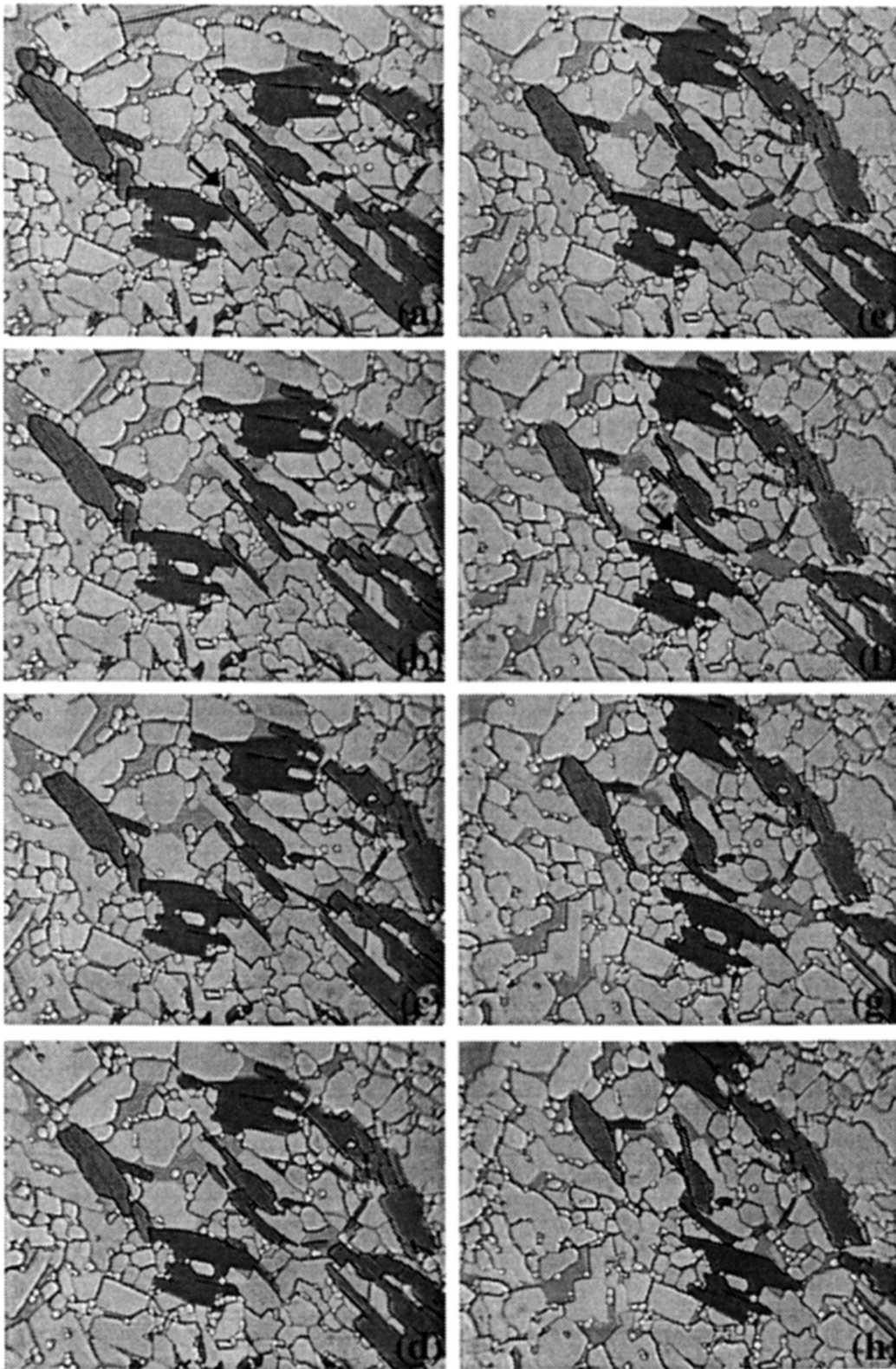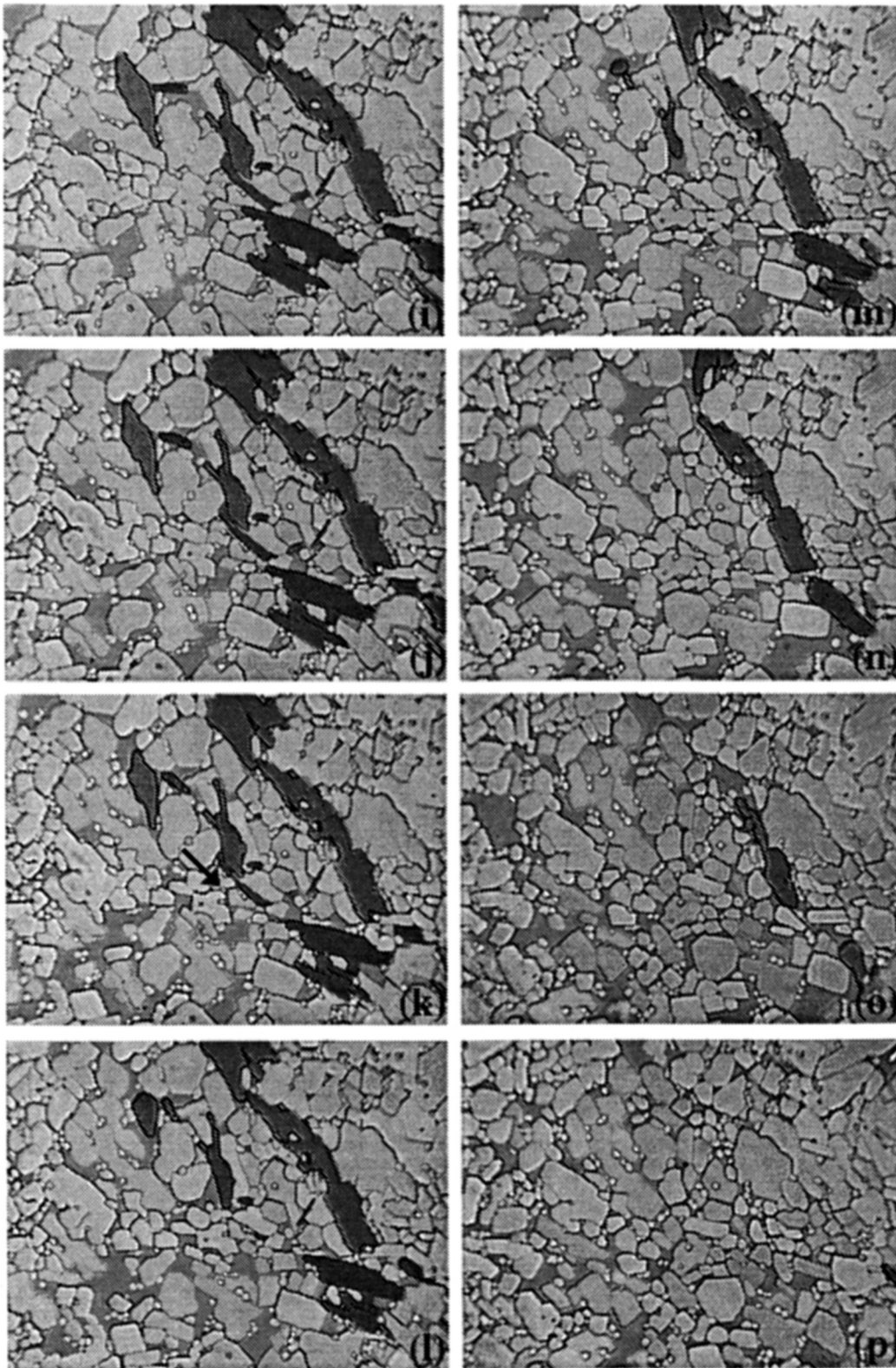
Figure 4.6    Particle trajectories from Figure 4.5 (the left maps) and particle trajectories with superimposed blue phase crystal boundaries (the right maps).  (a) constructed from Figure 5a, b, c, d, & e, relative to Figure 5a.  (b) constructed from Figure 5f, g, h, i, & j, relative to Figure 5f.  (c) constructed from Figure 5k, l, m, n, o, & p, relative to Figure 5k.  Squares represent the initial positions of material points.  The stippled region in the right-hand diagrams represents the blue phase crystals at the initial stage for each particle trajectory.  The region bounded by thicker lines represents the blue phase crystals at the last stage for each displacement map.
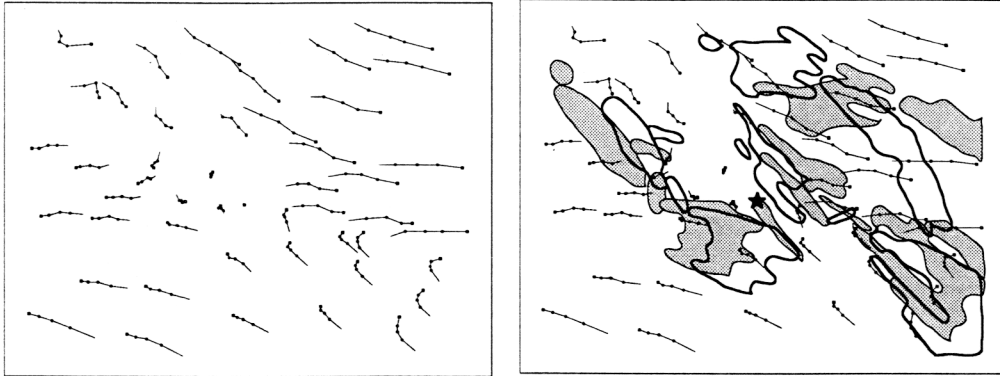
(a)
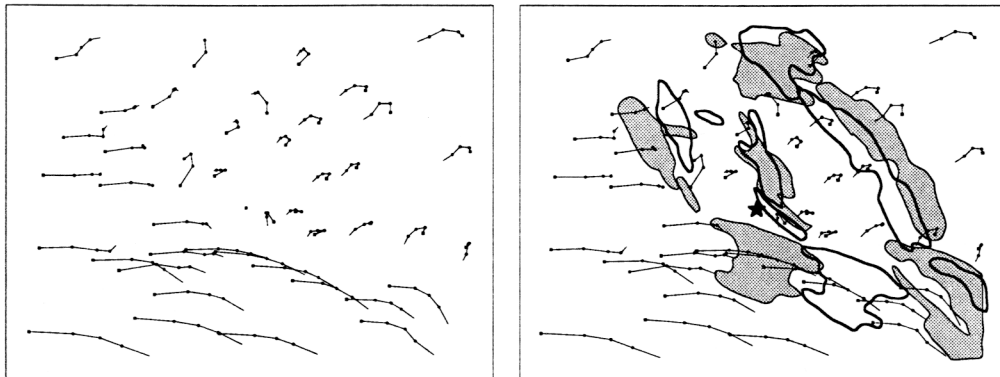
(b)
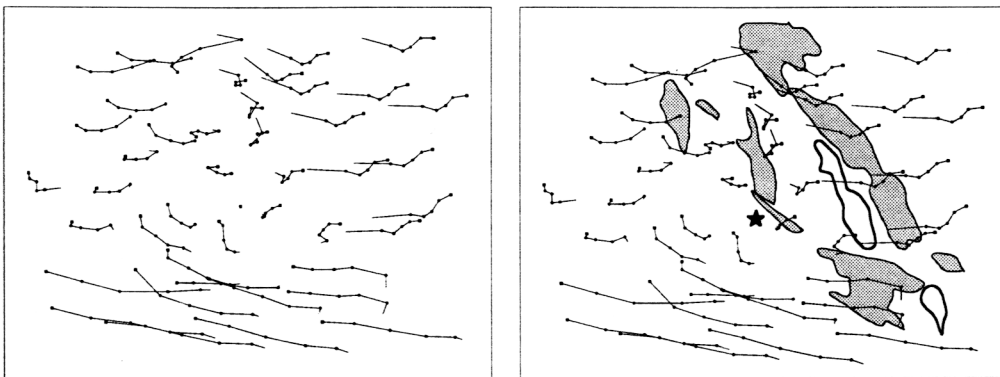
(c)

Figure 4.7   Formation of residual phase aggregates by melt extraction during heating and shortening.   The shaded area shows neighbor switching of four white phase crystals (shown in more detail in Figure 4.8).   (a) t=0 minutes & 26 ˚C.   (b) t=1 hour 58 minutes & 34 ˚C.   (c) t=3 hours 46 minutes & 42 ˚C.   (d) t=6 hours 52 minutes & 55 ˚C.   Plane polarized light. Field width: 0.15 mm.
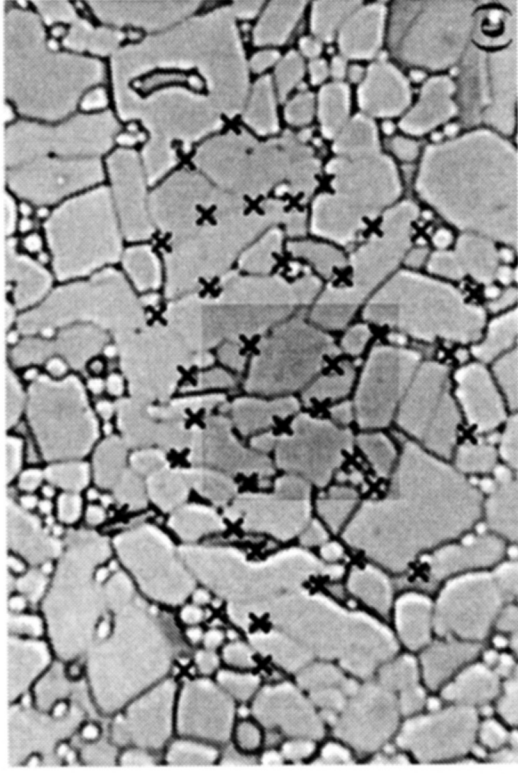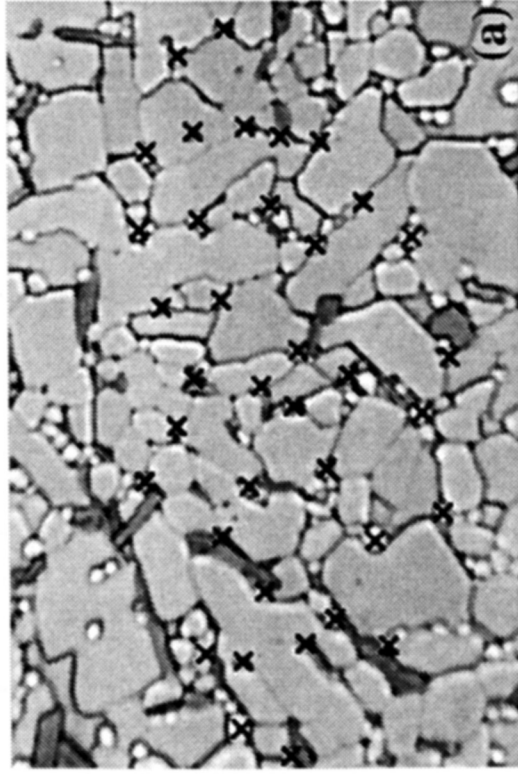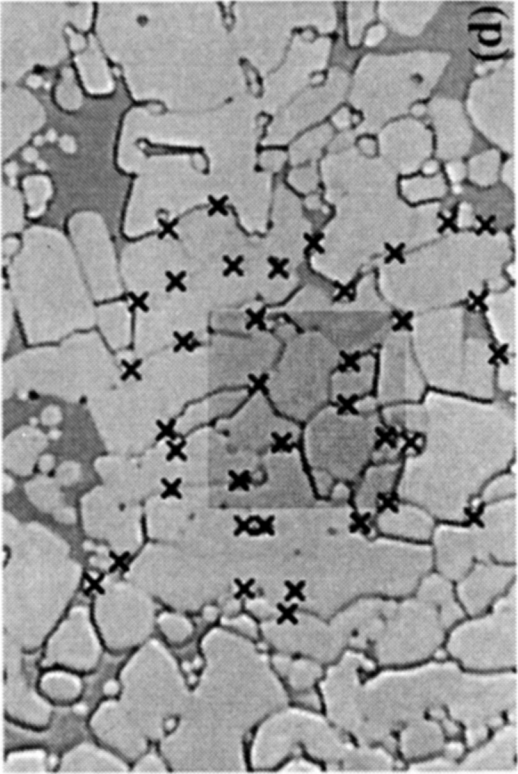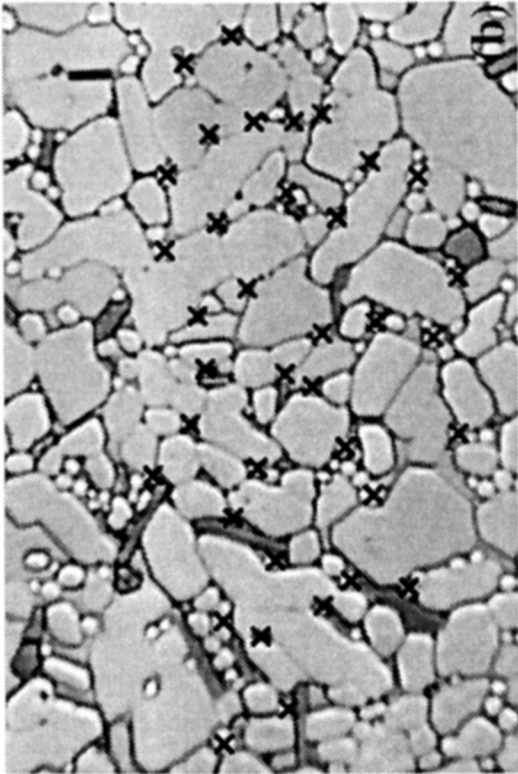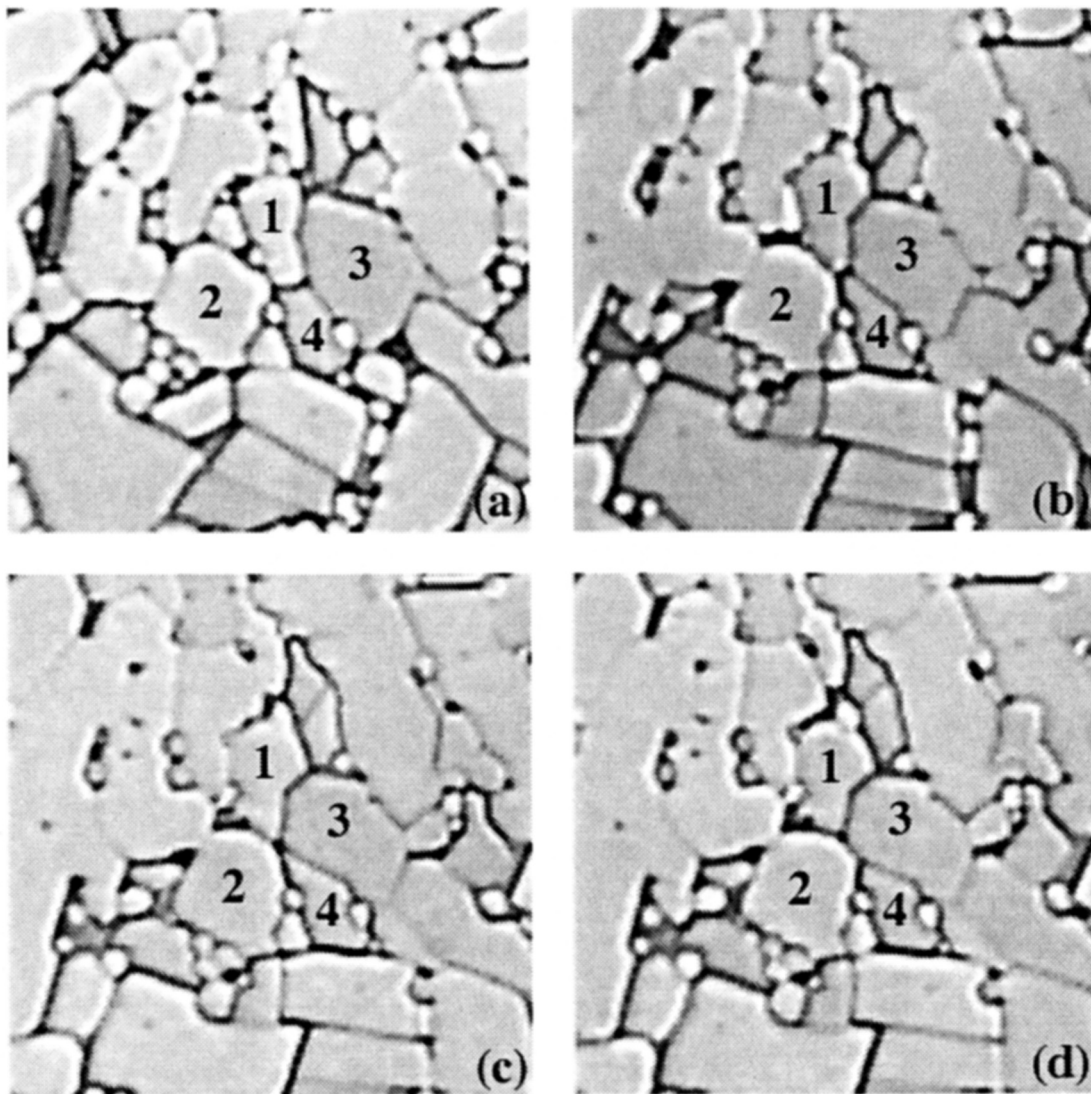
Figure 4.8    Details of neighbor switching in Figure 4.7c to d.  Plane polarized light.
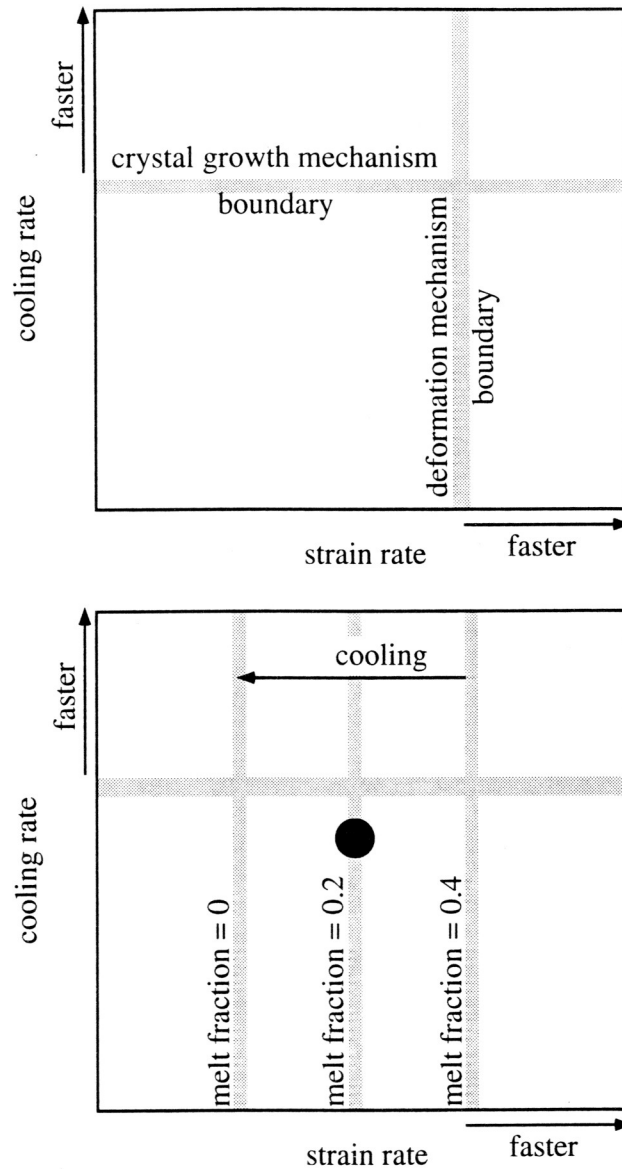
Figure 4.9   Melt fraction dependence of deformation mechanisms. The filled circle in the lower diagram represents constant cooling and strain rate.  As melt fraction decreases, crystal plastic deformation becomes dominant deformation mechanism (shown as moving deformation mechanism boundary).  Mechanisms across the boundaries are same as Figure 4.1.  See text for detail.
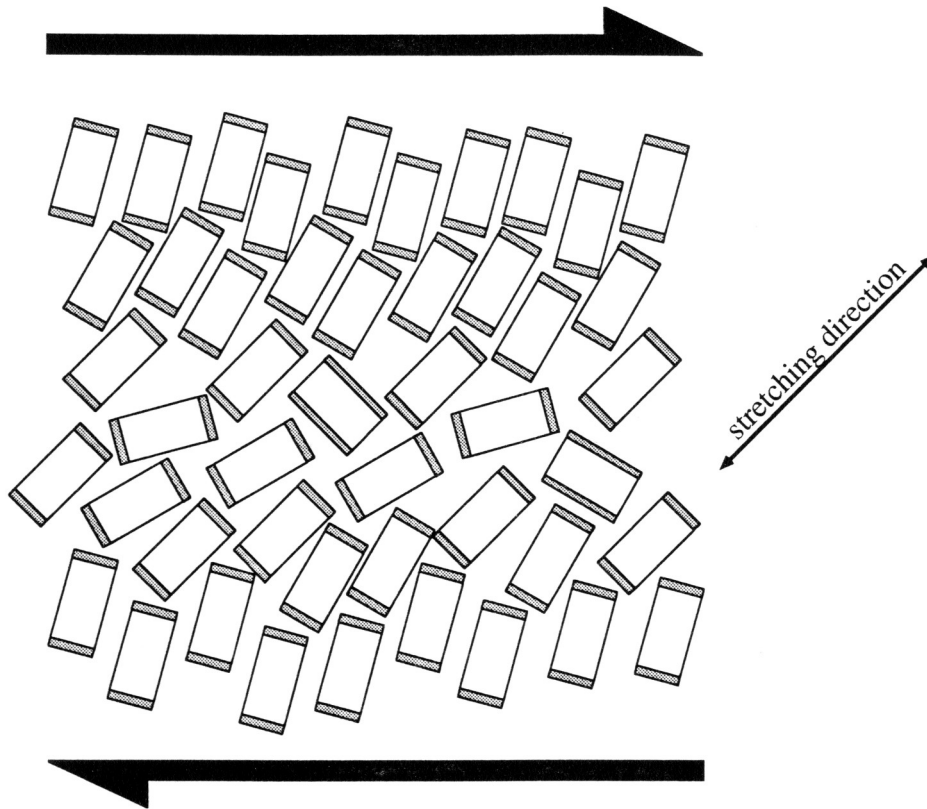
Figure 4.10 A possible microstructure which remembers the stretching direction, when preferential crystal growth toward the stretching direction occurs. The shaded part of crystals are the newly grown part of slightly different chemistry. The mineral zonation in the crystals preferentially faces the stretching direction.

grain size = 2 mm



$\dot{\epsilon} = 10^{-14.7}$ 1/sec

$\dot{\epsilon} = 10^{-10.6}$ 1/sec

stress difference (MPa)

T(°K)

(a)

grain size = 0.1 mm



$\dot{\epsilon} = 10^{-11}$ 1/sec

$\dot{\epsilon} = 10^{-6.9}$ 1/sec

stress difference (MPa)

T(°K)
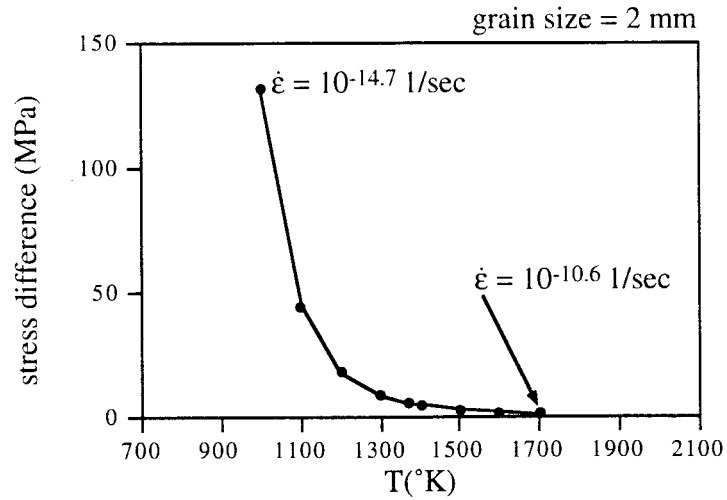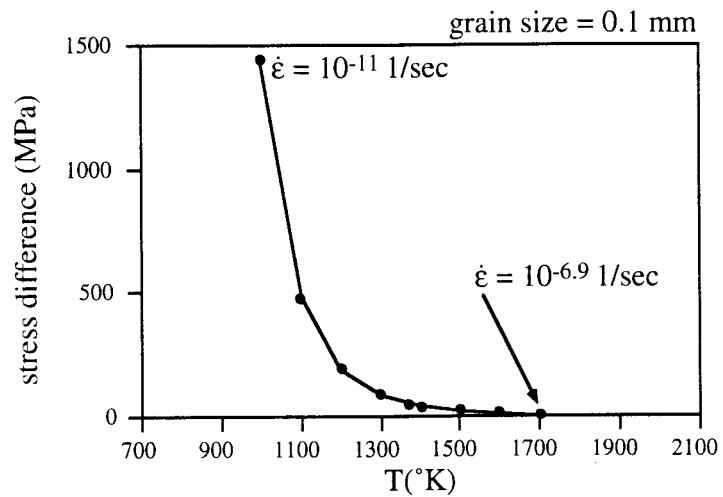
(b)

Figure 5.1   Plots for conditions (stress difference and temperature) in which the ratio of strain rate by dislocation creep to strain rate by diffusion creep is 0.215 in polycrystalline aggregates of olivine.  Flow laws from Karato *et al* (1986).  (a) for grain size 2 mm.  (b) for grain size 0.1 mm.  Strain rate in the figure represents total strain rate.
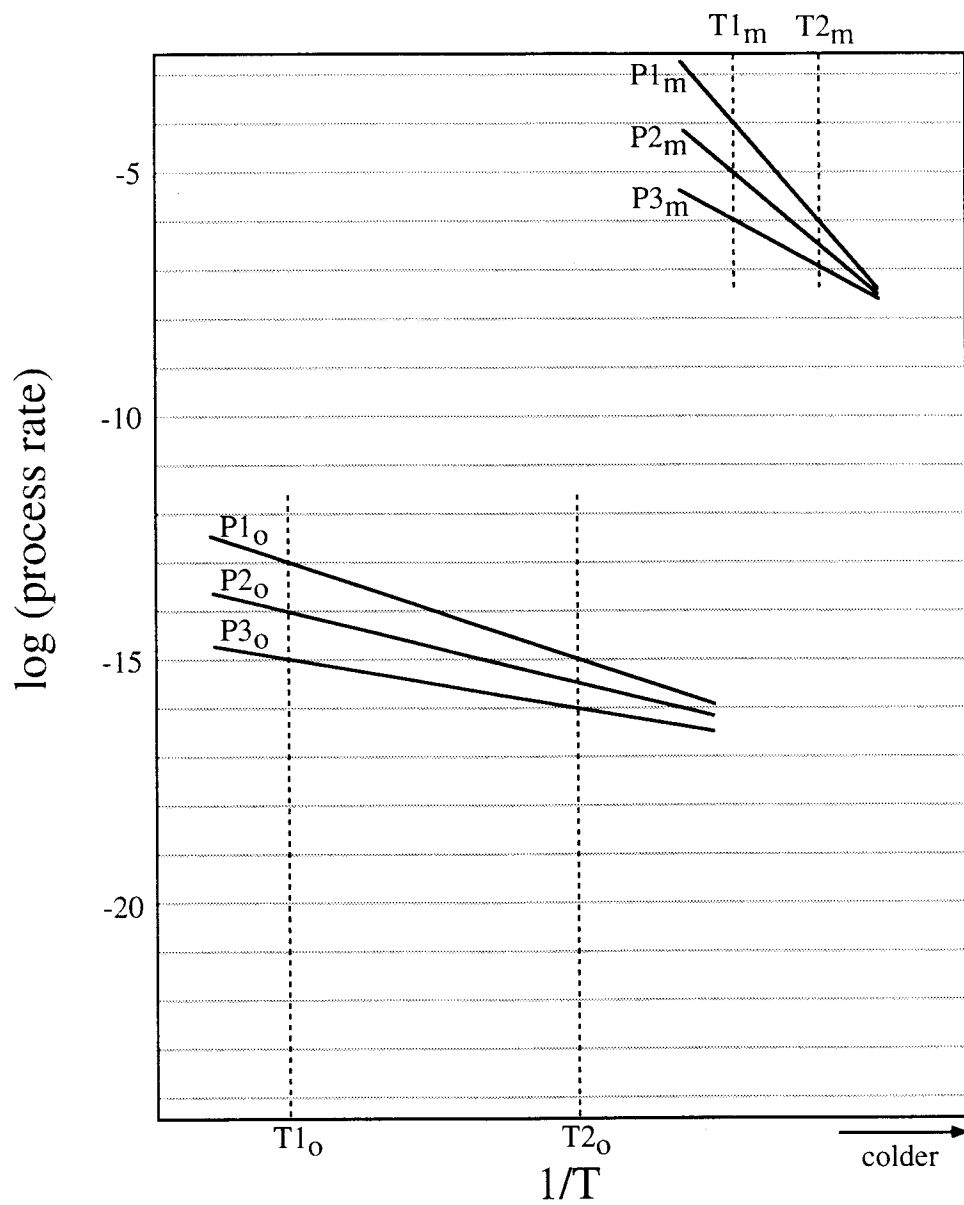
Figure 5.2    Arrhenius plot of process rates (P) in the original (o) and in the model (m).  See text for detail.

Figure 6.1    Crystallization during cooling.  m: melt.  Cooling rate: 5 °C/hour.  (a) t=0 minutes & at 60 °C.  (b) Cotectic crystallization of white phase crystals and cube phase crystals (t=250 minutes & at 40 °C).  (c) Appearance of blue phase crystals (t=370 minutes & at 31 °C).  Plane polarized light.  Field width: 0.6 mm.
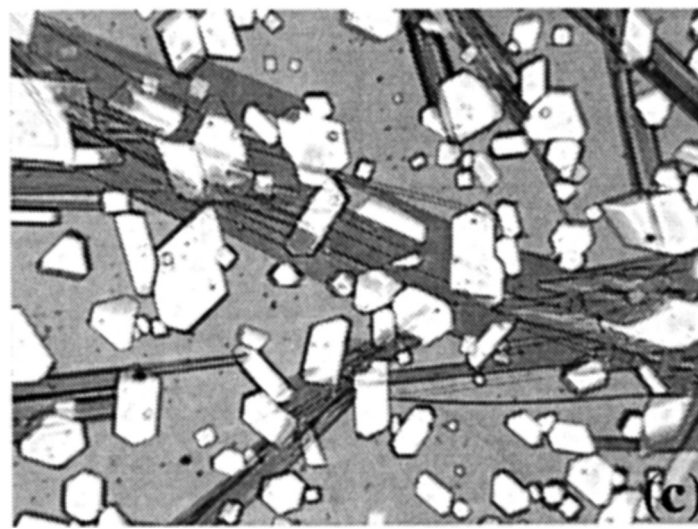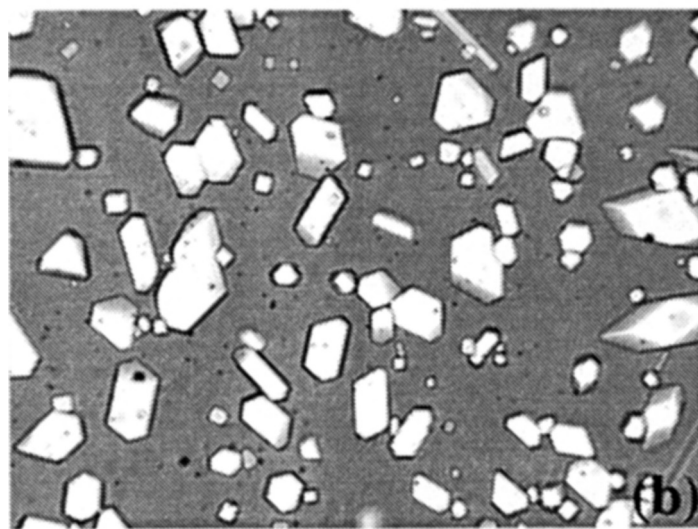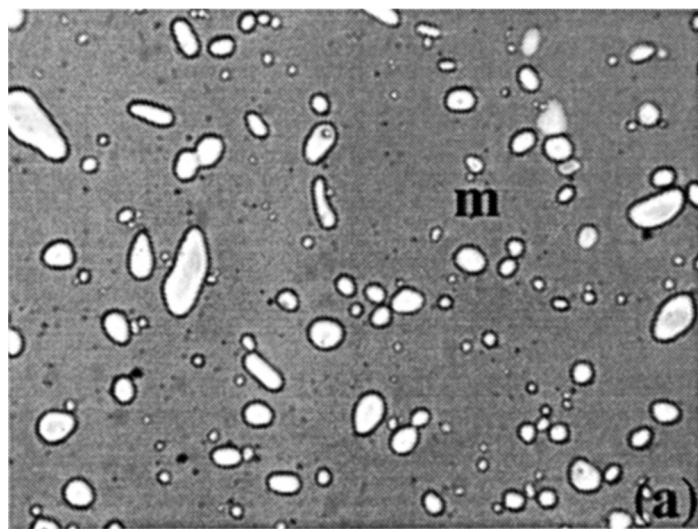
Figure 6.2 Eutectic crystallization at 45 °C. m: melt. B: blue phase crystal. Euhedral crystal faces of white and cube phase crystals become subhedral as growth impingement boundaries form during crystallization of blue phase crystals. (a) t=0 minutes. (b) t=4 minutes. (c) t=5 minutes 10 seconds. (d) t=18 minutes 30 seconds. Plane polarized light. Field width: 0.48 mm.
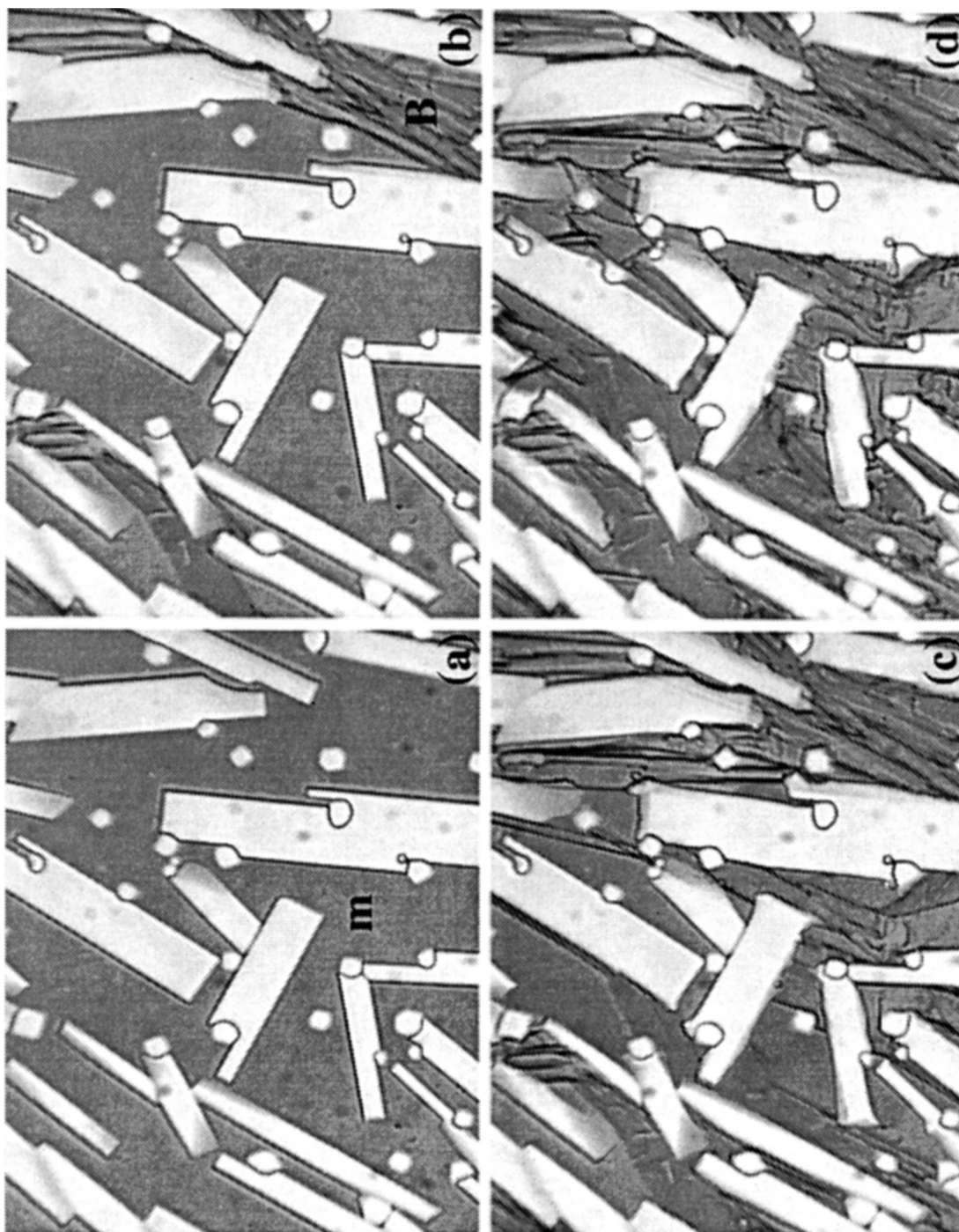
Figure 6.3    Isothermal coarsening of white phase dendritic crystals at 50 °C. m: melt. (a) t=0 minutes. (b) t=20 minutes. (c) t=49 minutes. (d) t=99 minutes. (e) t=149 minutes. (f) t=199 minutes. (g) t=249 minutes. (h) 589 minutes. (i) Plots for time vs. normalized crystal area, and time vs. crystal-melt interfacial surface area. Plane polarized light. Field width: 0.4 mm.
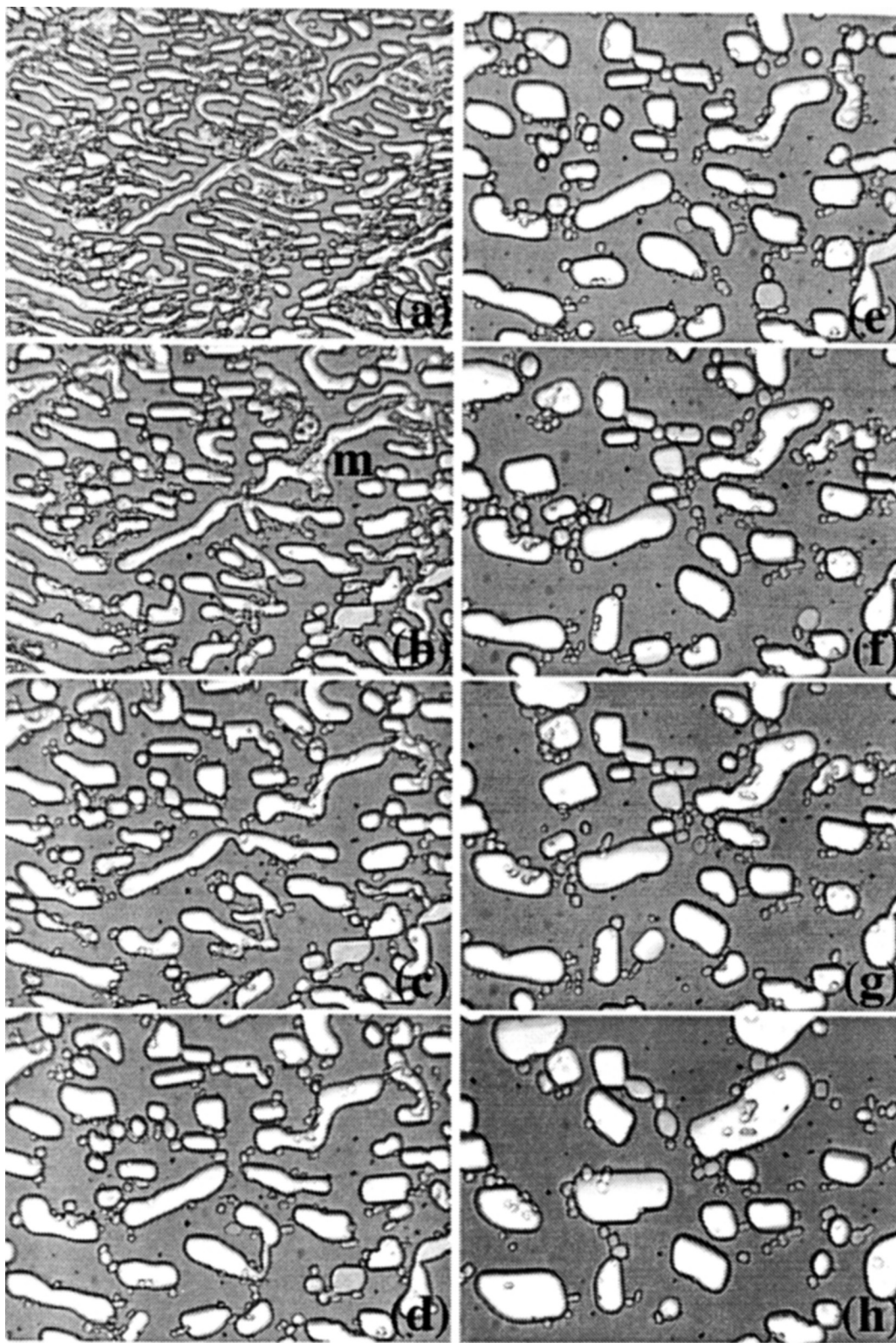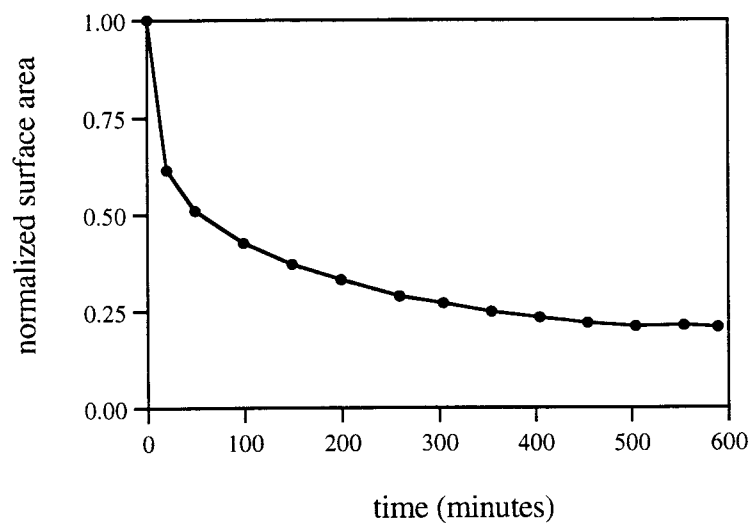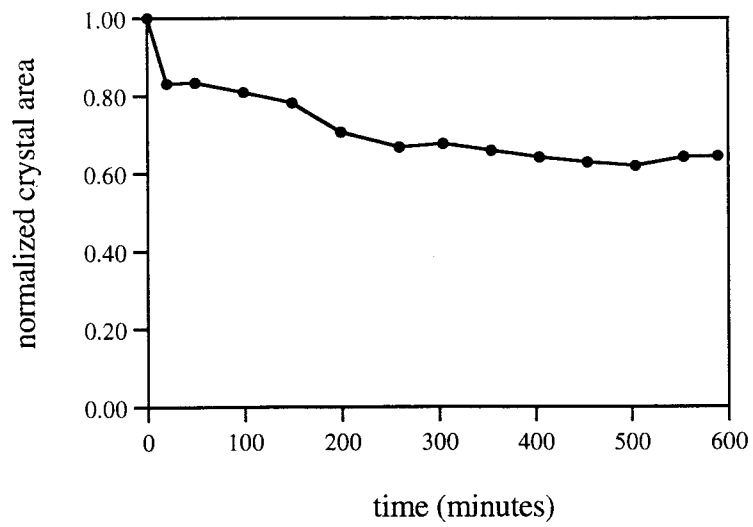
(i)

Figure 6.4 Coarsening during repeated thermal cycling from 55 °C to 75 °C and back at 20 °C/hour cooling and heating rate. m: melt. Some cube phase crystals (indicated by arrows in a) have disappeared during thermal cycling. (a) t=0 hours & at 55 °C. Numbers near the arrows indicate the number of thermal cycling after which the indicated crystals disappeared by complete dissolution. (b) t=1 hour & at 75 °C. (c) t= 2 hours & at 55 °C (after first thermal cycle). (d) t=16 hours & at 55 °C (after 8 thermal cycles). Plane polarized light. Field width: 1 mm.
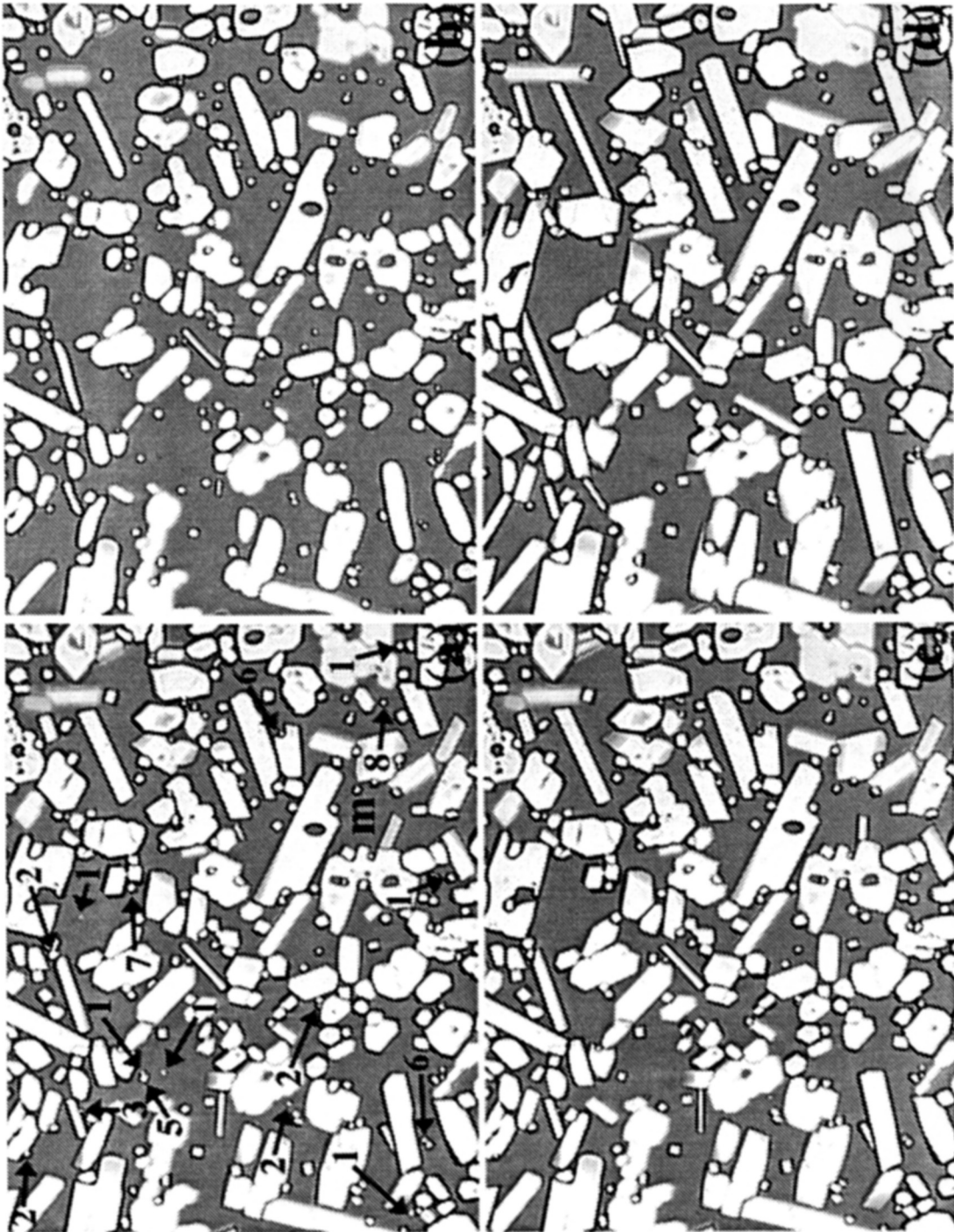
Figure 6.5  A simple model for the disappearing cube phase crystals during thermal cycling in Figure 6.4. (a) Size dependent solubility predicted by the Gibbs-Thompson equation, $C_{(r)} = C \cdot \dfrac{2 \cdot \sigma \cdot V_m}{R \cdot T \cdot r}$ (Shewmon, 1965). $\sigma$: interfacial surface energy (75 erg/cm$^2$ for NaCl-water). $V_m$: molar volume (35 cm$^3$/mole for NH$_4$Cl). R: gas constant ($8.31 \times 10^7$ erg/mole$^\circ$K). T: temperature (338 $^\circ$K, the average temperature during thermal cycling). r: radius of a crystal (cm). Source of $\sigma$ & $V_m$: Handbook of chemistry and physics (73rd ed.). (b) History of crystal size change during thermal cycling. When the solubility of a crystal is independent of size, the crystal size after one cycle of heating and cooling will be same as the initial crystal size (dashed line). However, since the solubility of a crystal is dependent on size, the crystal will 'over-dissolve' as crystal size decreases during heating (solid line). Crystal size of a dissolving crystal after one cycle of heating and cooling will be smaller than the initial crystal size, if diffusion is fast in the melt and all the crystals in the system share the dissolved crystalline constituents during growth.
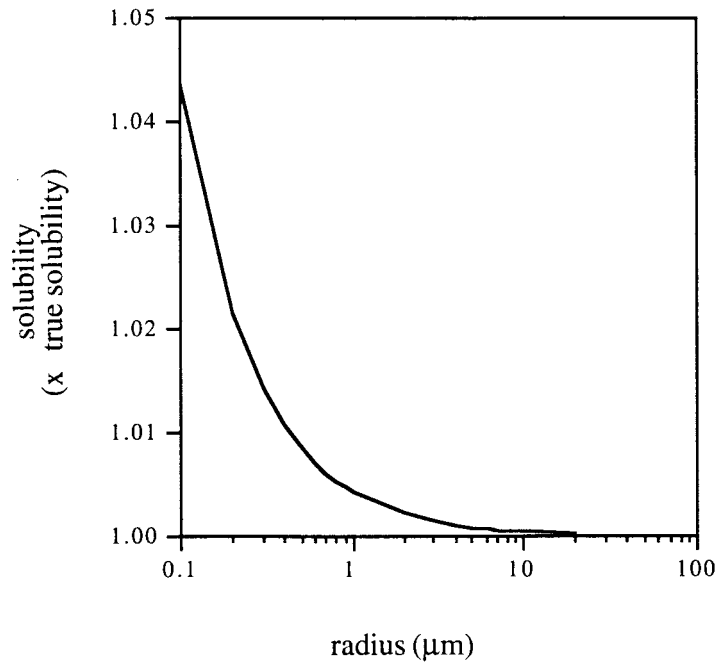
(a)
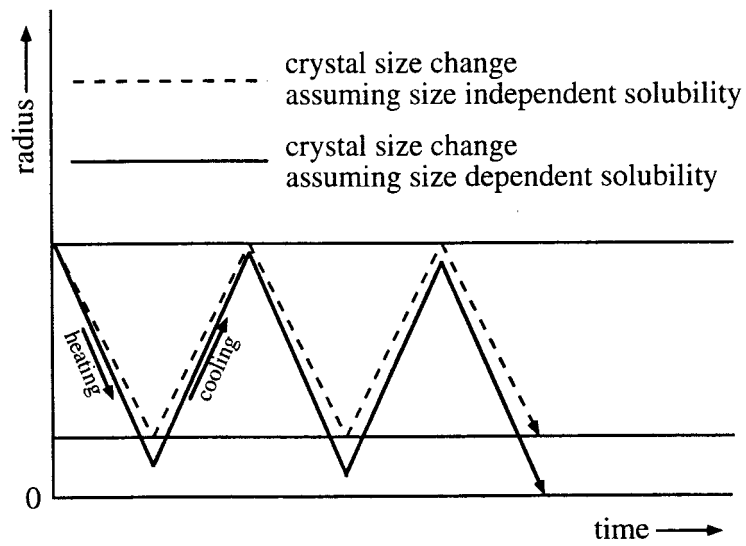


(b)

Figure 6.6   Growth to impingement (a-e) and grain boundary migration (f-h) between white phase crystals 1 & 2 during cooling.  m: melt.  Cooling rate: 6 °C/hour.  (a) t=0 minutes & at 85 °C.  (b) t=25 minutes & at 84 °C.  (c) t=53 minutes & at 83 °C.  (d) t=89 minutes & at 79 °C.  (e) t=124 minutes & at 75 °C.  (f) t=159 minutes & at 71 °C. (g) t=178 minutes & at 67 °C.  (h) t=194 minutes & at 65 °C.  Plane polarized light. Field width: 0.3 mm.
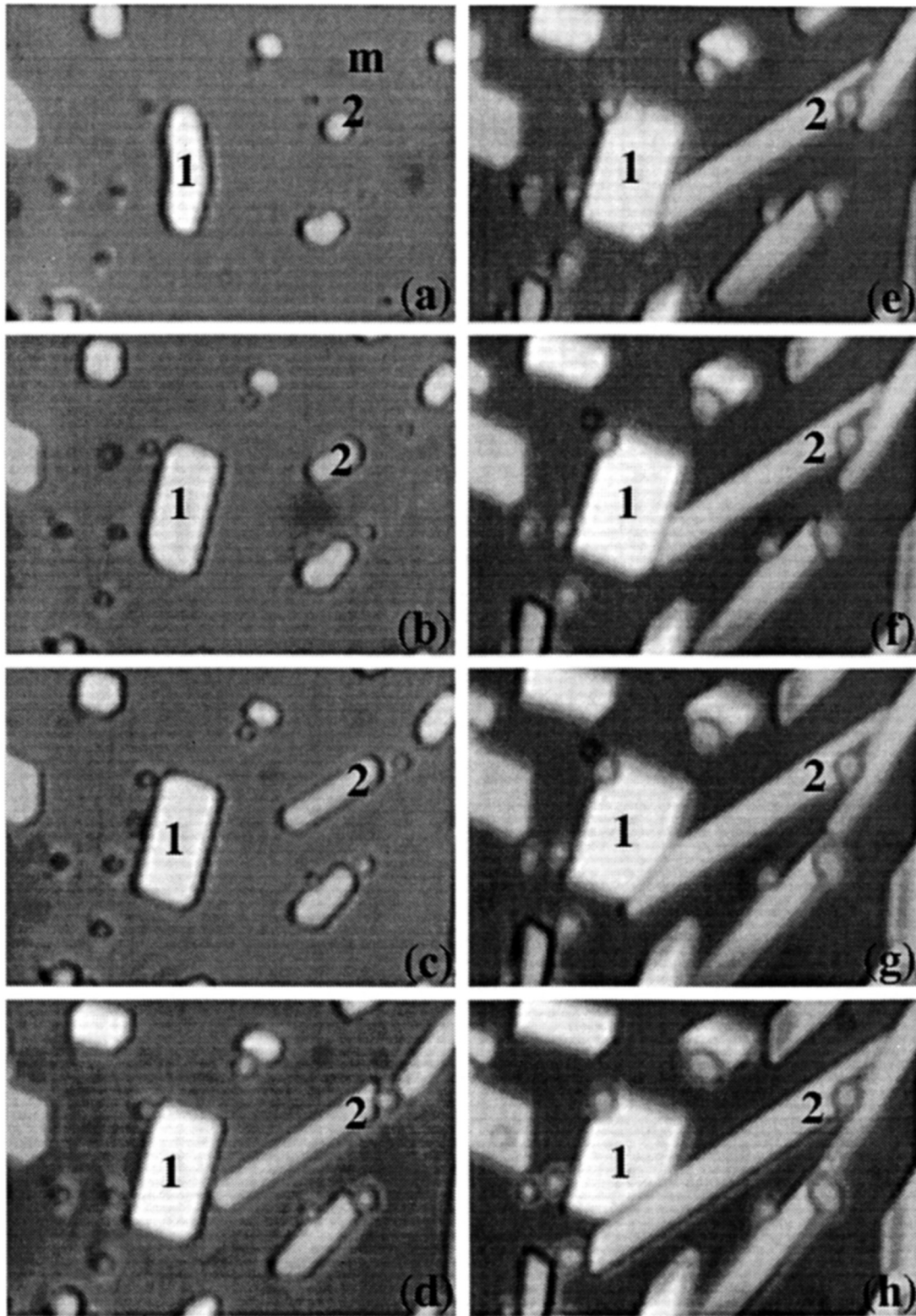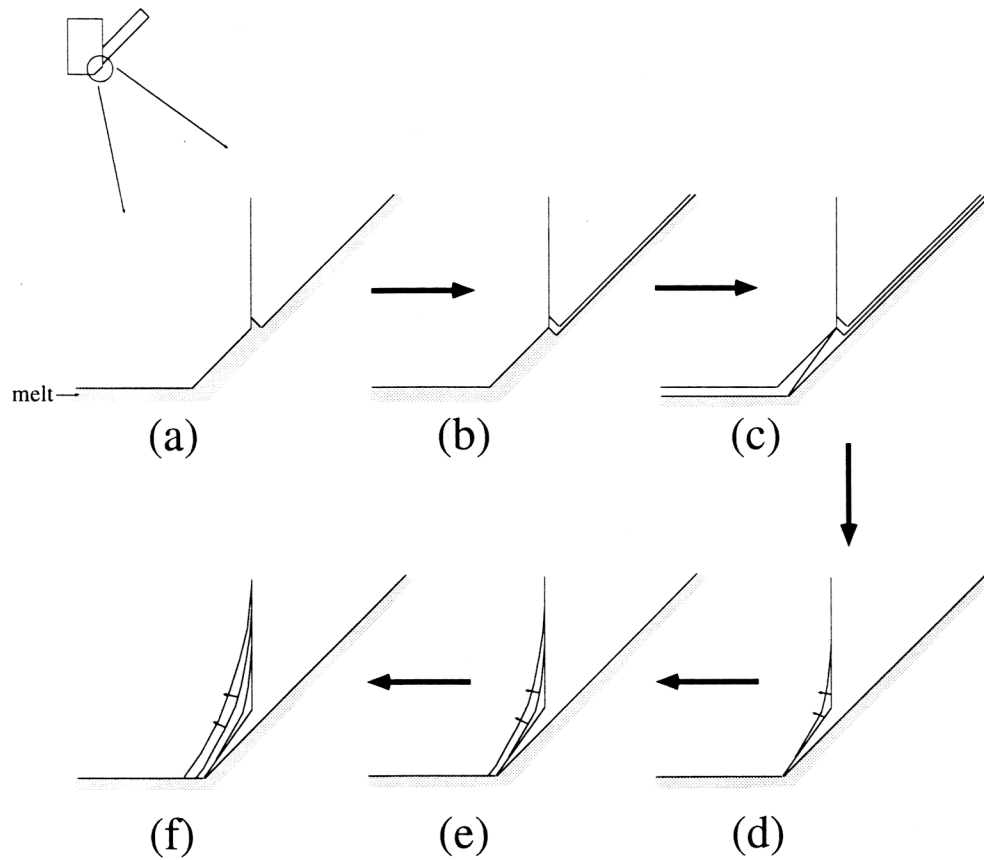
Figure 6.7 A model for the observed grain boundary migration in Figure 6.6. (a) Equivalent to the stage of Figure 6f. (b) to (c) Formation of a new growth impingement boundary. The newly formed growth impingement boundary is not rational with respect to either of the two crystals. (d) to (f) Grain boundary migration starts at the point where the old and new boundaries meet because of higher grain boundary energy due to the curvature.
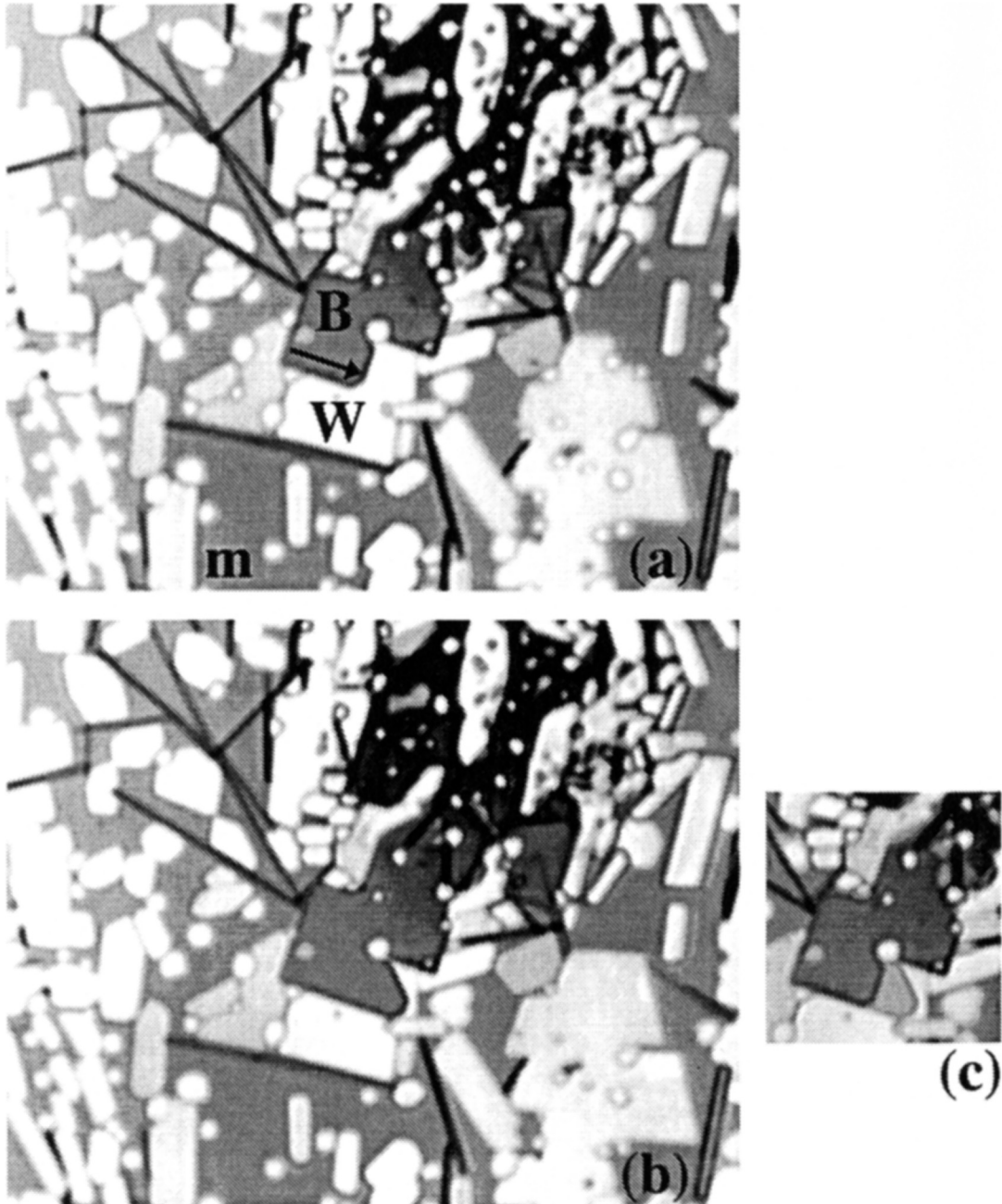
Figure 6.8 Isothermal phase boundary migration at 50 °C. m: melt. The phase boundary between the blue phase crystal (B) and the white phase crystal (W) migrates to the direction indicated by arrow. (a) t=0 days. (b) t=6 days. (c) Superimposed image of (a) and (b). Plane polarized light. Field width: 0.3 mm

Figure 6.9   Isothermal phase boundary migration at room temperature (experiment performed by Professor W.D. Means). m: melt.   The cube phase crystal (C) grows while replacing the white and blue phase crystals.   (a) t=0 days.   (b) t=20 days. (c) t=68 days.   (e) superimposition of (a), (b) & (c).   (a) (b) & (c).   Plane polarized light.   (f) (g) & (h) crossed polarized light equivalent to (a), (b) & (c), respectively.   Field width: 0.45 mm

6-23
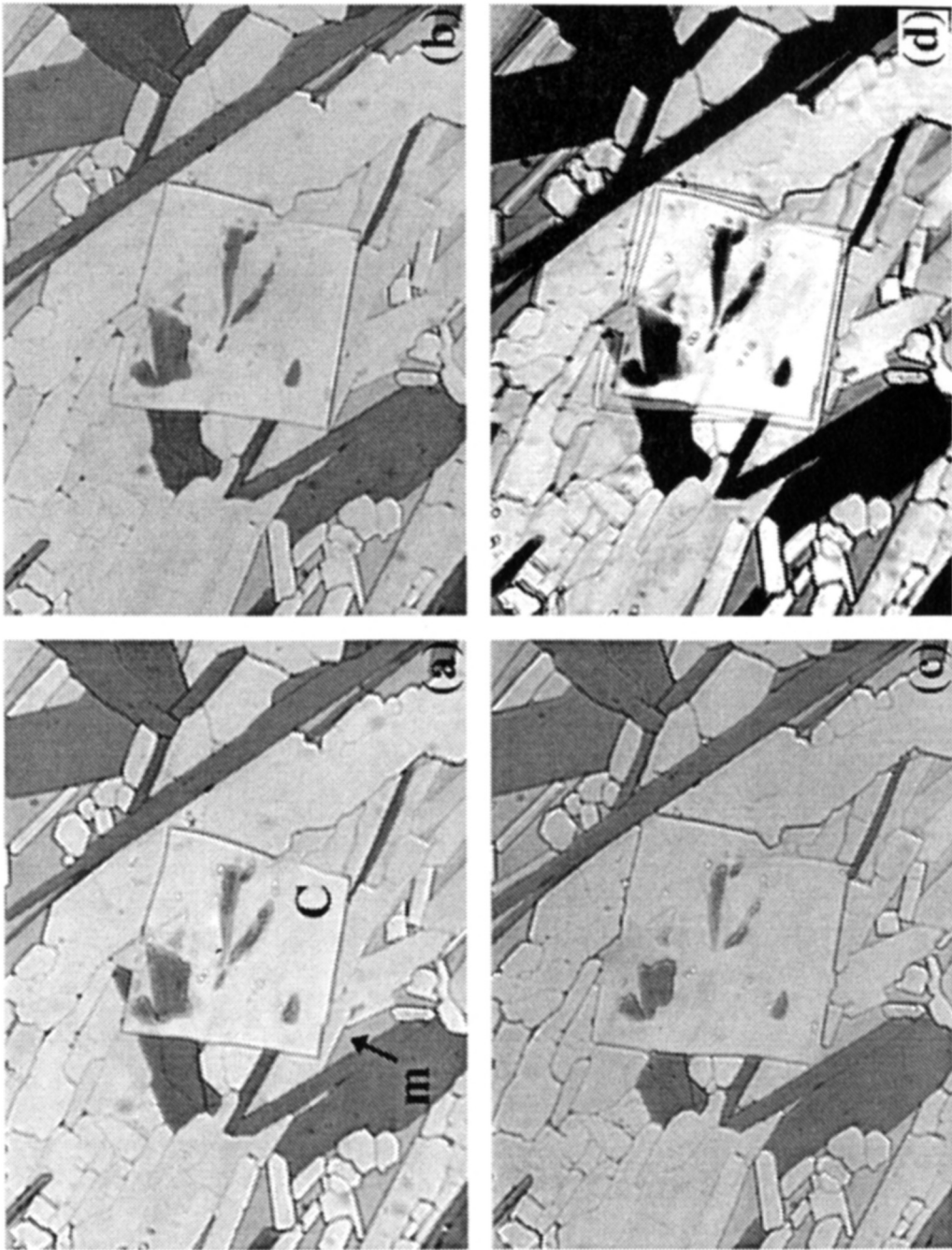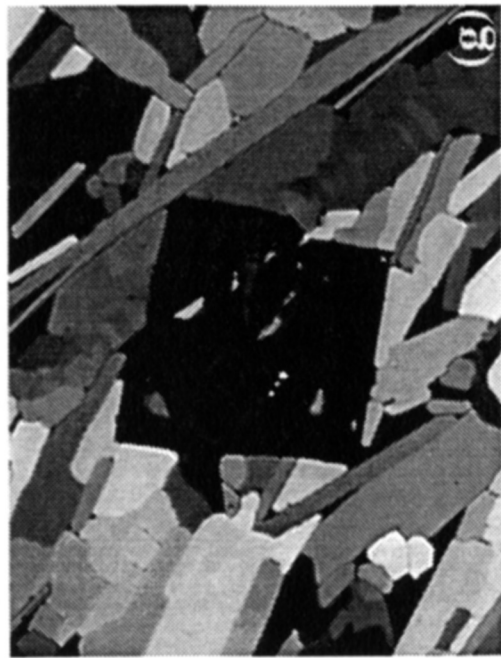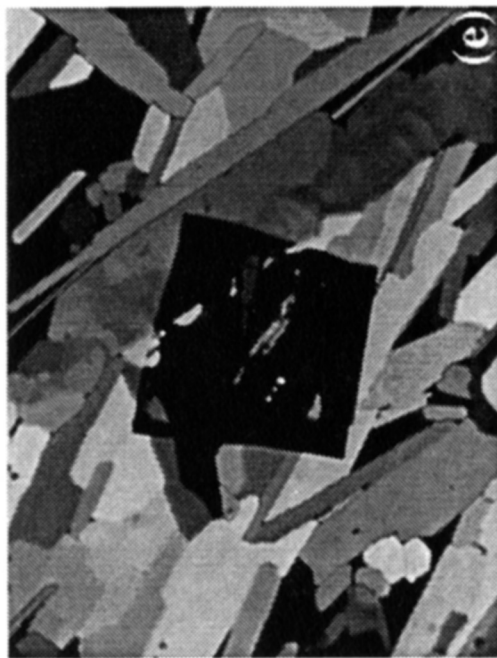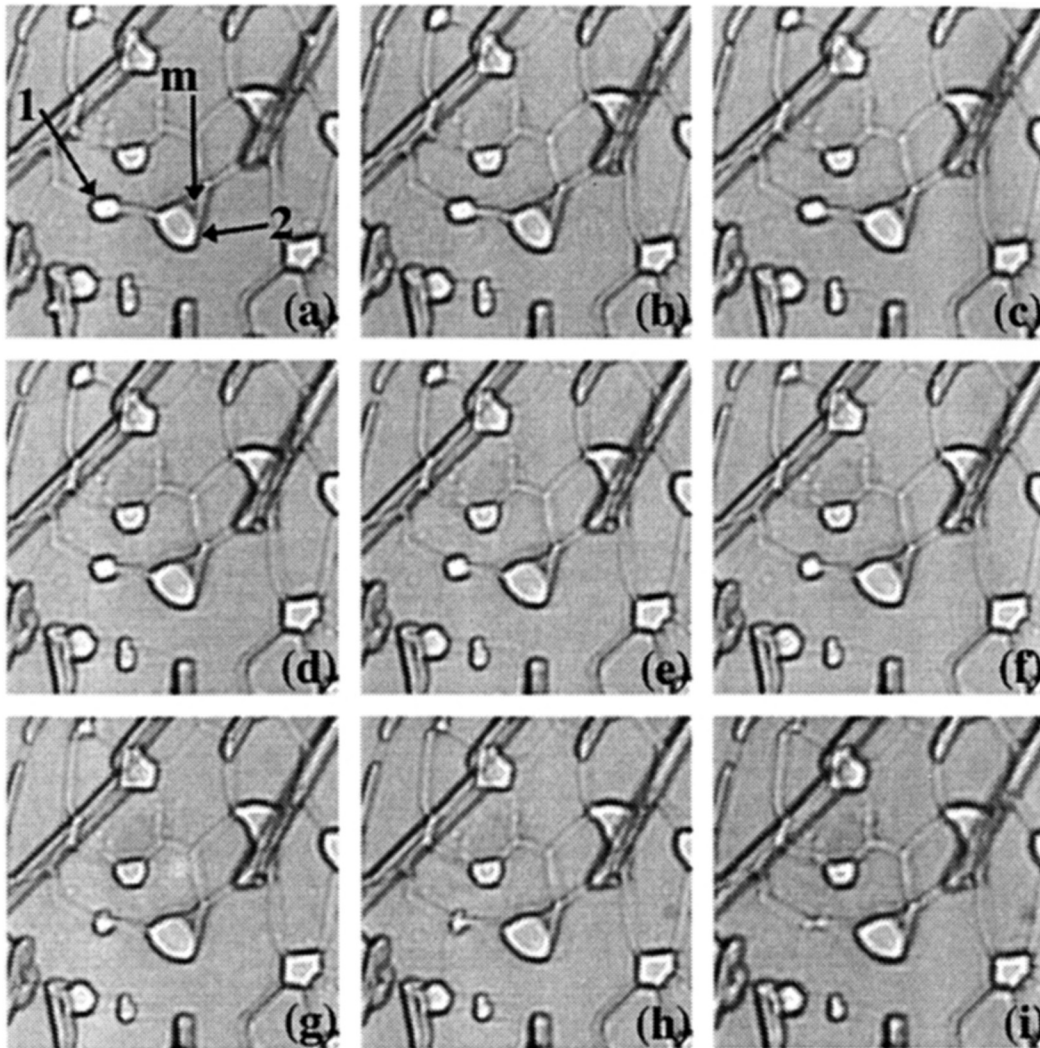
Figure 6.10 Isothermal coarsening of cube phase crystals at 80 °C. m: melt. The cube phase crystal (1) dissolves while the cube phase crystal (2) grows. (a) t=0 hours. (b)t=2 hours. (c)t=4 hours. (d)t=6 hours. (e)t=8 hours. (f)t=10 hours. (g)t=12 hours. (h)t=14 hours. (i)t=16 hours. Plane polarized light. Field width: 0.25 mm.
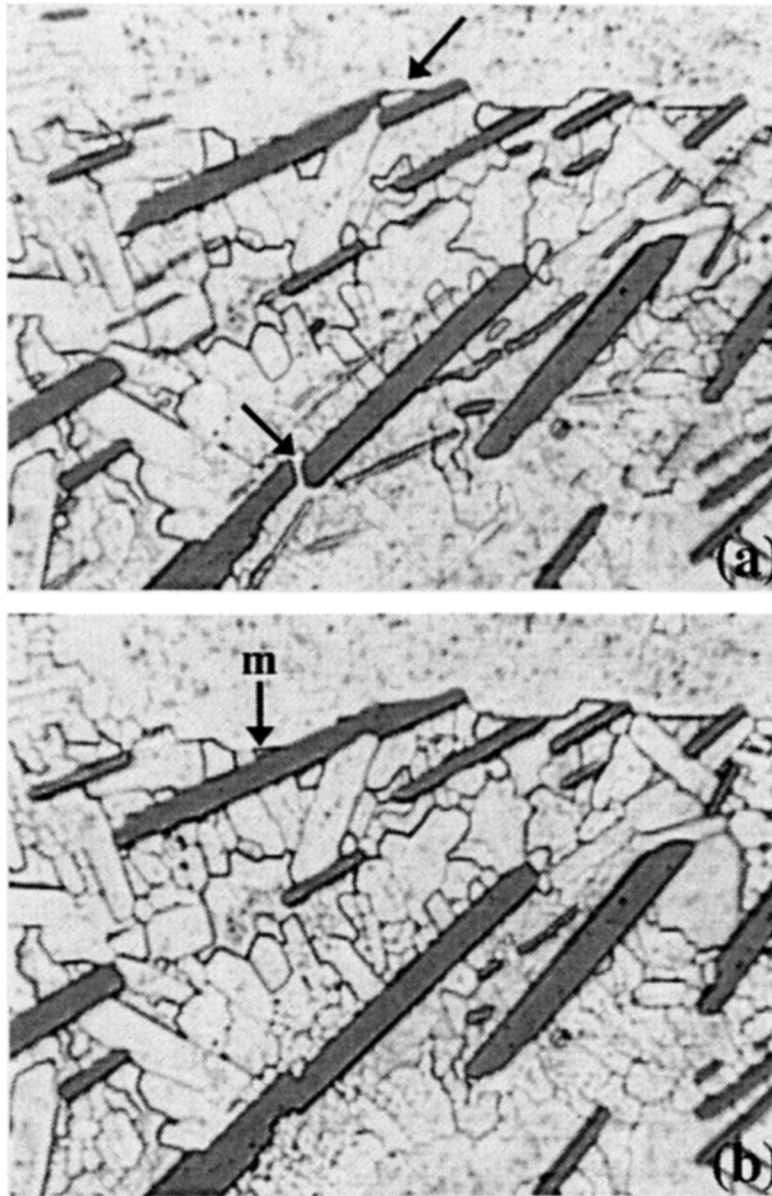
Figure 6.11 Isothermal coarsening of blue phase crystals at 80 °C. m: melt. The scattered smaller and thinner blue phase crystals dissolve while the larger blue phase crystal grows. Two blue phase crystals, initially separated by a white phase crystal (indicated by arrows), become connected by growth. (a) t=0 hours. (b)t=3 days 23 hours. Melt fraction in this sample is very low (~ < 1%). Plane polarized light. Field width: 0.25 mm.
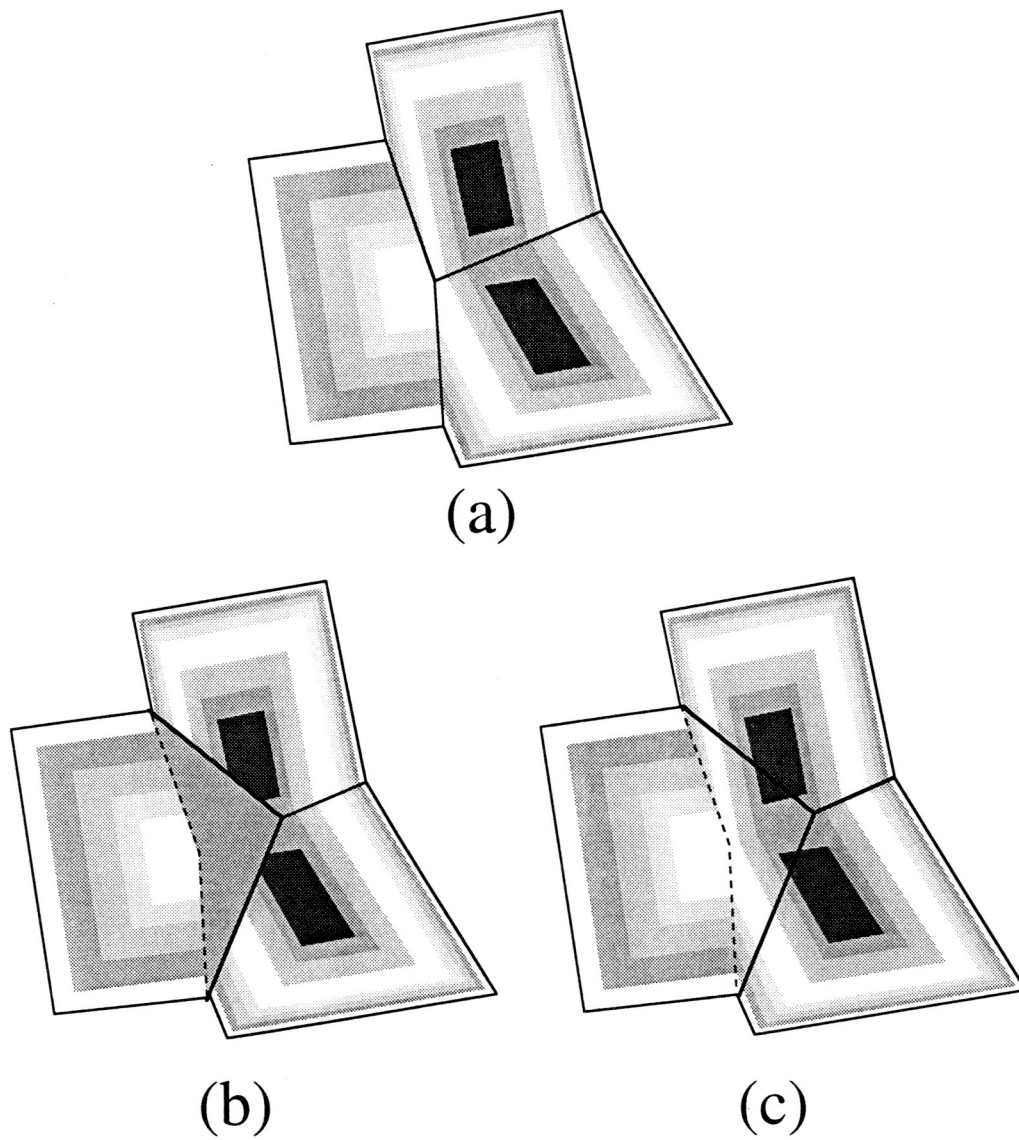
Figure 6.12 Possible zonation patterns in crystals after phase boundary migration. (a) Normal growth impingement boundaries between three crystals. The triple junction migrates to the right in order to achieve textural equilibrium. (b) & (c) Possible zonation pattern after phase boundary migration, depending on the range of diffusion. See text for detail.
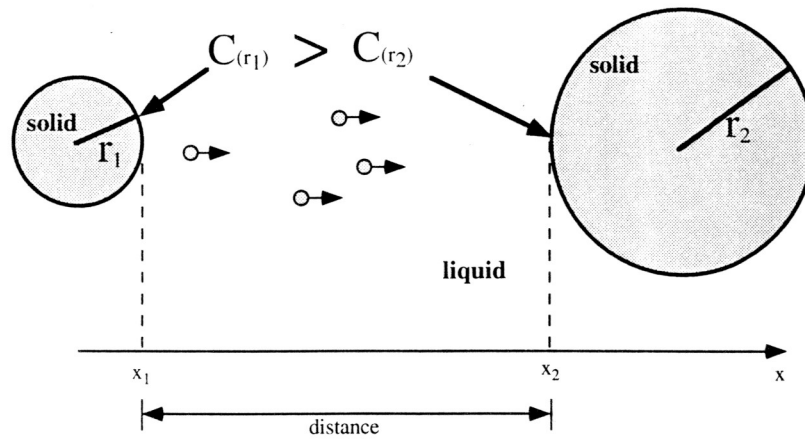
Figure 7.1   Schematic diagram illustrating the particle size dependent solubility (or concentration at interface) and resulting diffusive mass transfer from higher concentration at the smaller particle interface to lower concentration at the larger particle interface.
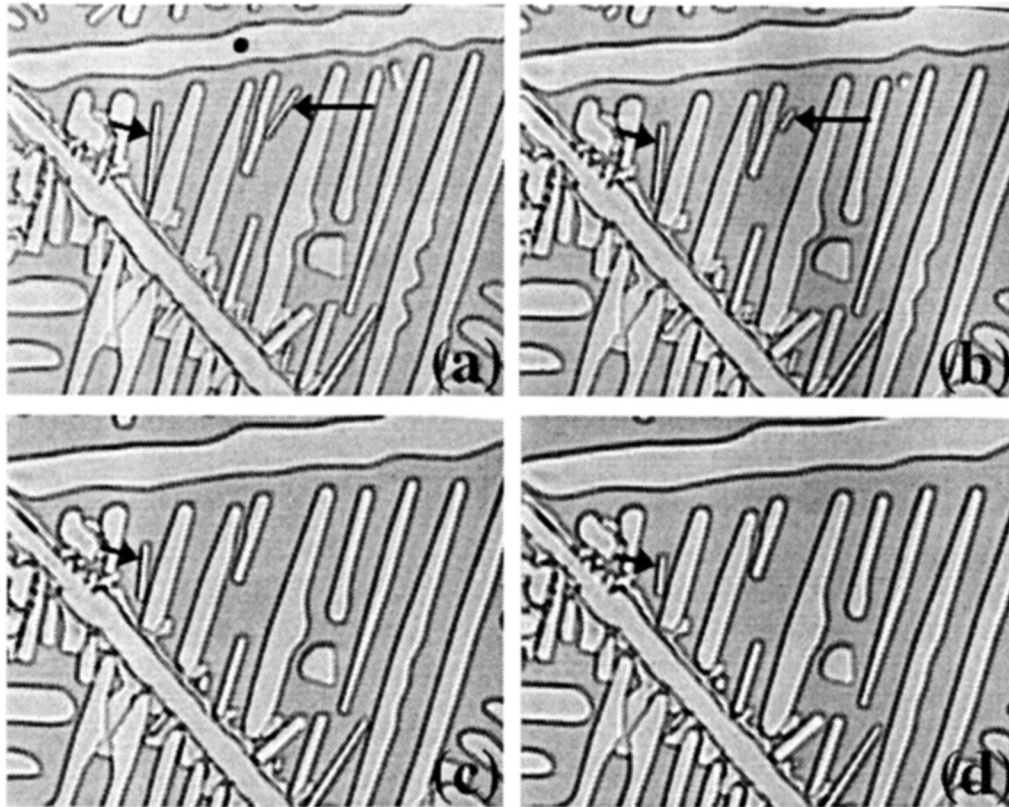
Figure 7.2    Isothermal (25 °C) coarsening of dendrite arms of ammonium thiocyanate crystals in a hydrous solution.  (a) t=0.  (b) t=12 minutes.  (c) t=24 minutes.  (d) t=36 minutes.  Narrow arms of a dendritic crystal (indicated by arrows) dissolve because of the high curvature at the tips.  Larger arms simultaneously increase in area (e.g. at circle).  Field width: 200 μm.
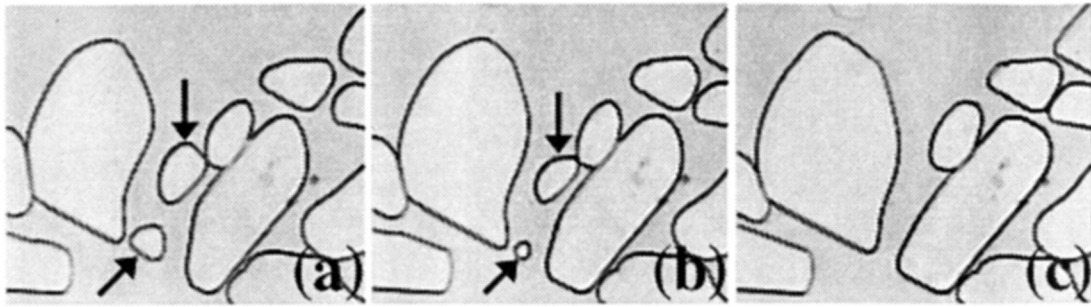
Figure 7.3   Dissolution of ammonium thiocyanate crystals (indicated by arrows) during cooling due to coarsening process (cooling rate: 5 °C/hour).  (a) t=0 & 70 °C. (b) t=40 minutes & 67 °C.  (c) t=100 minutes & 62 °C.  Field width: 250 μm.
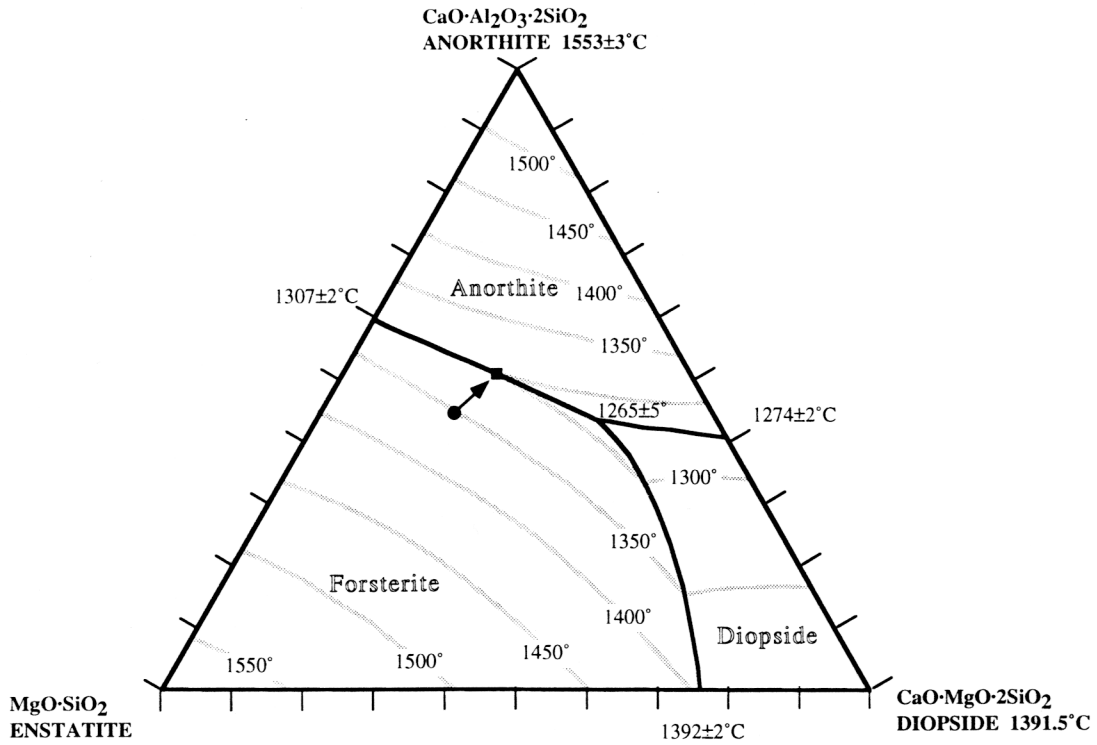
Figure 7.4   Phase diagram of the experimental system (from Morey, 1964).  Filled circle represents the starting bulk composition and filled square represents the projected melt composition at 1275° C.
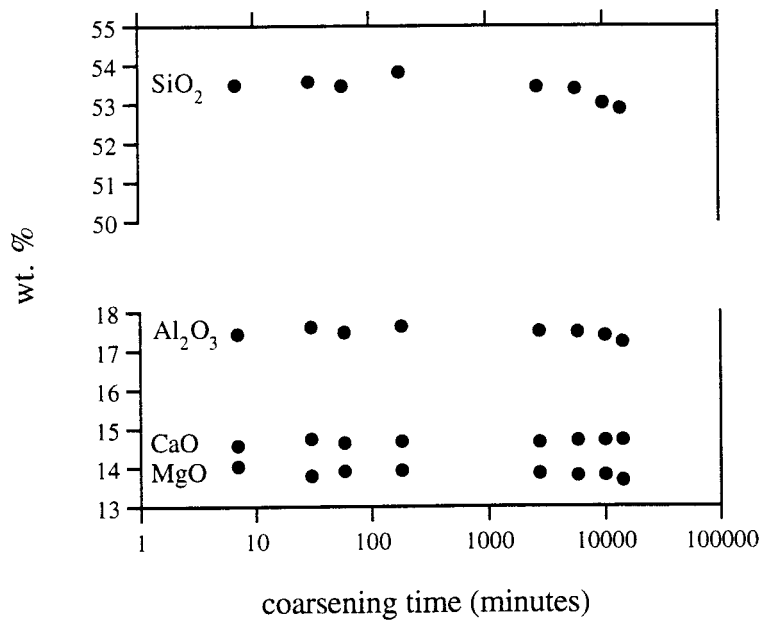
Figure 7.5   Plot of coarsening time vs. melt composition. The melt compositions from different coarsening experiments are virtually identical, suggesting the same conditions for each run.  Each result is the average of 5 analyses of glass at different places in the same experimental charge (Error bars smaller than symbols).

Figure 7.6    Backscattered electron images from the forsterite coarsening experiment. Black phase is forsterite and gray phase is glass (field width: 200 μm). (a) after 7 minutes of coarsening, (b) after 30 minutes, (c) after 58 minutes, (d) after 180 minutes, (e) after 1.9 days, (f) after 4.0 days, (g) after 6.9 days, & (h) after 9.8 days. Black lines are cracks in the experimental charge.
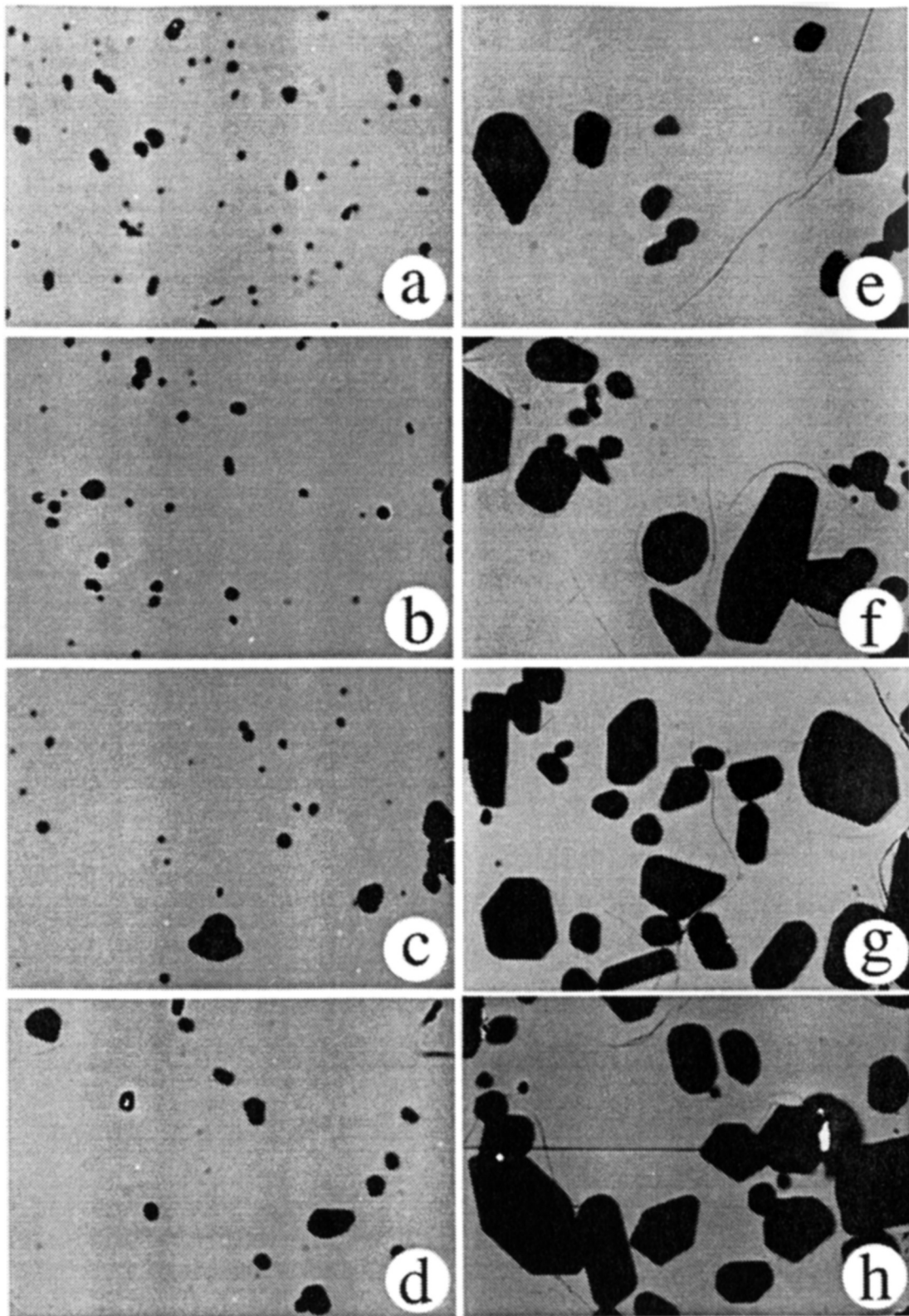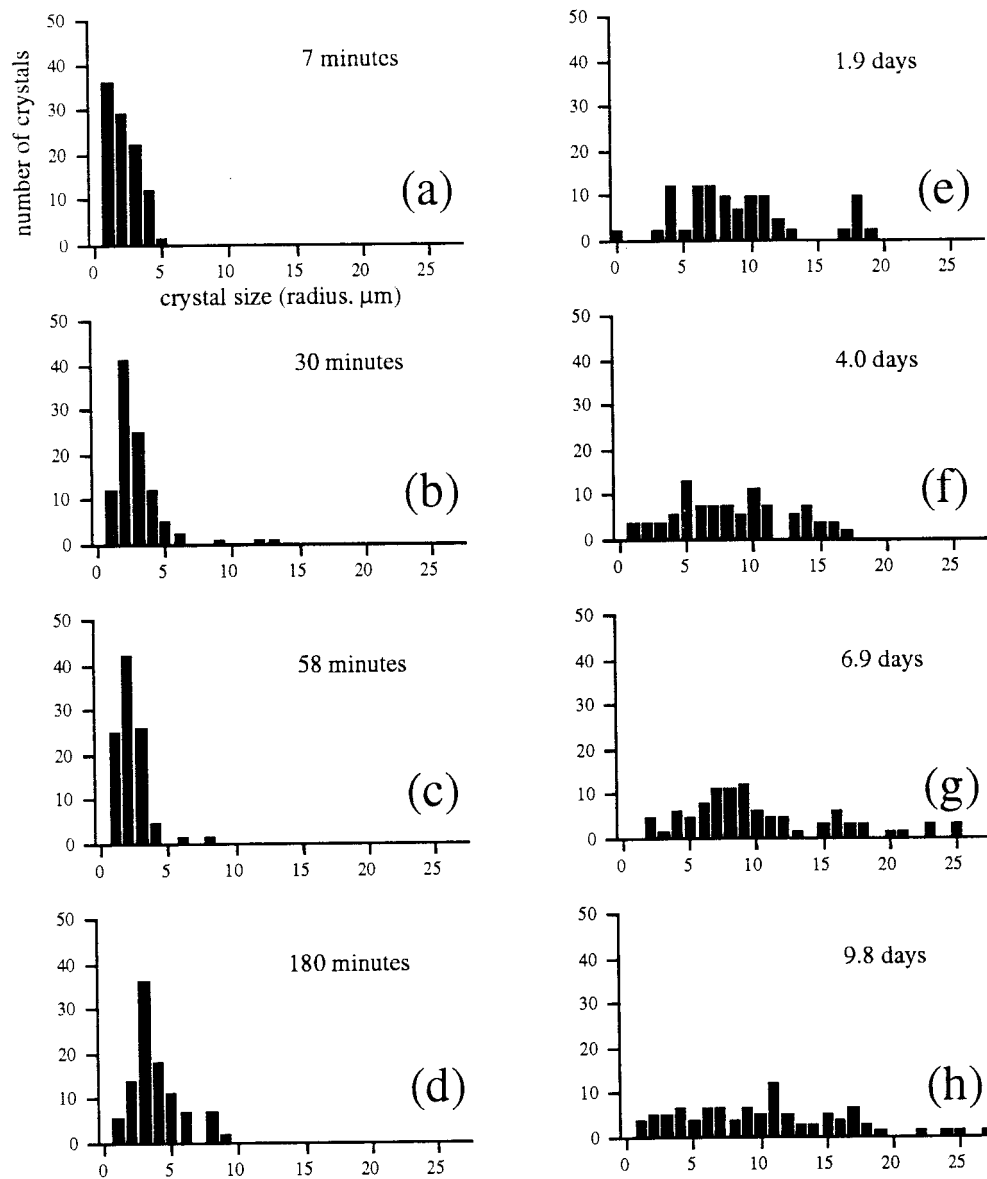
Figure 7.7  Forsterite crystal size distribution (size vs. frequency) from the coarsening experiment. Total number of crystals in each diagram are normalized to 100 crystals so that the integrated area in each diagram is same. Labels in this figure correspond to labels in Figure 7.6. Numbers of actually measured crystals are (a) n=83, (b) n=122, (c) n=85, (d) n=56, (e) n=42, (f) n=53, (g) n=65, (h) n=77.
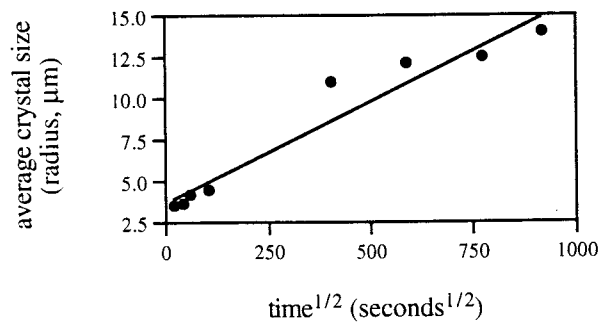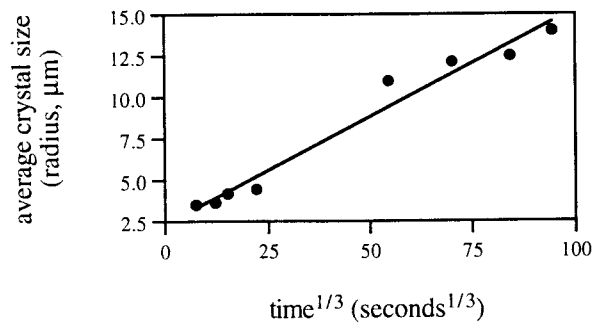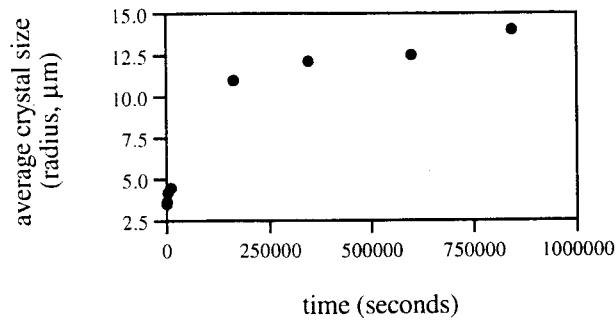
Figure 7.8   Plots of crystal size vs. time (a), time$^{1/3}$ (b), and time$^{1/2}$ (c). Stereologically corrected average radius for crystals was used in this plot. (b) slope of regression line=0.012 and correlation coefficient ($r^2$)=0.938. (c) slope of regression line=0.129 and correlation coefficient ($r^2$)=0.969.
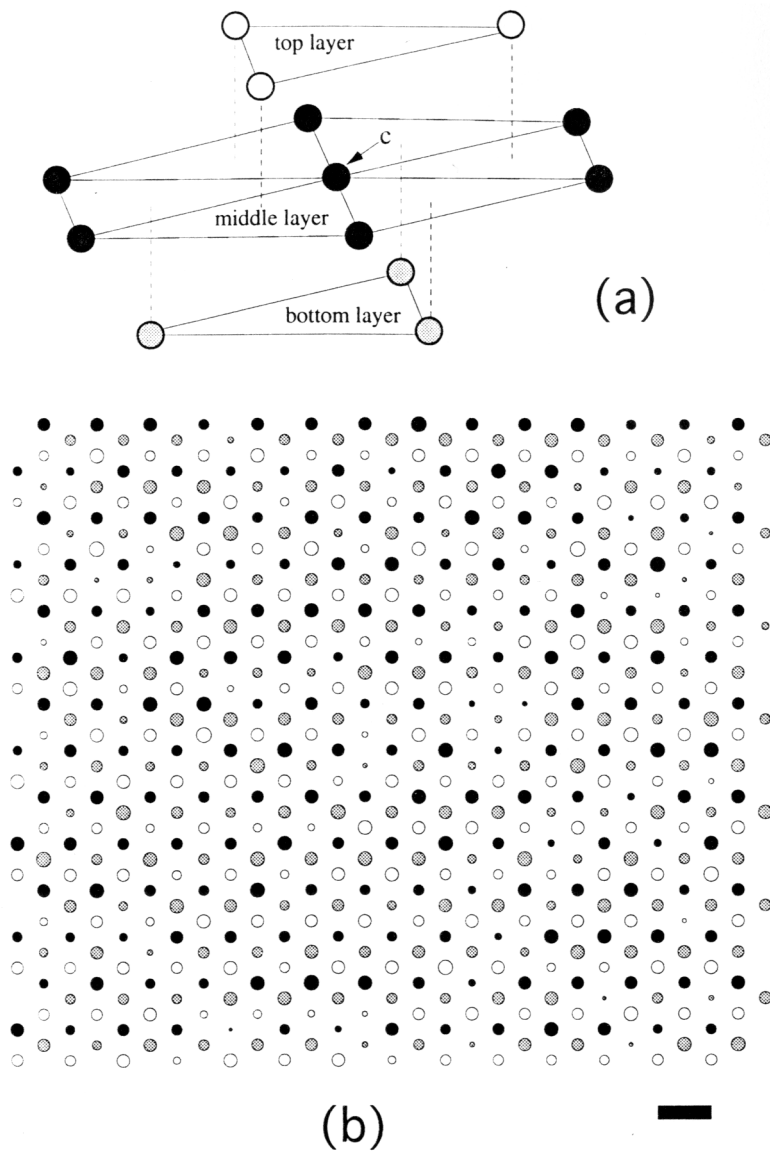
Figure 7.9   Geometry of crystal distribution assumed in the computer simulation of coarsening. (a) One crystal at center ('c') is surrounded by 12 neighboring crystals of equal distance (similar to hexagonal closed packing). (b) Map view of initial crystal distribution. Crystal size distribution in (b) is the size distribution that has reached steady state. Same patterns as (a) is used to represent crystals in different layers. Scale bar at the bottom right represents center to center distance between neighboring crystals.
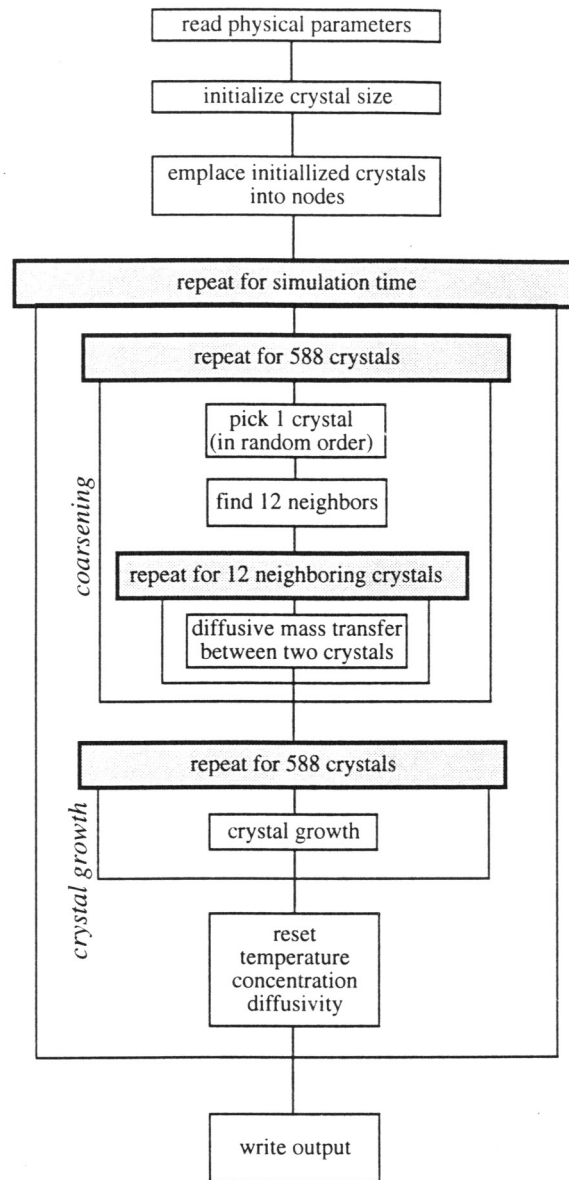
Figure 7.10 Flow chart for the algorithm of the coarsening simulation program.

Figure 7.11 Results of coarsening simulation (conditions summarized in Table 7.1). (a) Output from the program. Initially small crystals (indicated by arrows) surrounded by larger crystals dissolve completely and initially larger crystals (indicated by boxes) are growing at the expense of small neighboring crystals. (b) Time vs. total crystal volume plot, showing constant volume is maintained during isothermal coarsening. (c) time$^{1/3}$ vs. average radius plot (slope of regression line=0.024 and correlation coefficient ($r^2$)=0.969). (d) Steady state crystal size distribution during diffusion limited coarsening. Dashed line represents the initial size distribution and solid line represents the size distribution after isothermal coarsening of 2 days. The normalized crystal size is the crystal size normalized to the average crystal size, and the normalized frequency is the frequency normalized to the frequency of average crystal size.
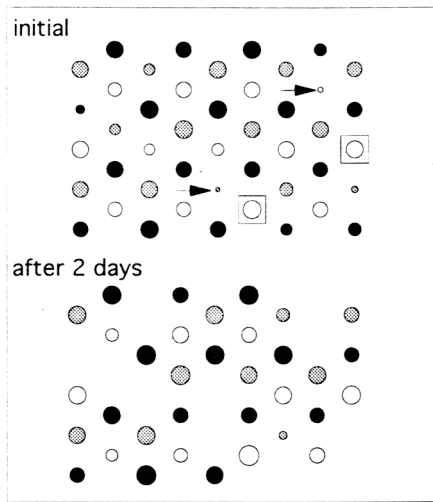
(a)
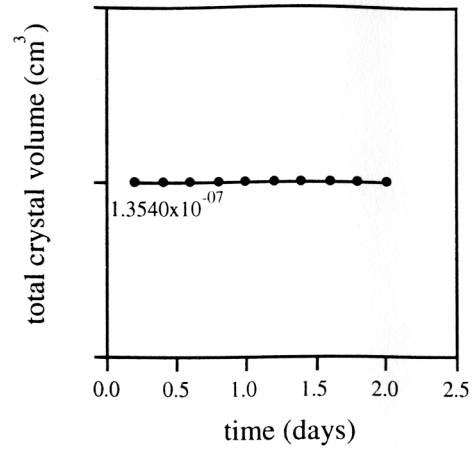
(b)
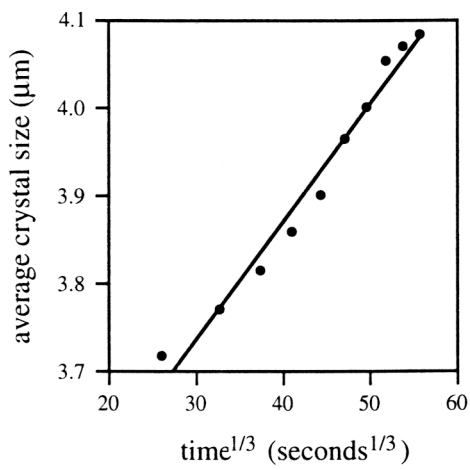
(c)
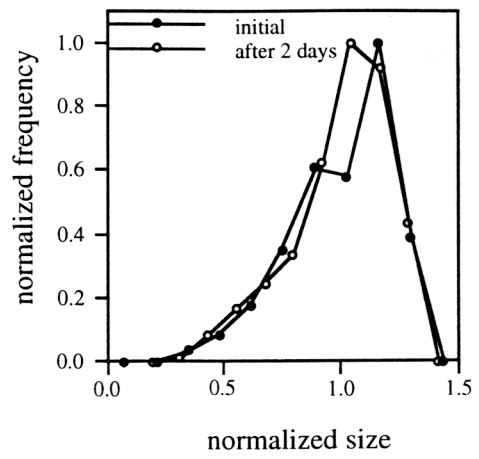
(d)
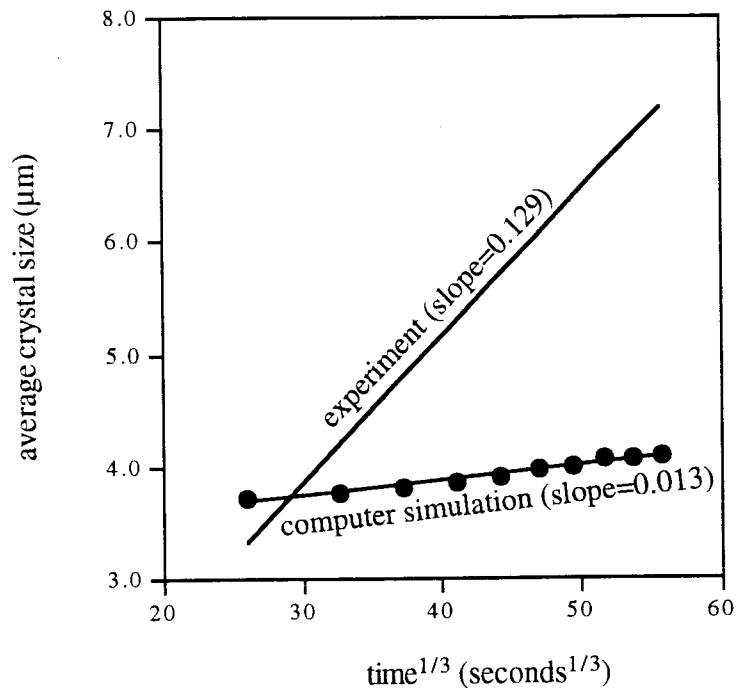
Figure 7.12 Comparison of the rate of average radius increase from experiments and computer simulation.
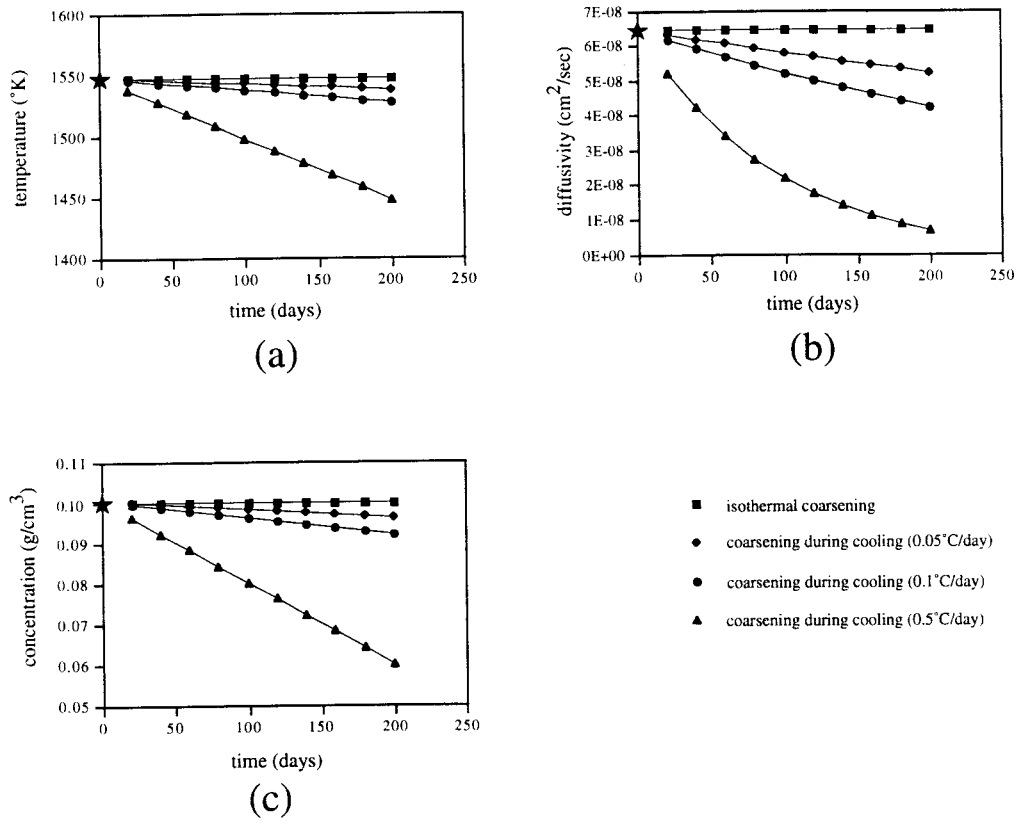
Figure 7.13 Simulation conditions for coarsening during cooling of various rates. Stars indicate the initial conditions. Changes of diffusivity and concentration follows the assumptions made in Table 7.2.

initial condition

isothermal coarsening (after 100 days)

coarsening during cooling, -0.05 °C per day (after 100 days)

coarsening during cooling, -0.1 °C per day (after 100 days)

coarsening during cooling, -0.5 °C per day (after 100 days)
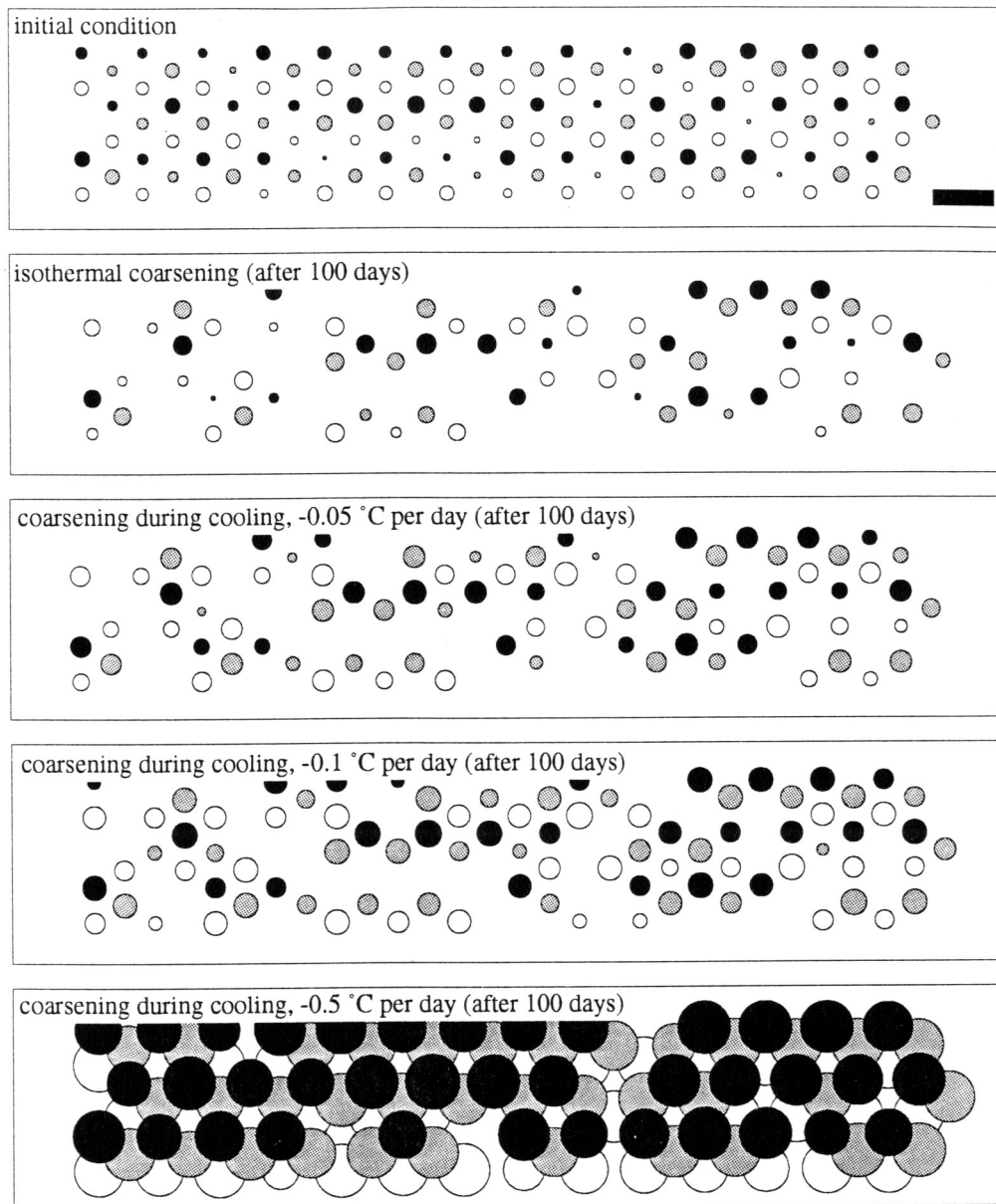
Figure 7.14 Partial output of the simulation results for various cooling rates (simulation conditions summarized in Figure 7.13 and Table 7.2).
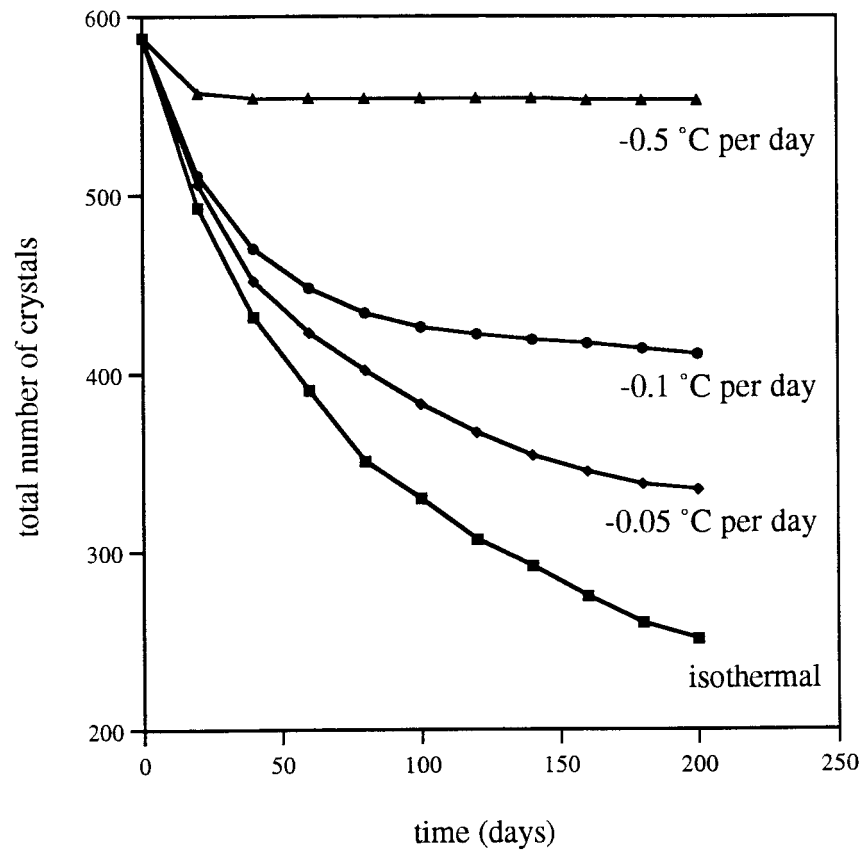
Figure 7.15 Plot of time vs. total number of crystals from simulation (simulation conditions summarized in Figure 7.13 and Table 7.2).
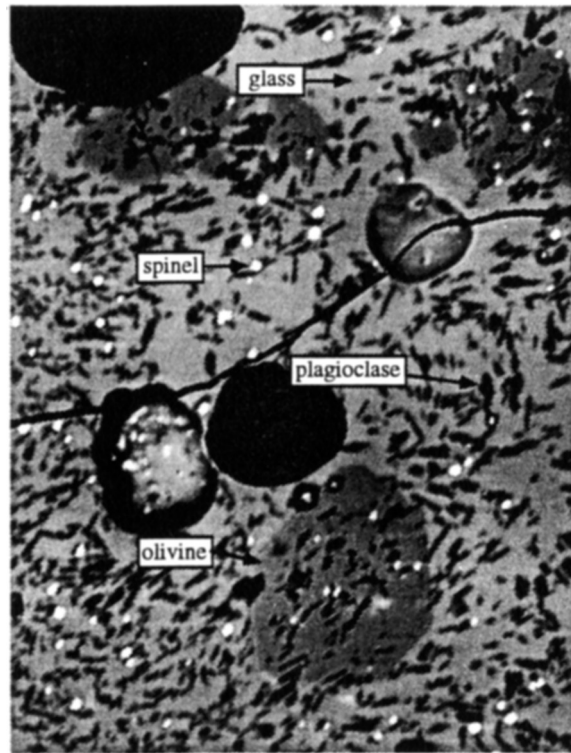
Figure 7.16 Backscattered electron image of the isothermally coarsened F2-2 bulk composition sample (Allen *et al*, 1989). Phenocryst phase (olivine) is coarser than the matrix phases (spinel and plagioclase) due to difference in coarsening rate. Experiment performed by Ben Hanson. Field width: 200 μm.
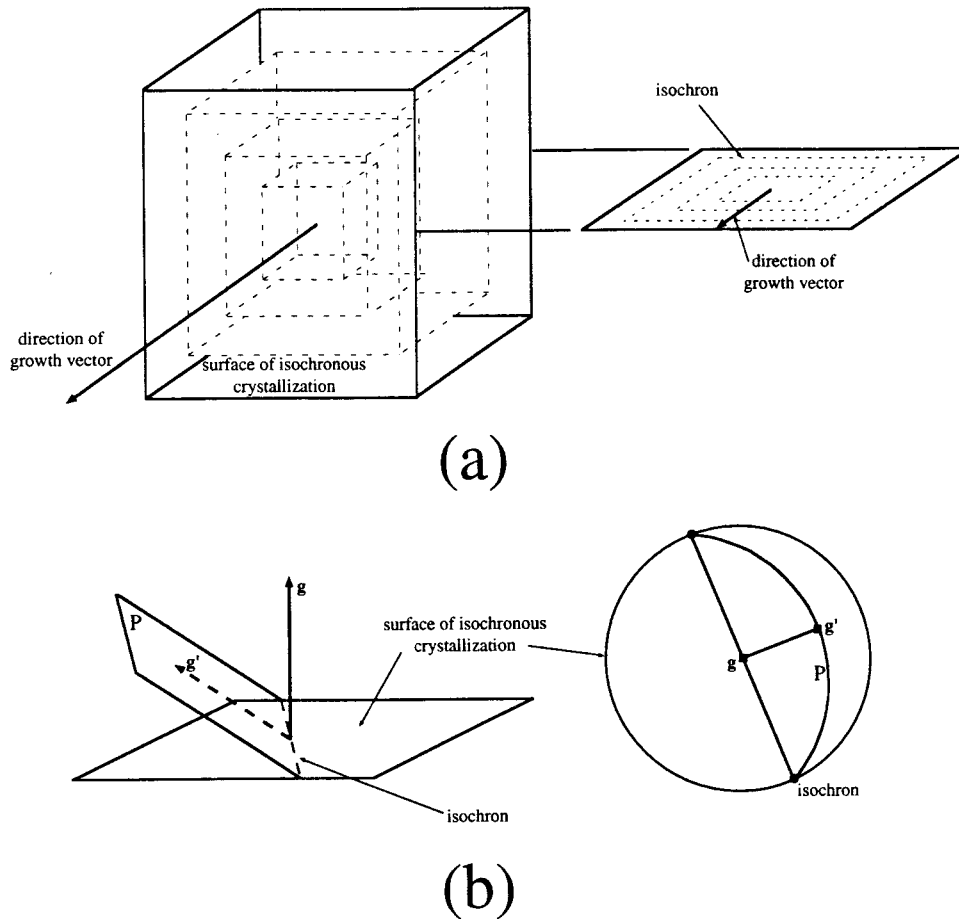
Figure 8.1  Isochron and growth vector.  (a) Surface of isochronous crystallization (surfaces of rectangular boxes) and direction of growth vector which is normal to the surface of isochronous crystallization.  The magnitude of growth vector is the growth amount per unit time.  (b) Relationship between an isochron (trace of isochronous crystallization surface) and a projected growth vector on a two dimensional cutting plane.  The projected growth vector is always normal to isochron (g: growth vector, g': orthogonally projected growth vector, P: arbitrary plane).

Figure 8.2   Genetically classified crystal boundaries.   (a) Growth impingement boundary.  When a growth impingement boundary is formed by two growing crystals, material  ages (at o and x) across the boundary are the same.  Arrow along the boundary indicates the younging direction.  (b) Displacement impingement boundary formed by rotation and translation of crystals.  (c) Migrated grain boundaries (top) and phase boundaries (bottom).  Boundary migrates through material point (star symbol). (d) Dissolution boundary formed by dissolution of crystal(s) along the boundary. Notice the change of distance (from d1 to d2) of material points. Empty symbols represent the position of material points before dissolution and filled symbols represent the position after dissolution.  The diagram represents the special case when equal amounts of material are removed from both crystals.
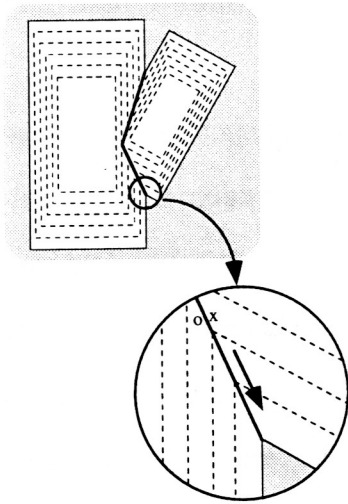
(a)
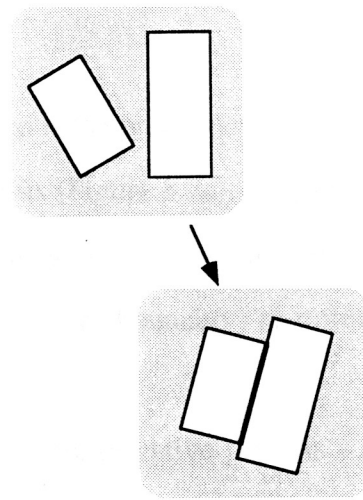
(b)
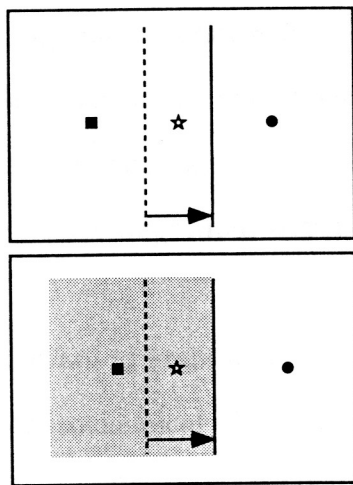
(c)
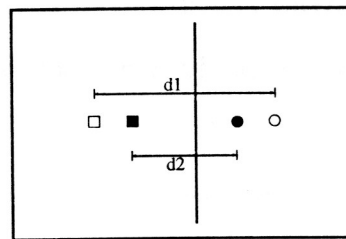
(d)

Figure 8.3   Geometric features of growth impingement boundaries.  (a) Construction of a new segment of a growth impingement boundary, using two growth vectors ($g_1$ & $g_2$).   I: intersection between two isochrons.   (b) Straight growth impingement boundaries formed when relative growth rate of two crystals is constant.  (c) Kinked or curved growth impingement boundaries formed when relative growth rate of two crystals is changing.  (d) Orientation limit of a growth impingement boundary when the growth impingement boundary is formed by *growing* crystals.  Rays of arrows represent the possible orientations.  (e) Example of geometrically impossible orientation of a growth impingement boundary (in the dark rectangular region).  (f) Kink in a growth impingement boundary formed by the change in the impinging crystal faces. The older segment of the boundary is formed by f1-f2 face. Sudden orientation change occurs when the boundary is formed by f1-f2' face.

(a)

(b)

(c)

(d)

(e)

(f)
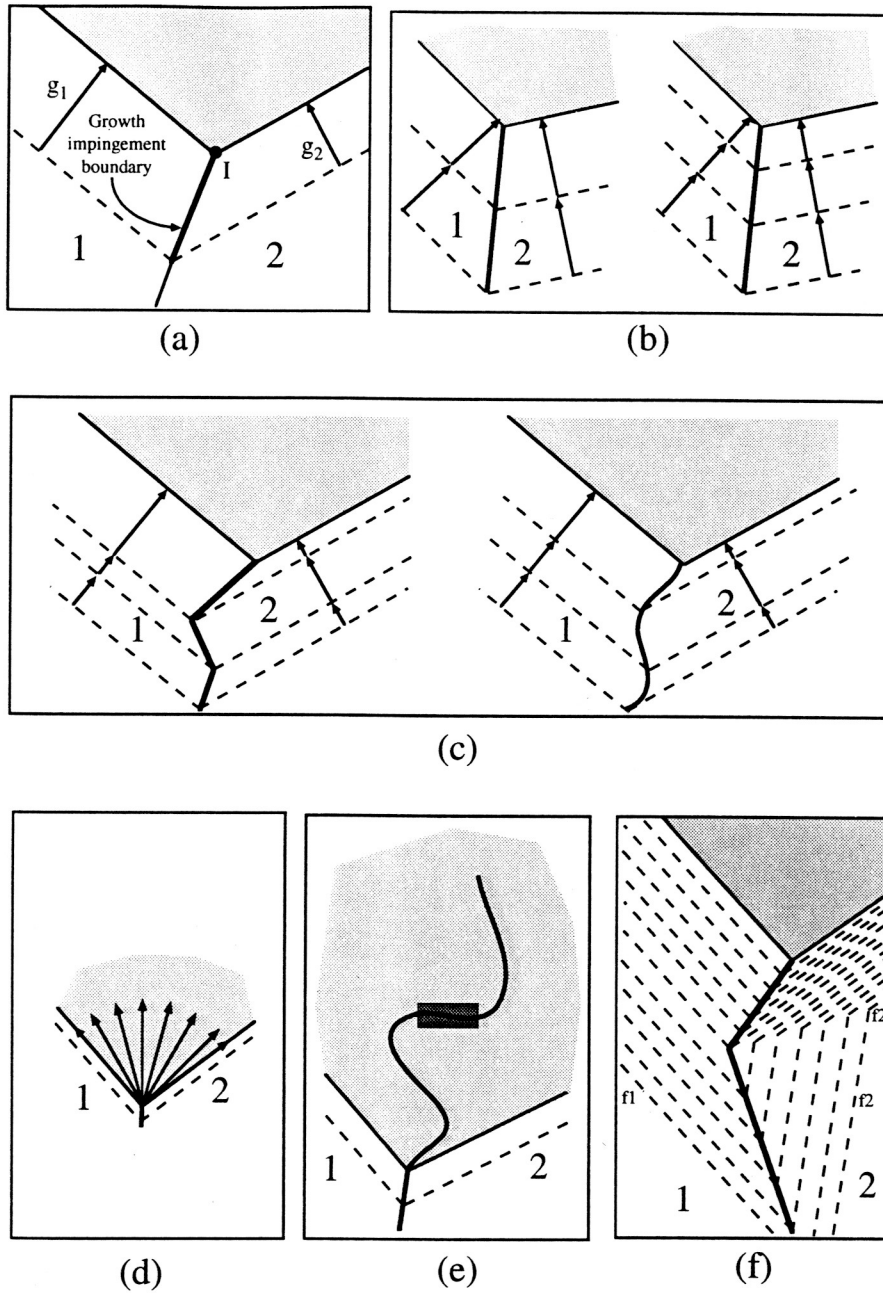
Figure 8.4   Geometric features of displacement impingement boundaries, migrated boundaries, and dissolution boundaries.   (a), a migrated boundary (b), and a dissolution boundary (c).   (a) A displacement impingement boundary is likely to be straight and rational relative to two crystals, and have isochrons parallel to the boundary.   When further crystal growth occurs after formation of the displacement impingement boundary, growth impingement boundaries (arrow) will form at the end of the displacement impingement boundary.   (b) Migration of an initial growth impingement boundary (left).   top: when resetting of chemical zoning does not occur, older chemical pattern of crystal 2 can be preserved in crystal 1.   bottom: when resetting occurs, chemical pattern in the migrated part of crystal 1 will not have any relation to the original chemical patterns in crystals 1 and 2.   (c) Dissolution at a displacement impingement boundary.   Isochrons truncated by the boundary are expected.   top: for a situation where only one crystal is dissolving.   bottom:   for a situation where both crystals are dissolving.

(a)

(b)

(c)

#: boundaries formed by the end member process - growth impingement
*: boundary formed by the end member process - displacement impingement
$_BV_A$: velocity of B with respect to A (both A & B are material points
            inside crystals)
$_bV_{xl}$: velocity of a crystal melt-interface with respect to a material point
            inside a crystal
O: conditions for the formation of crystal boundaries
x: conditions when crystal boundaries do not form

(a)



%: no modification
Δ: newly recognized classes
signs in the box represent the sign of $_BV_A$ (velocity of
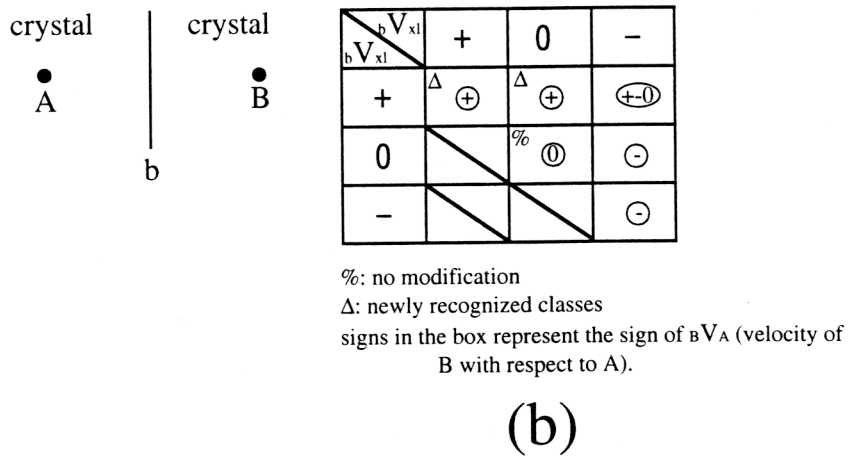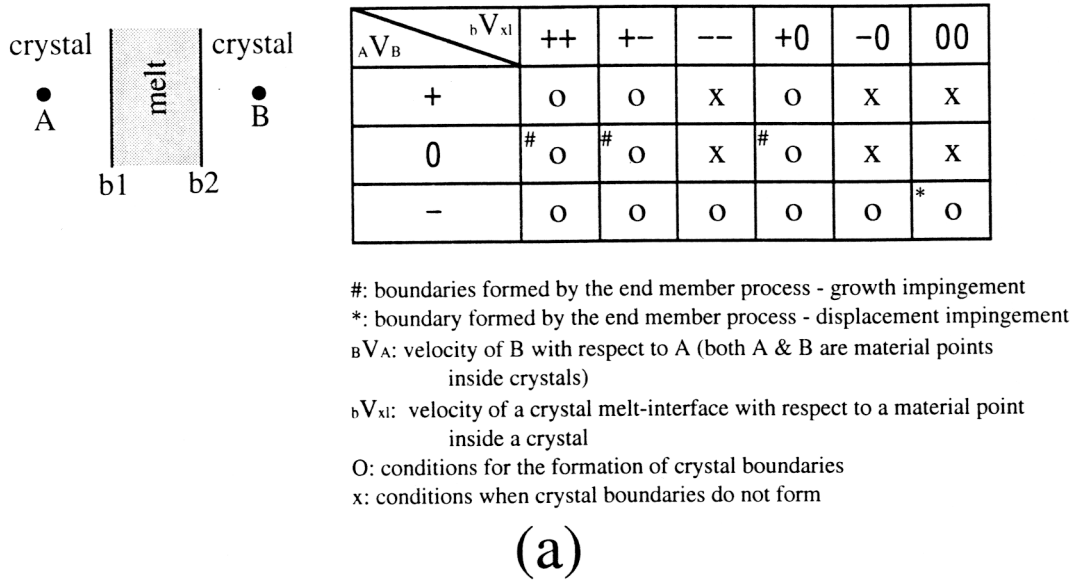            B with respect to A).

(b)

Figure 8.5    Classification of boundaries based on velocities of material points and boundaries. (a) for primary boundaries. (b) for secondary boundaries.

Figure 8.6   Effect of cutting on apparent orientation of the younging direction in a growth impingement boundary.   (a) Stereograph: lower hemisphere projection of isochronous crystallization surfaces (1 & 2) and cutting planes (x, y & z).   When a cutting plane (x) includes two growth vectors, the younging direction observed on the plane is the *true* younging direction.   *Apparent* younging direction appears when the cutting plane (y and z) is in a more general orientation with respect to the two growth vectors.   (b) Depending on the orientation of a cutting plane, younging directions can be hidden, and isochrons appear parallel to the boundary, resulting in similar patterns to a displacement impingement boundary.   (b1) cuts boundary parallel to the top of the block diagram.   (b2) cuts parallel to the right vertical face of block diagram.

● true younging direction

○ apparent younging directions

(a)

(b1)

(b2)
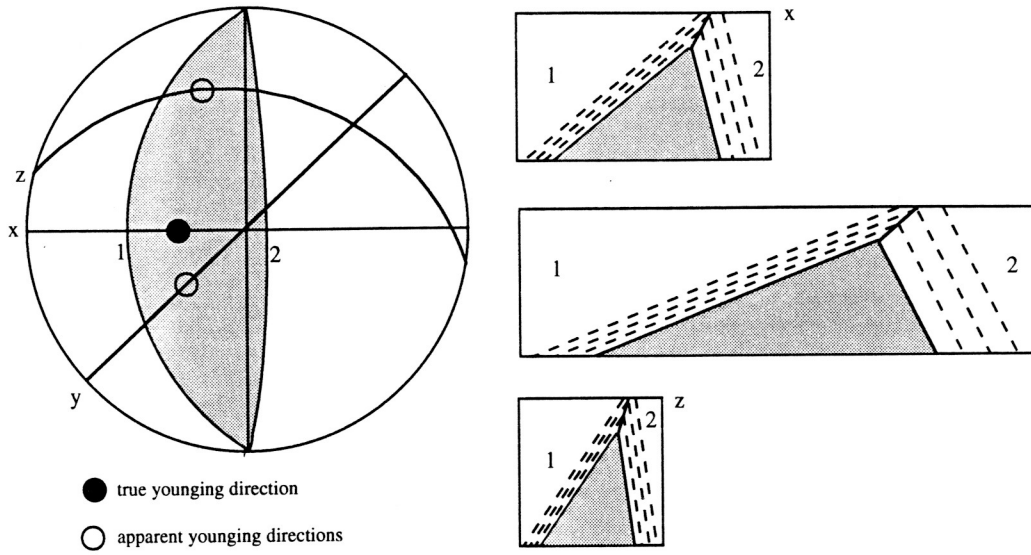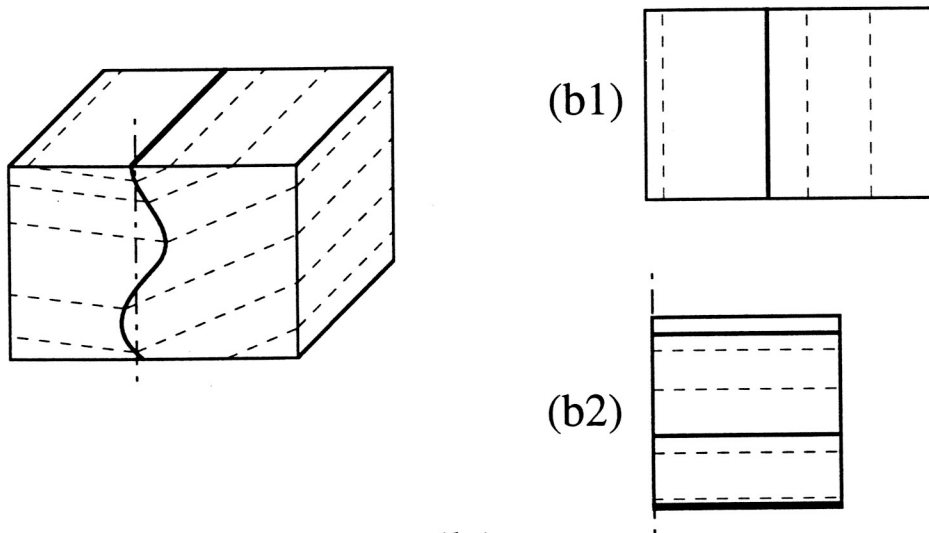
(b)

Figure 8.7   Patterns of younging directions at triple junctions of growth impingement boundaries.  (a) Schematic three dimensional illustration of grain boundaries, a grain edge and a triple junction point.  (b) & (c) Patterns of possible younging directions at a triple junction.  (b) Pattern with three converging younging directions; last melt consumption by crystallization occurs at the triple junction.  (c) Pattern with two converging younging directions and one diverging direction.  The diverging younging direction indicates the direction of local melt consumption by crystallization.

grain edge

grain boundary

trace of grain boundary
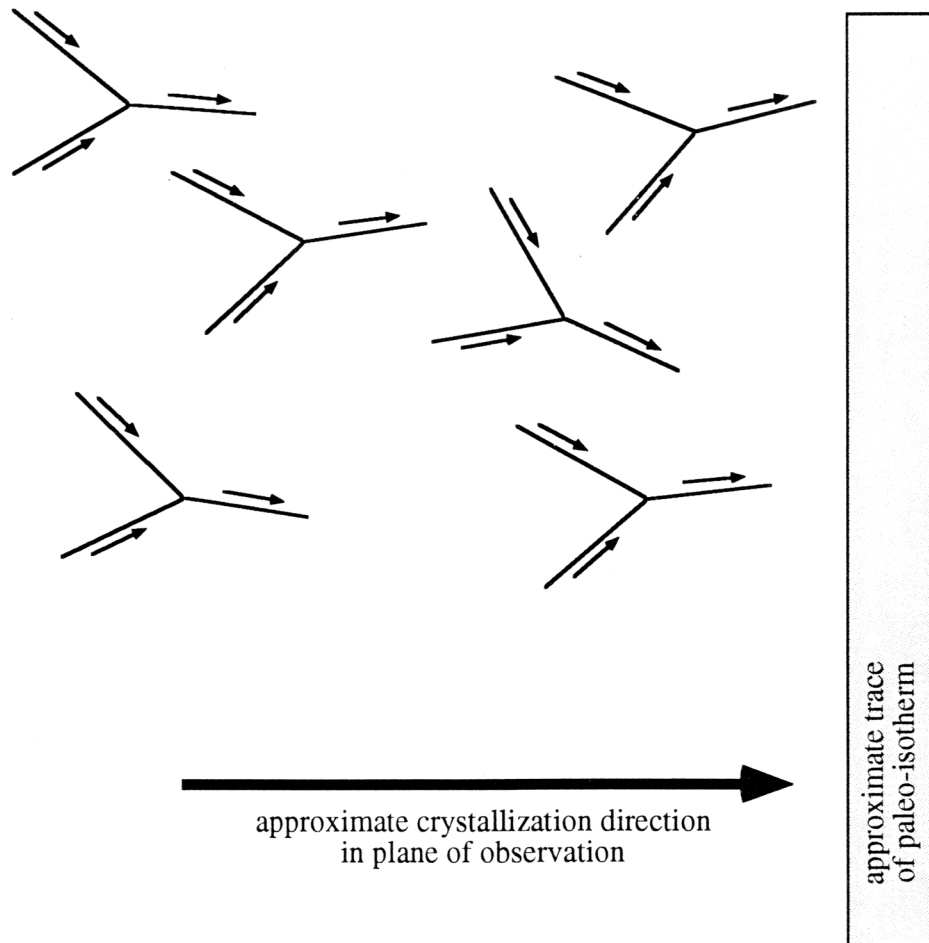
triple junction point

(a)

(b)

(c)
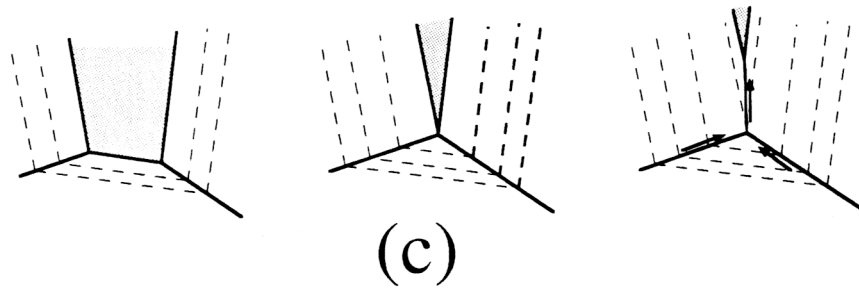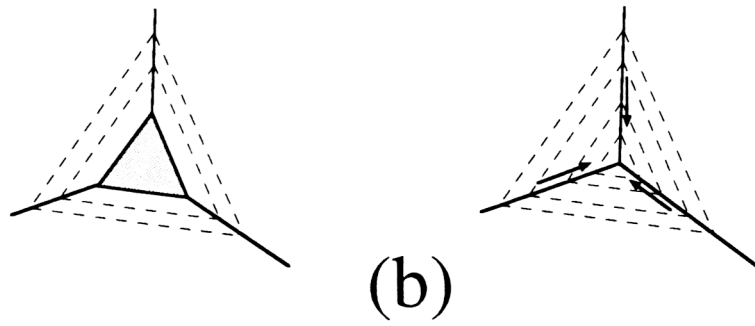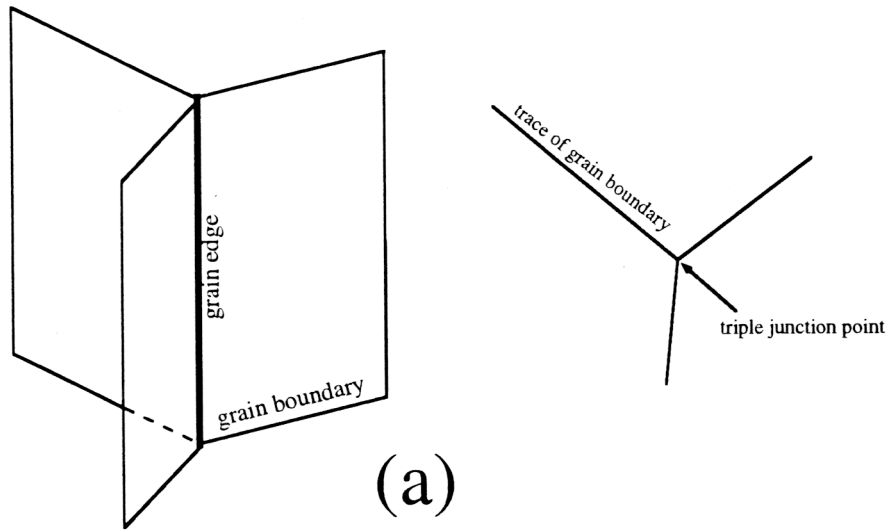
Figure 8.8   Hypothetical illustration of preferred orientation of local melt consumption directions which could be interpreted as approximate two-dimensional crystallization direction of magma.  Drawn perpendicular to the crystallization direction is the trace of paleo-isotherm.